ISSN 1028-8546

Volume XXIV, Number 1
Section: En
March, 2018

# Azerbaijan Journal of Physics

# Fizika

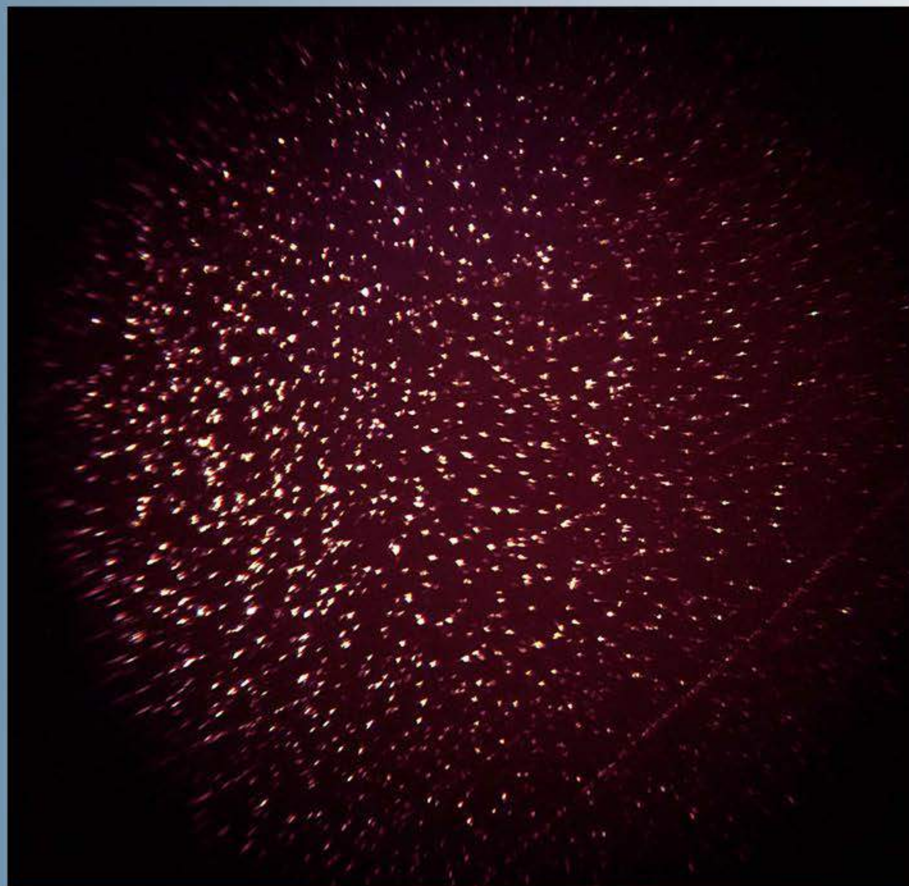

www.physics.gov.az

G.M. Abdullayev Institute of Physics
Azerbaijan National Academy of Sciences
Department of Physical, Mathematical and Technical Sciences

Published from 1995
Ministry of Press and Information
of Azerbaijan Republic,
Registration number 402, 16.04.1997

**ISSN 1028-8546**
vol. XXIV, Number 01, 2018
Series: En

# *Azerbaijan Journal of Physics*

# *FIZIKA*

*G.M.Abdullayev Institute of Physics*
*Azerbaijan National Academy of Sciences*
*Department of Physical, Mathematical and Technical Sciences*

**HONORARY EDITORS**

Arif PASHAYEV

**EDITORS-IN-CHIEF**

Nazim MAMEDOV Chingiz QAJAR

**SENIOR EDITOR**

Talat MEHDIYEV

**INTERNATIONAL REVIEW BOARD**

Ivan Scherbakov, Russia
Kerim Allahverdiyev, Azerbaijan
Mehmet Öndr Yetiş, Turkey
Gennadii Jablonskii, Buelorussia
Rafael Imamov, Russia
Vladimir Man'ko, Russia
Eldar Salayev, Azerbaijan
Dieter Hochheimer, USA
Victor L'vov, Israel
Vyacheslav Tuzlukov, South Korea
Majid Ebrahim-Zadeh, Spain
Firudin Hashimzadeh, Azerbaijan
Anatoly Boreysho, Russia
Mikhail Khalin, Russia
Hasan Bidadi, Tebriz, Iran
Natiq Atakishiyev, Mexico
Tayar Djafarov, Azerbaijan
Arif Hashimov, Azerbaijan
Javad Abdinov, Azerbaijan
Bagadur Tagiyev, Azerbaijan
Talat Mehdiyev, Azerbaijan
Vali Huseynov, Azerbaijan
Ayaz Baramov, Azerbaijan
Tofiq Mammadov, Azerbaijan
Salima Mehdiyeva, Azerbaijan
Shakir Nagiyev, Azerbaijan
Rauf Guseynov, Azerbaijan
Almuk Abbasov, Azerbaijan
Yusif Asadov, Azerbaijan

**TECHNICAL EDITORIAL BOARD**

Senior secretary Elmira Akhundova, Nazli Guseynova, Sakina Aliyeva,
Nigar Akhundova, Elshana Aleskerova, Rena Nayimbayeva

**PUBLISHING OFFICE**

131 H.Javid ave, AZ-1143, Baku
ANAS, G.M.Abdullayev Institute of Physics

Tel.: (99412) 539-51-63, 539-32-23
Fax: (99412) 537-22-92
E-mail: jophphysics@gmail.com
Internet: www.physics.gov.az

It is authorized for printing:

Published at "ŞƏRQ-QƏRB"
17 Ashug Alessger str., Baku
Typographer : Aziz Gulaliyev

Sent for printing on: __.__. 201_
Printing approved on: __.__. 201_
Physical binding:_________
Number of copies:______200
Order:_________

# PHOTOLUMINESCENCE OF $(Ga_2S_3)_{0.94}$:$(Eu_2O_3)_{0,05}(Tb_2O_3)_{0,01}$ CRYSTAL

**O.B. TAGIYEV, Kh.B. GANBAROVA, F.A. KAZIMOVA, T.Sh. IBRAGIMOVA, K.O. TAGIYEV, S.O. GUSEYNOVA**

*G.M.Abdullayev Institute of Physics Azerbaijan National Academy of Sciences, Baku, AZ1143, H. Javid ave., 131, Azerbaijan*

*E-mail:oktay58@mail.ru*

The investigations of luminescence spectra, dependence of luminescence intensity on excitation source power and also $(Ga_2S_3)_{0.94}$:$(Eu_2O_3)_{0,05}(Tb_2O_3)_{0,01}$ crystal luminescence kinetics in temperature interval 10 – 300K are given in the work. Stokes shifting (ΔS=0,6 eV), Huan - Rice factor (S=12±2), energy of optical phonons and lifetime of $Eu^{2+}$ ions decreasing from 400nsec up to 200nsec with temperature increase are defined.

**Keywords :** photoluminescence, excitation, intracenter transition, luminescence kinetics, lifetime.
**PACS:** 50.5230

## INTRODUCTION

Nowadays the study of inorganic materials is the modern scientific-technical direction connecting the series of tasks of quantum electronics, spectroscopy, crystallography and chemical technology in one complex problem. The activated crystals with impurity of rare-earth ions (REI) are the main objects of its study. The production of high-performance devices for visualization and lighting which are able to compete with traditional systems requires the obtaining of luminophors with specifical propeties. This necessity causes the development of new material obtaining or optimization of already existing luminophors.

Introduction of rare-earth element impurities (REE) is necessary for obtaining of radiation big quantum output at optical and electrical pumping of $Ga_2S_3$ crystals, moreover the effective energy transfer of excited carriers to 4f-electrons takes place. REE excitations are possible through wide matrix absorption band that decreases the excitation threshold increasing the luminescence efficiency.

The diversity of radiated transitions of REE allows us to realize the both any required lightening color and laser generation [1]. The essential peculiarity of the given materials is in the absence of concentration damping (up to 7mol% of impurity) for series of levels taking place in generation [2,3].

There are several compounds $Ga_2S$, GaS, $Ga_4S_5$, $Ga_2S_3$ in Ga-S system [4]. The distinctive feature of these compounds is the difference in their stability in air and corrosive medium (in mineral acids HCI, $HNO_3$, $H_2SO_4$). $Ga_2S_3$ is the more stable from the given compounds. It crystallizes in structures of sphalerite or wurtzite and is related to crystal-chemical group of diamond like substances.

The structure of this compound is the defect one in relation to normal structure of sphalerite or wurtzite types because of absence of gallium atoms, 1/3 part of places of which is vacant one in lattice. The impurities in compound of $Ga_2S_3$ type are electrically inactive ones. This peculiarity of $Ga_2S_3$ compound makes it closer with glassy and amorphous semiconductors. Rare-earth elements (REE) create the effective radiation centers in $Ga_2S_3$ and these compounds reveal the intensive luminescence at the influence of external factors (electric field, ultraviolet and roentgen radiations, electron beams and etc) [5,6].

The solid solutions of $(Ga_2S_3)_{1-x}(M_2O_3)_x$ (M-Eu, Sm, Tb) system are firstly synthesized by authors [7,8]. These crystals crystallize in monoclinic syngony.

The results of investigations of $Sm^{2+}$ ion luminescence in $Ga_2S_3$ crystals at78-450K are given in [9]. The narrow bands with maxima at 610, 657, 829nm, which aren't connected by transmitted transitions $^5D_1 \rightarrow ^7F_0$, $^5D_1 \rightarrow ^7F_2$, $^5D_0 \rightarrow ^7F_4$ correspondingly, are observed in $Ga_2S_3$: $Sm^{2+}$ crystal radiation spectrum. The luminescent properties of europium bivalent ions in $Ga_2S_3$ are considered in [10] at temperatures 77÷300K. There are bands with maximum at 545nm (band half-width 0.13eV) caused by $4f^65d \rightarrow ^8S_7(4f^7)$ transition are observed in spectrum. The work [11] is dedicated to the investigation of luminescence spectra $Ga_2S_3$:$Tb_2O_3$ in temperature interval 77÷300 K, it is shown that the observable narrow-band radiation in wave length region 400÷750 nm is connected with intracenter transitions $^5D_4 \rightarrow ^7F_6$ (492 nm), $^5D_4 \rightarrow ^7F_5$ (544 nm), $^5D_4 \rightarrow ^7F_4$ (584 nm), $^5D_4 \rightarrow ^7F_3$ (625 nm), $^5D_4 \rightarrow ^7F_2$ (680 nm) of $Tb^{3+}$ ion.

In case if there is more than one REE in the system then the nonadditive effects being the result of their interaction. The interaction can reveal in change of absorption and radiation spectra, duration of excitation state, probability of energy transitions and series of other properties because of reconstruction of energy level system. At big concentrations or in cases of inclination from statistical distribution of REE ions there are other features of interaction in crystal lattices such as line shifting and energy redistribution in them, formation of new lines and disappearance old ones. The problem of sensitized luminescence at which the energy transfer from sensitizer resolved level to activator forbidden band plays the main role in one from developing theories in the given direction [12-15]. The strong overlapping of $Eu^{2+}$ excitation spectrum and $Tb^{3+}$ radiation spectrum can serve the reason of energy transfer from $Tb^{3+}$ to $Eu^{2+}$ [16].

The investigation of luminescence properties of $Ga_2S_3$ solid solutions activated by rare-earth element ions is of interest from both points of view the (PhL) photoluminescence mechanism revealing and their practical application. The given work is dedicated to

131 H.Javid ave, AZ-1143, Baku
ANAS, G.M.Abdullayev Institute of Physics
E-mail: jophphysics@gmail.com

investigation of luminescence spectra in temperature interval 10 – 300K, dependence of luminescence intensity on excitation source power and also crystal luminescence kinetics $(Ga_2S_3)_{0.94}$:$(Eu_2O_3)_{0,05}(Tb_2O_3)_{0,01}$.

## EXPERIMENT

For formation of effective luminescence spectra in $(Ga_2S_3)_{0.95}$:$(Eu_2O_3)_{0.05}$ the impurity Tb in $Tb_2O_3$ form is introduced in synthesis process. The terbium oxide content changes from 0,1 up to 7at%. The melts are synthesized in evacuated ampoules up to $10^{-4}$ Pa at 1400K with periodic mixing. The samples are excited by radiation of impulse nitrogen laser (Laser LN 1000 with energy 1,4J by impulse 0,5 nsec, wavelength 337,1 nm). The luminescence spectrum is registered on spectrometer HR 460, radiation detector is CCD detector.

## RESULTS AND THEIR DISCUSSION

PhL spectra at different temperatures are presented in fig.1.

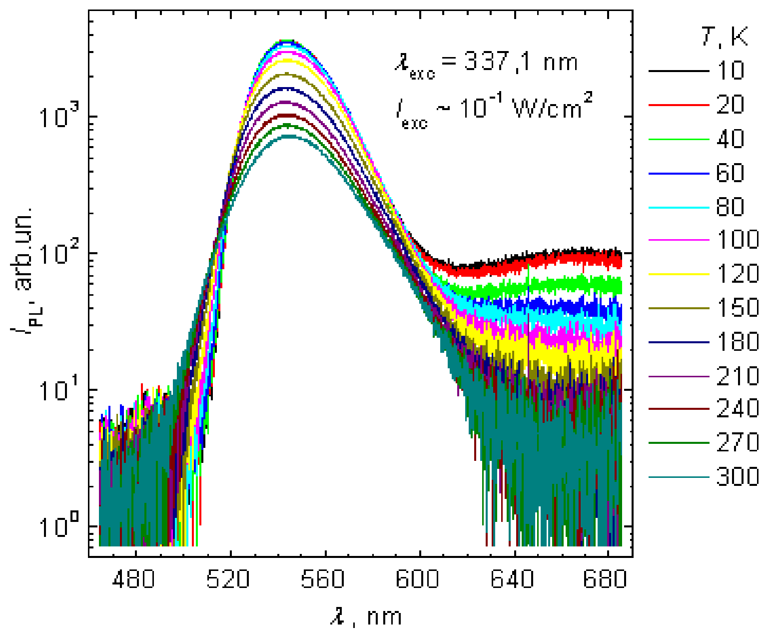


*Fig.1.* PhL spectrum of $(Ga_2S_3)_{0.94}$:$(Eu_2O_3)_{0,05}(Tb_2O_3)_{0,01}$ at temperatures: 1-10,2-20, 3-40,4-60,5-80,6-100,7-120,8-150,9-180, 10-210,11-240,12-270,13-300K, $\lambda_{exc.}$=337.1nm, $I_{exc.}=10^{-1}$Vt/cm$^2$.

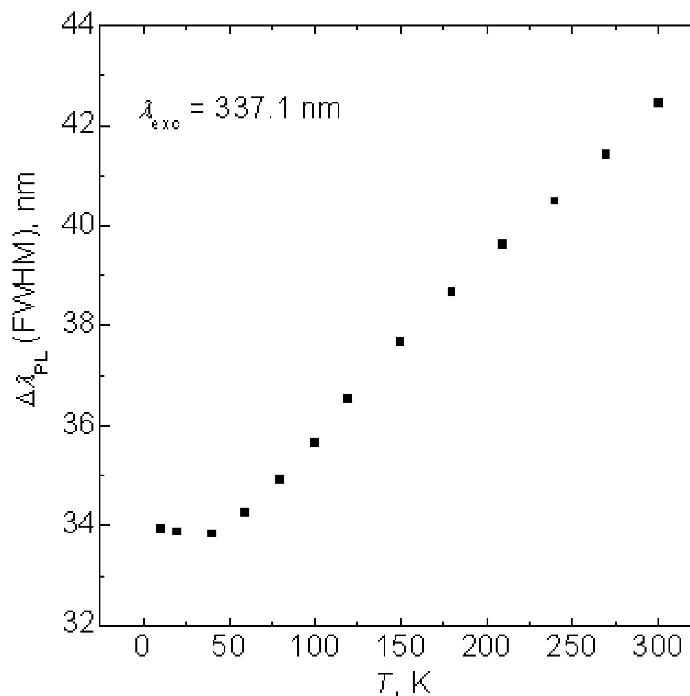


*Fig.2.* The dependence of photoluminescence bandwidth with maximum at 548nm on temperature.

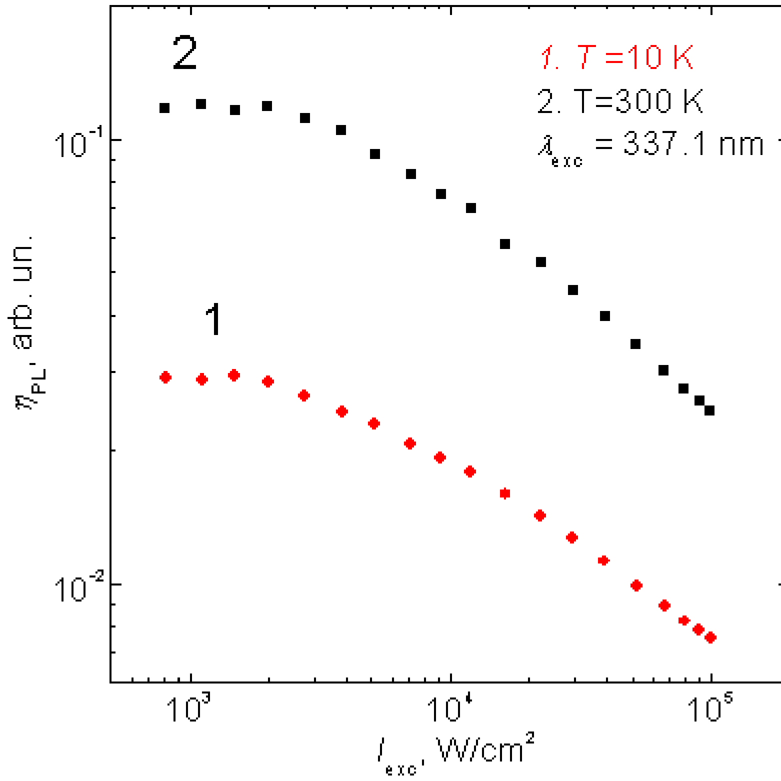


*Fig.3.* The dependence of PhL efficiency on excitation level in $(Ga_2S_3)_{0.94}$:$(Eu_2O_3)_{0,05}(Tb_2O_3)_{0,01}$ crystal at $\lambda_{exc.}$=337.1nm, 1-10, 2-300K.

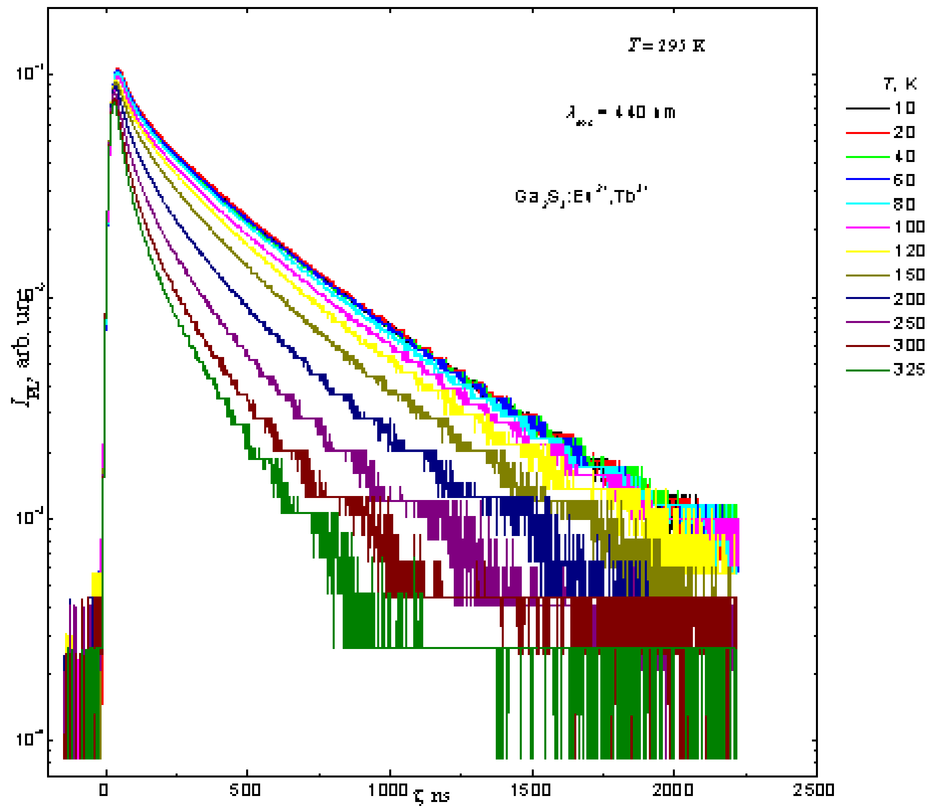


*Fig.4.* The kinetics of luminescence damping of $(Ga_2S_3)_{0.94}$:$(Eu_2O_3)_{0,05}(Tb_2O_3)_{0,01}$ crystal at temperatures: 1-10, 2-20, 3-40, 4-60, 5-80, 6-100,7-120, 8-150, 9-200, 10-250,11-300, 12-325K.

It is seen that they are broadband ones and have spectral region 480-650nm. The band intensity significantly decrease, band half-width increases (fig.2) and their maximum energy position (548nm) doesn't change with temperature increasing. On this spectrum $Ga_2S_3:Tb^{3+}$ the maximums character for spectrum aren't observed and band intensity with maximum 548nm observed in PhL spectrum $Ga_2S_3:Eu^{2+}$ which caused by intracenter transitions $4f^65d \rightarrow 4f^7$ ($^8S_{7/2}$) of $Eu^{2+}$ ions, increases [10]. The absence of radiation bands corresponding to above mentioned transitions $5d \rightarrow {}^7F_6$ and $5d \rightarrow {}^7F_5$ of $Tb^{3+}$ ion in PhL spectrum of crystals $(Ga_2S_3)_{0.94}:(Eu_2O_3)_{0,05}(Tb_2O_3)_{0,01,}$ activated by two REE, probably is connected with energy transfer from $Tb^{3+}$ ion to $Eu^{2+}$ ion. Such energy transfer between these ions is shown in [17,18]. It takes place because in these crystals the lowest excited level 5d of $Tb^{3+}$ ion is higher than lowest excited level $4f^65d$ of $Eu^{2+}$ ion [16]. The temperature dependence of PhL band half-width with maximum at 548nm in *Г(T)* and $T^{1/2}$ coordinates is presented in fig.2. It is seen that this dependence in temperature interval 77 – 300K is linear one and can be described by the model of configuration coordinates and Boltzmann distribution. The expressions connecting Stokes shift *ΔS*, Huan-Rice factor *S* and phonon energy $\hbar\omega$ with temperature dependence of band half-width *Г (T)* are obtained on the base of theoretical analysis of absorption and radiation spectra in [17,18]:

$$\Delta S = (2S - 1) \quad \hbar\omega \qquad (1)$$

$$\Gamma(T) = 2{,}36 \ \hbar\omega\sqrt{S}\sqrt{\coth\frac{\hbar\omega}{2kT}} \qquad (2)$$

If $\hbar\omega < kT$ then the expression under square root (2) we can expand in series and limit ourselves by the first term:

$$\coth x = \frac{1}{x}, \qquad \text{where } x = \frac{\hbar\omega}{kT} \qquad (3)$$

Then expression (2) we can rewrite in the following form:

$$\Gamma(T) = 2.36\hbar\omega\sqrt{S}\sqrt{\frac{2kT}{\hbar\omega}} \qquad (4)$$

or

$$\Gamma(T) = 2.36\sqrt{S}\sqrt{2kT \cdot \hbar\varpi} \qquad (5)$$

Equation (5) shows that band half-width *Г(T)* linearly depends on $\sqrt{T}$ . The band half-width increases with temperature increase from 34 up to 43nm. Stokes shift (ΔS=0,6 eV), Huan-Rice factor (S=12±2) and energy of optical phonons ($\hbar\omega = 23$ MeV) are defined by experimental results. The constancy of energy position of broadband radiation maximum at 548nm with temperature change and band temperature dependence prove the belonging of this radiation band to $Eu^{2+}$ ions, i.e. to intracenter transitions $4f^65d - 4f^7(^8S_{7/2})$ of $Eu^{2+}$ ions (fig.1). PhL efficiency ($\eta_{PhL}$) saves its constant value at impulse excitation at wavelength 337nm in excitation level interval from$10^2$ Vt/cm$^2$ (fig.3). The insignificant decrease of PhL intensity and practically constant PhL efficiency significantly decreases at excitation levels higher $10^2$ Vt/cm$^2$. The further decrease of excitation level from$10^5$ Vt/cm$^2$ up to$10^2$ Vt/cm$^2$ leads to intensity reconstruction in previous level that evidences on absence of material degradation.

The kinetics of radiation damping for maximum 548nm at temperature interval10±335 K at excitation 440nm is shown in fig.4. As it is seen the luminescence damping in the given coordinates has the linear character, i.e. luminescence damping obeys to exponential law $I=I_0.e^{t/\tau}$. $Eu^{2+}$ ion lifetime decreases from 400 nsec up to 200nsec in solid solutions $(Ga_2S_3)_{0.94}:(Eu_2O_3)_{0,05}(Tb_2O_3)_{0,01}$ with temperature increase from 10K up to 325K that can be connected with thermal activation of radiationless recombination channel.

## CONCLUSION

Thus, it is shown that constancy of energy position of broadband radiation maximum at 548nm with temperature change and temperature dependence of band half-width evidences on belonging of this radiation band to $Eu^{2+}$ ions i.e., to intracenter transitions$4f^65d - 4f^7(^8S_{7/2})$ of $Eu^{2+}$ ions and also on the absence of material degradation in excitation level interval from $10^2$ - $10^5$ Vt/cm$^2$ and stability of position and form of PhL spectra.


[1] *S. Iida, T. Matsumoto, N.T. Mamedov, G.A.Y. Maruyana, A.I. Bairamov, B.G. Tagiev, O.B. Tagiev, R.B. Dzhabbarov*. Japon J. Appl. Phys., 1997. V.36, pt 2, (7A), L857.

[2] *B.G. Tagiev, V.A. Djalilov, T.A. Gyulmaliev, G.M. Niftiev, O.B. Tagiev, F.B. Askerov, B.M. Izzatov, Ya.G. Talibov*. Неорг. Mater. 1992. T. *B.G. Tagiev, Tagiev* 28 (12), s.2269 . (in Russian).

[3] *B.G. Tagiev, M.G. Shaxtaxtinskiy, V.A. Djalilov, T.A. Gyulmaliev, B.M. Izzatov, G.K. Aslanov, O.B. Tagiev, Ya.G. Talibov*. Neorq. Mater. 1993. t. 29 (10), s.1. (in Russian).

[4] *Z.S. Medvedeva*. Xalkoqenidi elementov III B podqruppi periodicheskiy sistem. Moskva, «Nauka», 1968, 216 s. (in Russian).

[5] *O.B. Tagiev, T.G. Mishina, S.A. Abushov*. Pisma v JTF, 2007, t. 33, s. 255-257. (in Russian).

[6] *C. Barthon, P. Benalloul, B.G. Tagiyev* et al. Energu Transfer between $Eu^{2+}$ and $Er^{3+}$ Eu, $EuGa_2S_4$:Er, Z.Chys: Condens Matter, 2004, v.16, p.8075-8084.

[7] *P.G. Rustamov, I.B. Baxtiyarov*. J. Neorq. Ximii. 1978. 22 (6), s.1703. (in Russian).

[8] *I.B. Baxtiyarov, P.G. Rustamov, A.N. Mamedov. J. Neorq. Mat. J. Neorq.*, 1980. 16 (4), s.2053. (in Russian).
[9] *A.N. Georgobiani, B.G. Tagiev, O.B. Tagiev, X.B. Ganbarova. Neorq. Mater*. 2008. 44 (6), 1. (in Russian).
[10] *A.M. Pashaev, B.G. Tagiev, O.B. Tagiev, X.B. Ganbarova.* JPS , 2001. 78(2), s.289. (in Russian).
[11] *B.G. Tagiev, O.B. Tagiev, X.B. Ganbarova.* Azerbaijan J. of Phys. 2013. V.XIX, N 2, c.92.
[12] *Y. Tan, C. Shi.* J. Phys. Chem. 1999. Sol., 60, p.1805.
[13] *M.D. Shinn, W.A. Sibley*. Phys. Rev. 1984.B, 29 (7), p.3834.
[14] *Rubio J.O., Minoz A.F., Zaldo C., Murrieta H.S.* Sol. St. Commun., 1988. 65(4), p.251.
[15] *B.M. Agranovich, M.M. Galanik.* Perenos enerqii elektronnoqo vozbujdeniya v kondensirovannix sredax M., 1978. (in Russian).
[16] *O.B. Tagiev, X.B. Ganbarova.* FTP. 2015. t.49, №4, s. 459-462. (in Russian).
[17] *P. Dorenbos*. J.Phys.: Condens. Mtter, 2003. p.575-594.
[18] *P. Dorenbos* J.Luminescence, 2003. 104, 239 – 260. P.392.

*Received: 05.02.2018*

# THE PRODUCTION OF THE HIGGS BOSON ON ELECTRON-POSITRON LINEAR COLLIDERS

**F.T. KHALIL-ZADE**
*G.M.Abdullayev Institute of Physics Azerbaijan National Academy of Sciences,*
*Baku, AZ1143, H. Javid ave., 131, Azerbaijan*

Taking into account the polarizations of the linear colliding electron-positron beams, differential, total cross-section as well as the energy-angular distribution of the fermions in the process $e^+e^- \to Hf\bar{f}$ are calculated. The characteristic features of the cross-sections and the polarization effects of the process on the linear accelerator ILC (International Linear Collider) are investigated.

**Keywords:** Standard Model, ILC, Higgs boson, Lepton production, $e^-e^+$ interactions.
**PACS:** 12.15-y, 13.66.Fg, 14.80-j, 14.70 Hp

## INTRODUCTION

The study of different properties of Higgs boson is the one of the most actual tasks of modern high-energy physics. The modern high-energy research at the Large Hadron Collider (LHC) at CERN, in such projects as ATLAS and CMS ones will be added by investigations on electron-positron colliders, in particular, on ILC (International Linear Collider) [1]. The pure signals and precise measurements which can be obtained with the help of linear collider of high luminosity give us the possibility for new ideas in our understanding of fundamental interactions of nature and structure of the matter, space and time. The high-energy physics on linear collider will have the new possibilities for investigations, for example, the possibility of polarized beams formation. As is known, a high degree of polarization can be realized without significant losses in luminosity. The polarized electron beam already will serve as the valuable tool for checking of Standard Model and for diagnostics of new physics. The most investigations will be carried out at energies $200 \quad GeV < \sqrt{s} < 500 \quad GeV$ and the integrated luminosity will reach the value $L_{int} = 500\, fb^{-1}$.

The polarization high degree is provided in ILC plans, for electron is on 80% and for positron on 50%. Though the beam polarization plays not the main role in definition of Higgs boson properties however this is very useful for process dividing, suppression of background processes and accuracy increase. The use of polarized beams in this context has mainly the statistic meaning. The annihilation processes are the dominating ones in $e^+e^-$ experiments. In annihilation processes the helicities of electron and positron are correlated with virtual particle spin in direct channel. That's why the corresponding combinations of polarizations of electron and positron beams can be used for significant increase of the velocity of signal and also for effective suppression of undesirable background processes. The increase of signal/background relation in combination with high luminosity gives the additional possibilities for investigations.

## 1. PROCESS $e^+e^- \to Hf\bar{f}$ ON POLARIZED COLLIDING ELECTRON-POSITRON LINEAR COLLIDERS

The detail analysis of all properties of Higgs boson is the central part of ILC physics program. The two main processes $e^+e^- \to HZ$ with following decay

$$Z \to > l^+ + l^- \tag{1}$$

$$e^+e^- \to H\nu\bar{\nu} \tag{2}$$

will be considered at $\sqrt{s} = 500 \;\; GeV$.

In the framework of the Standard Model, due to the rather strong coupling of the H- boson with W- and Z - bosons, the main sources of H- bosons will be the processes of their emission by W- and Z- bosons produced in various experiments. The particularly intense and favorable source of H- bosons could be the process $e^+e^- \to Hf\bar{f}$ occurring on linear electron-positron beams.

Note that production process of Higgs boson on polarized colliding beams $e^+e^- \to Hf\bar{f}$ had been investigated in detail earlier in [2-8]. In these works the dependences of differential cross-section distribution by invariant mass of muon pair, dependences of differential cross-section of the proses (3) on $x$ at different energies of initial beam for the small mass of Higgs boson and as well as the dependence of total cross-section of the process (3) on energy of initial colliding beams $\sqrt{s}$ are investigated. In addition, the effects associated with polarization (both longitudinal and transverse) of colliding beams were investigated in detail in [2-8].

Due to the research of various properties of the Higgs boson planned in ILC in the near future, it becomes necessary to recalculate various characteristics of the $e^+e^- \to Hf\bar{f}$ process.

The process $e^+e^- \to Hf\bar{f}$ taking place by the one of the following scheme:

$$e^+e^- \to Z^* \to HZ^* \to Hf\bar{f}, \tag{3a}$$

$$e^+e^- \to Z \to HZ^* \to Hf\bar{f}, \tag{3b}$$

$$e^+e^- \to Z^* \to HZ \to Hf\bar{f}, \tag{3c}$$

131 H.Javid ave, AZ-1143, Baku
ANAS, G.M.Abdullayev Institute of Physics
E-mail: jophphysics@gmail.com

is investigated in detail in present work, where Z is real, $Z^*$ is virtual neutral vector boson, $f$ is fundamental fermion (lepton or quark). Taking into account the polarizations of the electron-positron beams, a dependence of differential cross-section on invariant mass and total cross-section of the processes (3) are calculated. The dependences of the obtained expressions on the initial energy are investigated and the characteristic features in the behavior of the cross-sections are revealed.

Within the framework of Standard Model the amplitude of the process (3) has the following form:

$$M_{fi} = 2^{3/4} G^{3/2} D_Z(q_1) D_Z(q_2) \bar{u}(-p_2)\gamma_\mu(g_V + \\ + g_A\gamma_5)u(p_1)\bar{u}(k_1)\gamma_\mu(G_V + G_A\gamma_5)u(-k_2)H(\chi), \tag{4}$$

where $\Gamma_Z$ is Z-boson width, $q_1 = p_1 + p_2 = k_1 + k_2 + \chi$, $q_2 = p_1 + p_2 - \chi = k_1 + k_2$; $p_1, p_2, k_1, k_2$ and $\chi$ are the 4-impulses of electron, positron, fermion, antifermion and $H$-boson correspondingly. In (4) we neglect the terms proportional to $m_e/m_Z$ and $m_f/m_Z$ where $m_e$ electron and $m_f$ are producing fermion masses.

Carrying out the calculations on the base of formula (4) at arbitrary polarization of initial colliding beams in the center-of- mass system we have the following expression for differential cross-section of the process (3):

$$\frac{d\sigma(\vec{s}_1, \vec{s}_2)}{dx d\Omega} = \frac{d\sigma}{dx d\Omega}\{1 + ((\vec{p}^0 \vec{s}_1) + (\vec{p}^0 \vec{s}_2))t_1 + [(\vec{s}_1 \vec{s}_2)\sin^2\theta + 2((\vec{p}^0 \vec{s}_1)(\vec{\chi}^0 \vec{s}_2) + \\ + (\vec{p}^0 \vec{s}_2)(\vec{\chi}^0 \vec{s}_1))\cos\theta - 2(\vec{\chi}^0 \vec{s}_1)(\vec{\chi}^0 \vec{s}_2)]t_2 + (\vec{p}^0 \vec{s}_1)(\vec{\chi}^0 \vec{s}_2)t_3\}, \tag{5}$$

where

$$\frac{d\sigma}{dx d\Omega} = \frac{G_F^3 m_Z^8}{6\sqrt{2}(4\pi)^3} \frac{(1 - 4r_f^2/x)^{1/2}}{(s - m_Z^2)^2 + m_Z^2\Gamma_Z^2} \cdot \frac{[(1 + r_H^2 - x)^2 - 4r_H^2]^{1/2}}{(x - m_Z^2/s)^2 + m_Z^2\Gamma_Z^2/s^2} T_0, \tag{6}$$

is cross-section of process (3) averaged and summarized by particle polarization. In (5) and (6) the following notations are accepted:

$$t_i = T_i/T_0 \qquad (i = 1,2,3)$$

$$\begin{aligned} T_0 &= (g_V^2 + g_A^2)(G_V^2 + G_A^2)\{4x(1 - 4r_f^2/x) + (1 + 2r_f^2/x)[4x + ((1 + r_H^2 - x)^2 - 4r_H^2)\sin^2\theta]\} + \\ &\quad + 24r_f^2(g_V^2 + g_A^2)(G_V^2 - G_A^2), \\ T_1 &= -2g_V g_A(G_V^2 + G_A^2)\{8x(1 - r_f^2/x) + (1 + 2r_f^2/x)[(1 + r_H^2 - x)^2 - 4r_H^2]\sin^2\theta\} - \\ &\quad - 48r_f^2 g_V g_A(G_V^2 - G_A^2)^2, \\ T_2 &= (g_V^2 - g_A^2)(G_V^2 + G_A^2)(1 + 2r_f^2/x)[(1 + r_H^2 - x)^2 - 4r_H^2], \\ T_3 &= T_0 - (1 + \cos^2\theta)T_2. \end{aligned} \tag{7}$$

In expressions given above $\vec{s}_1$ and $\vec{s}_2$ are unit vectors in the directions of electron and positron polarization correspondingly; $\vec{p}^0$ and $\vec{\chi}^0$ are unit vectors in directions of impulses of electron and $H$-boson correspondingly; $\theta$ is the angle between of $H$-boson and electron impulses; $r_H = m_H/\sqrt{s}$, $r_f = m_f/\sqrt{s}$. $x$ is the invariant mass of final fermion pair in $s$ units ($\omega$ is Higgs boson energy) that is limited from $4r_f^2$ up to $(1 - r_H)^2$.

$$x = \frac{(k_1 + k_2)^2}{s} = 1 + r_H^2 - \frac{2\omega}{\sqrt{s}} \tag{8}$$

Let's analyze the formula (5) in different cases of initial particle polarization.

Note that, in the cases of longitudinal and transverse polarization of initial beams, the differential cross-section of the energy-angular distribution of Higgs bosons was considered in [9], were calculations carried out for the values of $G_V = g_V, G_A = g_A$ and $r_f = 0$.

## 2. THE CASE OF UNPOLARISED COLLIDING BEAMS

1. In the case of unpolarized colliding beams, the differential cross-section of the process is determined by formula (6). Integrating the (6) over the angles we find the following expressions for differential cross-sections of distribution of final fermion couples on invariant mass:

$$\frac{d\sigma}{dx} = \frac{G_F^3 m_Z^8}{9\sqrt{2}(4\pi)^3} \frac{(1-4r_f^2/x)^{1/2}}{(s-m_Z^2)^2 + m_Z^2\Gamma_Z^2} \cdot \frac{[(1+r_H^2-x)^2 - 4r_H^2]^{1/2}}{(x-m_Z^2/s)^2 + m_Z^2\Gamma_Z^2/s^2} A_0, \tag{9}$$

where

$$A_0 = (g_V^2 + g_A^2)(G_V^2 + G_A^2)\{6x(1-4r_f^2/x) + (1+2r_f^2/x)[6x + \\ + (1+r_H^2-x)^2 - 4r_H^2]\} + 36r_f^2(g_V^2 + g_A^2)(G_V^2 - G_A^2). \tag{10}$$

The differential cross-section on invariant mass of $\mu^+\mu^-$ pair in (3) process without taking into consideration the particle polarizations is considered earlier in [5]. However, the formula $d\sigma(e^+e^- \to H\mu^+\mu^-)/dx$ in this work is obtained in case $G_V = g_V, G_A = g_A$ and $r_f = 0$. Moreover, this formula contains the series of inaccuracies, it is increased in 4 times and the second term of the last lines should have the form $2x(5 - m_H^2/s)$ in formula (2.2) of the given work.

The dependences of $d\sigma(e^+e^- \to H\mu^+\mu^-)/dx$ on $x$ at $m_H = 125$ $GeV$ for different values of $\sqrt{s}$ initial beam (here and below, the curves are constructed within the framework of the Weinberg-Salam model where $G_V = g_V = -1/2 + 2sin^2\theta_W, G_A = g_A = -1/2$, at the value of $sin^2\theta_W = 0,22$) are presented in figures 1, 2 and 3.

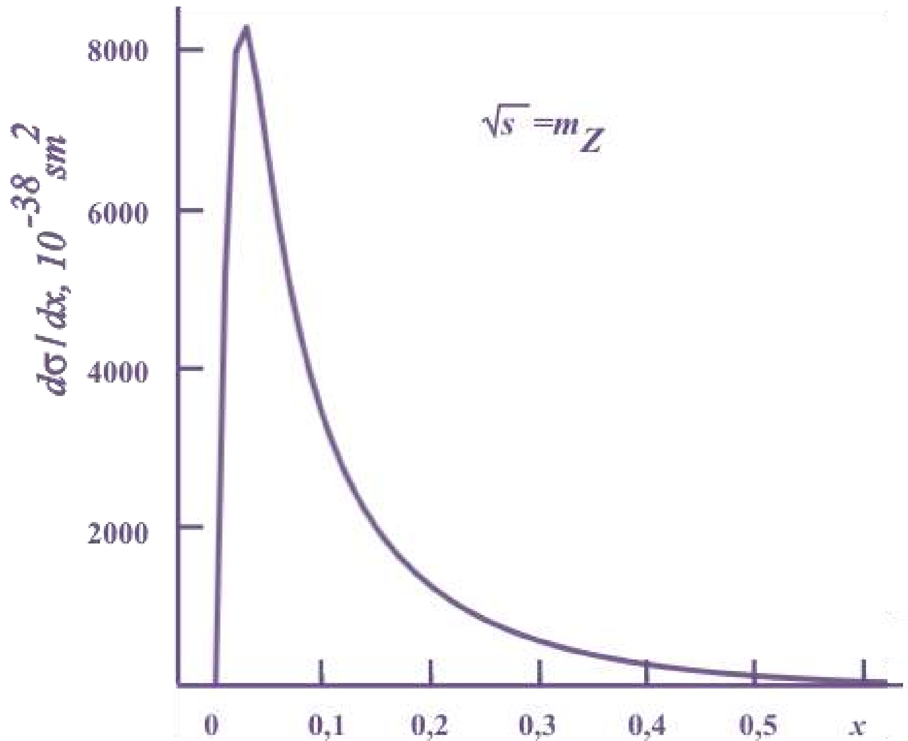


*Fig.1.* The dependence of differential cross-section of the (3) process on *x*.

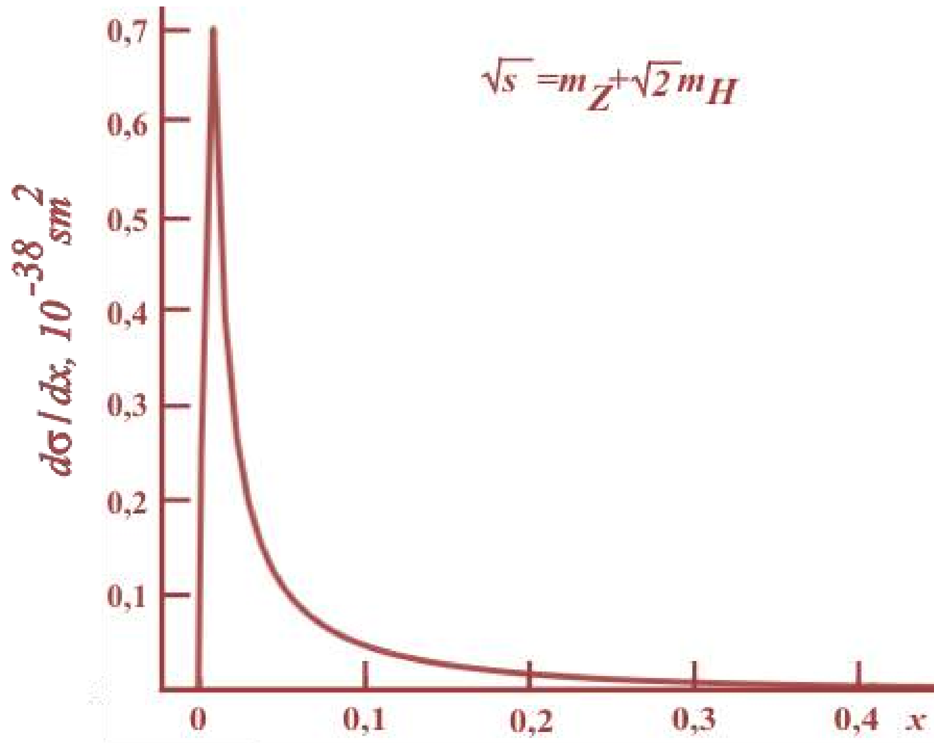


*Fig.2.* The dependence of the differential cross-section of the process (3) on *x*.

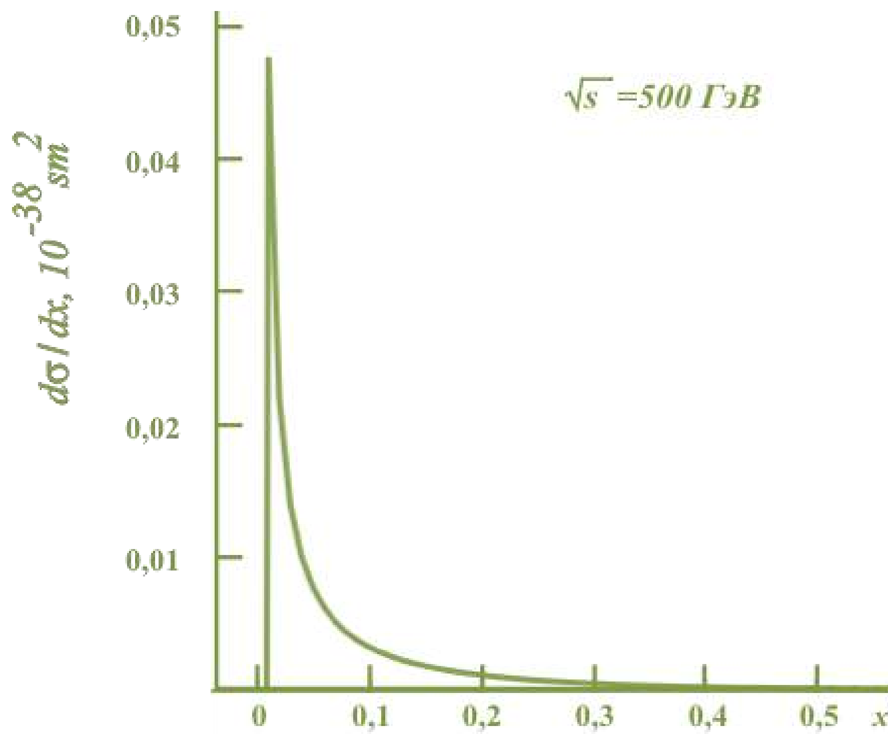


*Fig.3.* The dependence of the differential cross-section of the process (3) on *x*.

As one can be seen, from the figures in the differential cross-section (in $\sqrt{s}$ units) there is a maximum, and with increasing initial energy up to energy $\sqrt{s} = m_Z + m_H$ the place of the maximum shifts to the side of large values of $x$ and at energies $\sqrt{s} = m_Z + m_H$ it is determined by the value $x = m_Z^2 / s$.

As it was shown in [5], the detection of the Higgs bosons in the process under consideration is most favorable in the region $x > 0,5$, since in this case most of the background events are excluded. This specific behavior of the cross-section gives us to conclude that for the detection of the Higgs boson in the process under consideration with respect to the maximum of the differential cross-section, it is not necessary to increase the energy of the initial beams above the threshold of the main reaction $e^+e^- \to HZ$.

## 3. TOTAL PROCESS CROSS-SECTION

Let's consider the total cross-section of the process. Carrying out the rather complicated integration over the $x$ in (9), for the total cross-section of process (3) we obtain:

$$\sigma = \frac{G_F^3 m_Z^8}{9\sqrt{2}(4\pi)^3} \frac{(g_V^2 + g_A^2)(G_V^2 + G_A^2)}{(s - m_Z^2)^2 + m_Z^2 \Gamma_Z^2} [(1 - r_H^2)^2 J_0 + 2(5 - r_H^2) J_1 + J_2]. \tag{11}$$

The expressions of the quantities $J_0$, $J_1$ and $J_2$ appearing in (11) are the integrals of the form:

$$J_i = \int_0^{a_2} \frac{x^i \sqrt{(x - a_1)(x - a_2)}}{[(x - a)^2 + b^2} dx \qquad (i = 0,1,2), \tag{12}$$

Where

$$a_1 = (1 + r_H)^2, \quad a_2 = (1 - r_H)^2, \quad a = m_Z^2/s, \quad b = m_Z \Gamma_Z/s.$$

Theoretically calculated integrals have the following form:

$$\begin{aligned} J_0/2 &= -\rho_1 + C\tau_0 - A\tau_2, \\ J_1/2 &= -(2a - a_2)(\rho_1 + A\tau_2) + (a_1 - a_2)\rho_2 + (2a - a_1)C\tau_0, \\ J_2/2 &= (b^2 - 3a^2 + 2aa_2)(\rho_1 + A\tau_2) + (a_1 - a_2)(2a - a_1 - a_2)\rho_2 - \\ &\quad -(a_1 - a_2)^2 \rho_3 - (b^2 - 3a^2 + 2aa_1)C\tau_0. \end{aligned} \tag{13}$$

The following notations are accepted in (13):

$$\begin{aligned} \rho_1 &= \frac{1}{2} Ln[(\sqrt{a_1} - \sqrt{a_2})/(\sqrt{a_1} + \sqrt{a_2}), \rho_2 = \frac{1}{2}[\rho_1 - \sqrt{a_1 a_2}/(a_1 - a_2)], \\ \rho_3 &= \frac{3}{4}\rho_2 - \frac{1}{4}\frac{a_1\sqrt{a_1 a_2}}{(a_1 - a_2)^2}, \tau_0 = (T + L)/4F_1\sqrt{C}, \tau_2 = (T - L)/4F_1\sqrt{A}, \\ T &= -\frac{F_1}{F_2}[arctg \frac{\sqrt{Aa_2/a_1} - F_1}{F_2} + arctg \frac{\sqrt{Aa_2/a_1} + F_1}{F_2}], \\ L &= \frac{1}{2} Ln \frac{a_1\sqrt{C} - 2\sqrt{a_1 a_2}F_1 + a_2\sqrt{A}}{a_1\sqrt{C} + 2\sqrt{a_1 a_2}F_1 + a_2\sqrt{A}}, F_{1,2} = \frac{1}{\sqrt{2}}(\sqrt{AC} \pm B)^{1/2}, \\ A &= (a - a_1)^2 + b^2, B = (a - a_1)(a - a_2) + b^2, C = (a - a_2)^2 + b^2. \end{aligned} \tag{14}$$

In (11) we neglect the contribution of fermion mass.

The dependence of total cross-section of process (11) from $\sqrt{s}$ at $m_H = 125$ $GeV$ is presented in fig.4.

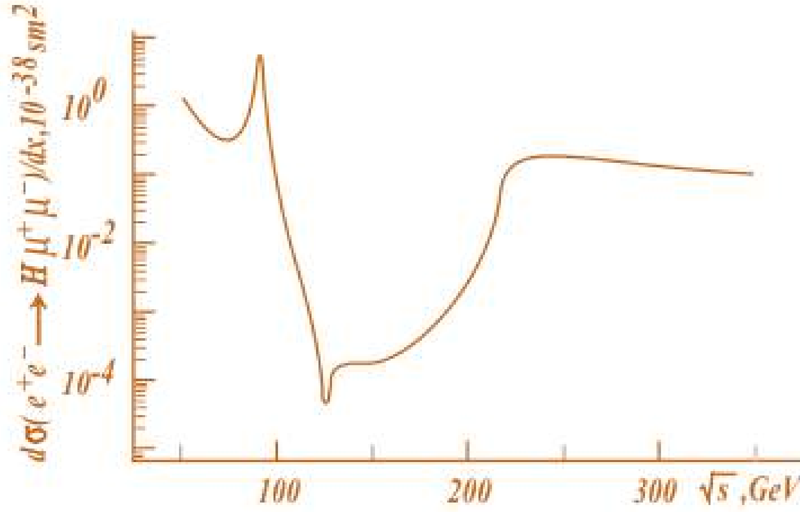


*Fig. 4.* The dependence of total cross-section of process $e^+e^- \to H\mu^+\mu^-$ on $\sqrt{s}$

As it is seen from the figure there are two maximums and two minimums in total cross-section of process (3). The first maximum is related to energy $\sqrt{s} = m_Z$ which corresponds to annihilation of $e^+e^-$ - pair by $e^+e^- \to Z \to HZ^* \to H\mu^+\mu^-$ scheme. The second maximum is related to energy of initial beams $\sqrt{s} = m_Z + \sqrt{2}m_H$ which corresponds to production of *HZ* - pair by scheme $e^+e^- \to Z^* \to HZ \to H\mu^+\mu^-$ and further decay of *Z*-boson.

The carried out analysis shows that second minimum corresponds to $\sqrt{s} = 125\ GeV$ of initial beam energy and in this case for the total cross-section we have $\sigma_{tot}^{2min} \approx 3{,}9 \cdot 10^{-42} cm^2$. The second maximum corresponds to energy of initial beams $\sqrt{s} = 245\ GeV$ at which for the total cross-section we have $\sigma_{tot}^{2max} \approx 2 \cdot 10^{-39} cm^2$.

The number of events of *HZ* - pair production by $e^+e^- \to Z^* \to HZ \to H\mu^+\mu^-$ scheme is given in Table 1.

Table 1

| *ILC energy* | *ILC luminosity, $L_{int}$* | *Number of events* |
|---|---|---|
| $\sqrt{s} = 245\ GeV$ | *250 $fb^{-1}$* | *M=Lσ=500 events* |
| $\sqrt{s} = 245\ GeV$ | *500 $fb^{-1}$* | *M=Lσ=1000 events* |
| $\sqrt{s} = 245\ GeV$ | *1000 $fb^{-1}$* | *M=Lσ=2000 events* |

From the Table 1 it is seen that number of events of Higgs boson production in the process $e^+e^- \to H\mu^+\mu^-$ on electron-positron collider ILC allows us to investigate Higgs boson various properties in detail.

Since in linear colliders ILC electrons and positrons will be longitudinally polarized, in this paper we will not consider the transverse polarizations of $e^+ e^-$ beams.

Note that the detail analysis of transversally polarized beams in process (3) is investigated in [7-8].

## 4. THE CASE OF LONGITUDINAL POLARIZATION OF COLLIDING $e^+e^-$ -BEAMS

In this case for the differential cross-section of the process (3) we have:

$$\frac{d\sigma(h_1,h_2)}{d\Phi} = \frac{d\sigma}{d\Phi}[1+(h_1-h_2)A_s - h_1h_2], \tag{15}$$

where $h_1$ and $h_2$ are longitudinal polarizations of electron and positron correspondingly. The formula (15) is applicable both to the differential cross-section in the variable $dxd\Phi$, and in variables $d\Phi$ and $dx$ variables separately.

Moreover in the case of $dxd\Phi = d\Omega$ we have $F = t_1$ (expression for the $t_1$ one can find in (7)) and in the case of $d\Phi = d\Omega$ we have.

$$A_s = -\frac{2g_V g_A}{(g_V^2 + g_A^2)}. \tag{16}$$

In the case $d\Phi = dx$ we have

$$A_s = A_1 / A_0, \tag{17}$$

where

$$\begin{aligned} A_1 &= -2g_V g_A (G_V^2 + G_A^2)\{12x(1 - r_f^2/x) + [(1 + r_H^2 - x)^2](1 + 2r_f^2/x)\} - \\ &- 72\, r_f^2 g_V g_A (G_V^2 - G_A^2), \end{aligned} \tag{18}$$

and $A_0$ is determined according to (10). The quantity $A_s$ determines the spin asymmetry due to the difference $(h_1 - h_2)$.

The effect of the electron beam polarization, determined according to:

$$N(h_1) = \frac{d\sigma(0,0)/d\Phi - d\sigma(h_1,0)/d\Phi}{d\sigma(0,0)/d\Phi + d\sigma(h_1,0)/d\Phi} \tag{19}$$

and found on the basis of formula (15), has the form

$$N(h_1) = -h_1 A_s/(2 + h_1 A_s) \tag{20}$$

The effect of positron beam polarization can be found from (20) by the substitution $h_1 \to h_2$.

It is easy to see that in case $r_f = 0$ the spin asymmetries $A_s$ in distributions on variables $dx$ and $d\Phi$ coincide, moreover $A_s = -23,7$ % at Weinberg angle $sin^2\eta = 0,22$. The effect of the beams polarization also has the same property, which at the value $sin^2\eta = 0,22$ is equal to: $N(h_1 = 1) = N(h_2 = -1) = 1\ \ 3$ %, $N(h_1 = -1) = N(h_2 = 1) = -10,6$ %.

Note that on ILC at $h_1 = 0,8$ the effect of electron beam polarization is equal $N(h_1 = 0,8) = 10,4$ % and at $h_2 = 0,5$ the effect of positron beam polarization is equal $N(h_2 = 0,5) = 0,56$ %.

Integrating the expression (9) over the all variables we have the following expression of the total cross-section of the process (3) in the case of longitudinal-polarized initial beams:

$$\sigma(h_1, h_2) = \sigma\left[1 - \frac{2g_V g_A}{(g_V^2 + g_A^2)}(h_1 - h_2) - h_1 h_2\right]. \tag{21}$$

## 5. ENERGY-ANGULAR DISTRIBUTION OF FERMIONS IN $e^+e^- \to Hf\bar{f}$.

Carrying out the calculations on the base of (4), for the arbitrary polarization of the initial colliding beams in the center-of-mass system, we have the following cross - section for the energy-angular distribution of fermions:

$$\begin{aligned} \frac{d\sigma(\vec{s}_1, \vec{s}_2)}{d\varepsilon d\Omega} &= \frac{d\sigma}{d\varepsilon d\Omega}\{1 + ((\vec{p}^0 \vec{s}_1) + (\vec{p}^0 \vec{s}_2))f_1 + [(\vec{s}_1 \vec{s}_2)sin^2\vartheta + \\ &+ 2((\vec{p}^0 \vec{s}_1)(\vec{k}^0 \vec{s}_2) + (\vec{p}^0 \vec{s}_2)(\vec{k}^0 \vec{s}_1))cos\vartheta - \\ &- 2(\vec{k}^0 \vec{s}_1)(\vec{\chi}^0 \vec{s}_2)]f_2 + (\vec{p}^0 \vec{s}_1)(\vec{k}^0 \vec{s}_2)f_3\}, \end{aligned} \tag{22}$$

where

$$\frac{d\sigma}{d\varepsilon d\Omega}=\frac{G_F^3}{2\sqrt{2}(4\pi)^4\varepsilon\beta^2}\frac{m_Z^8}{(m_Z^2-q_1^2)^2+m_Z^2\Gamma_Z^2}F_0, \tag{23}$$

is cross-section of the process (3) averaged and summed on particle polarizations. In (22) and (23) we introduce the following designations: $f_i=F_i/F_0$ $(i=1,2,3)$

$$\begin{aligned}F_0&=(g_V^2+g_A^2)(G_V^2+G_A^2)[\varepsilon(Q+R)(1-\beta^2\cos^2\vartheta)-2R]+\\&+8(g_V^2+g_A^2)(G_V^2-G_A^2)\varepsilon\beta^2r_f^2P-8g_Vg_AG_VG_AR\beta\cos\vartheta,\\F_1&=4G_VG_A(g_V^2+g_A^2)R\beta\cos\vartheta-2g_Vg_A(G_V^2+G_A^2)[\varepsilon(Q+R)(1-\\&-\beta^2\cos^2\vartheta)-2R]-16g_Vg_A(G_V^2-G_A^2)\varepsilon\beta^2r_f^2P,\\F_2&=(g_V^2-g_A^2)(G_V^2+G_A^2)(Q+R)\varepsilon\beta^2,\ F_3=F_0-(1+\cos^2\vartheta)F_2\end{aligned} \tag{24}$$

In the above mentioned formulae, $\vec{p}^{\,0}$ - and $\vec{k}^{\,0}$ - are the unit vectors in the directions of the electron momenta and the producing fermion correspondingly; $\vartheta$ - the angle of emission of the fermion with respect to the direction of the electron momentum, $\beta$ - the velocity of the producing fermion, $\varepsilon$ - its energy in units $\sqrt{s}/2$ which is limited from $2r_f$ up to $1-r_H^2-2r_fr_H$. The expressions for *P*, *Q* and *R* quantities are given in the appendix.

Note that in [10] a complete and all-lateral analysis of the energy-angular distribution of process (3) was carried out in the case of arbitrary polarized colliding beams (for small values of the Higgs boson mass).

In the case of unpolarized colliding beams, the energy-angular distribution of the producing fermions in the process (3) is determined by the formula (23). The analysis of the cross - section and other characteristics of the process (3) will be carried out below for the production of muons in the framework of the Weinberg-Salam model.

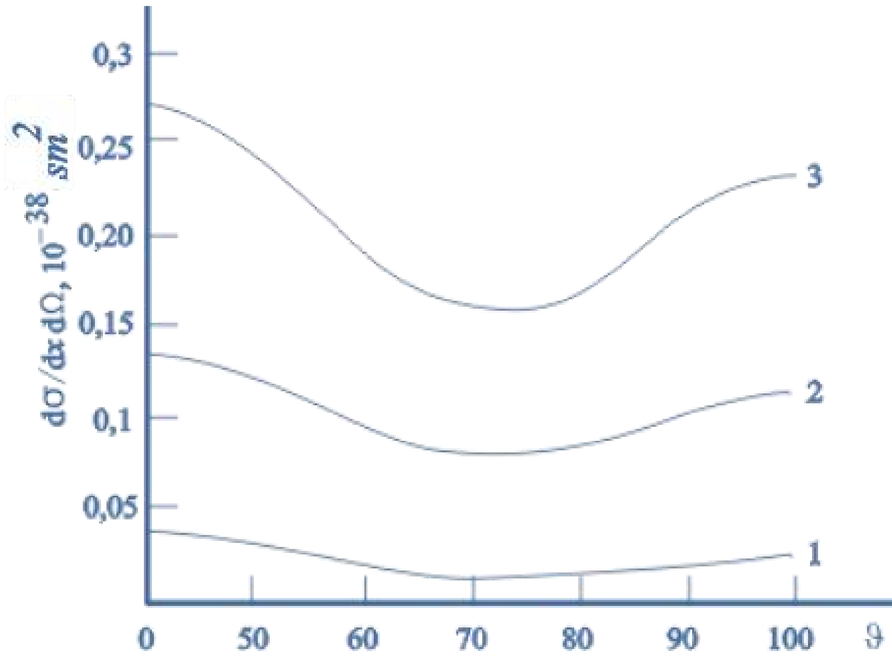


*Fig.5.*The dependence of energy-angular distribution on $\vartheta$

At $\sqrt{s}=m_Z$ and $m_H=175$ *GeV* the dependence of the cross-section $d\sigma(e^+e^-\to H\mu^+\mu^-)/d\varepsilon d\Omega$ on the muon emission angle $\vartheta$ for various values of $\varepsilon$ are presented in Fig. 5. The curves 1, 2 and 3 correspond to the values $\varepsilon=0.3$, 0.4, and 0.5. As one can be seen from Fig. 5, for a given value $\varepsilon$, the cross-section is larger for small

angles. We note that the initial energy is highlighted by the fact that the process under consideration occurs with the production of the $Z$- resonance, thus having the largest cross-section.

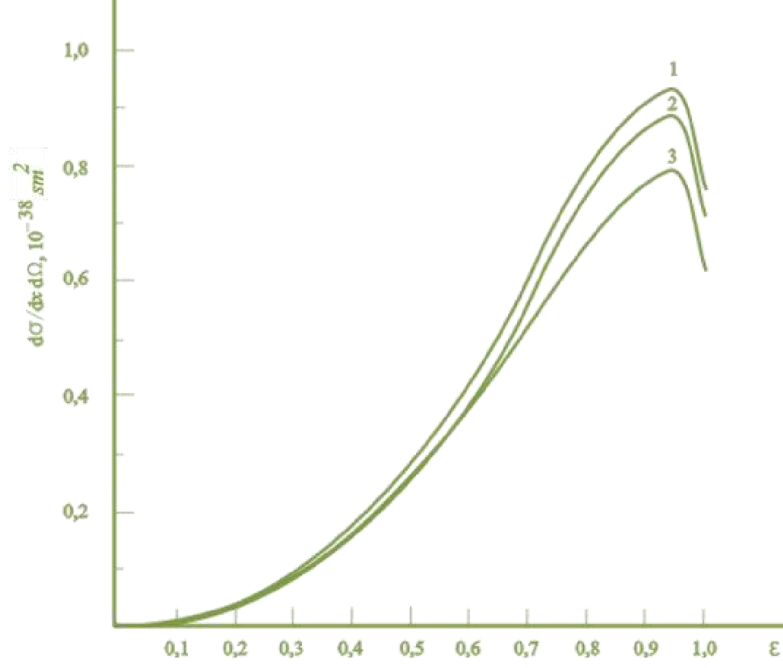


*Fig. 6.* Dependence of energy-angular distribution on $\varepsilon$

The dependence of cross-section $d\sigma(e^+e^- \to H\mu^+\mu^-)/d\varepsilon d\Omega$ on $\varepsilon$ at different $\vartheta$ (as in fig.5 at $\sqrt{s} = m_z$ и $m_H = 175$ GeV) is presented in fig.6. Curves 1,2 and 3 correspond to values $\vartheta = 5^\circ, 20^\circ$ and $35^\circ$.

The given work is supported by Science Development Foundation under the President of the Republic of Azerbaijan – **Grant № EİF-KETL-2-2015-1(25)-56/02/1.**

**APPENDIX**

At calculation of energy-angular fermion distribution in process (3) there are integrals of following type:

$$I_0 = \int \frac{1}{[(p_1 + p_2 - \chi)^2 - m_Z^2]^2 + m_Z^2 \Gamma_Z^2} \frac{d\vec{k}_2}{\omega_2} \frac{d\vec{\chi}}{\omega} \delta^4(k_2 + \chi - q), \tag{П.1}$$

$$I_\alpha = \int \frac{k_{2\alpha}}{[(p_1 + p_1 - \chi)^2 - m_Z^2]^2 + m_Z^2 \Gamma_Z^2} \frac{d\vec{k}_2}{\omega_2} \frac{d\vec{\chi}}{\omega} \delta^4(k_2 + \chi - q), \tag{П.2}$$

where $q = p_1 + p_2 - k_1$ .

For the calculation of the integrals (A.1) and (A.2), first of all, we give the region of admissible energy values of the Higgs boson (ω). Using the laws of conservation of energy and momentum in the process (3), we have (in the center-of-mass system of initial beams):

$$\omega_{max} = \sqrt{s} \frac{(1 - \varepsilon + r_H^2)(2 - \varepsilon) + \varepsilon\beta\sqrt{(1 - \varepsilon - r_H^2)^2 - 4r_f^2 r_H^2}}{4(1 - \varepsilon + r_f^2)},$$

$$\omega_{min} = \sqrt{s} \frac{(1 - \varepsilon + r_H^2)(2 - \varepsilon) - \varepsilon\beta\sqrt{(1 - \varepsilon - r_H^2)^2 - 4r_f^2 r_H^2}}{4(1 - \varepsilon + r_f^2)}.$$

Integrals (П.1) and (П.2) have the following form:

$$I_0 = \frac{2\pi}{s^2 \varepsilon\beta} P ,$$

$$I_\alpha = \frac{\pi}{s^2 \varepsilon^3 \beta^3} (Qk_{1\alpha} - Rq_\alpha ) .$$

Where

$$P = \frac{1}{\Gamma} [arctg \frac{2\omega_{max}/\sqrt{s} - (1 - r_Z^2 + r_H^2 )}{\Gamma} - arctg \frac{2\omega_{min}/\sqrt{s} - (1 - r_Z^2 + r_H^2 )}{\Gamma} ,$$

$$Q = (\varepsilon - 2r_f^2 )I_1 - 2(1 - \varepsilon + r_f^2 )I_2 , R = 2r_f^2 I_1 - (\varepsilon - 2r_f^2 )I_2 ,$$

$$I_1 = 2(1 - \varepsilon - r_H^2 + 2r_f^2 )P , \ I_2 = 2(r_Z^2 - 2r_f^2 )P - ln \frac{[2\omega_{max}/\sqrt{s} - (1 - r_Z^2 + r_H^2 )]^2 + \Gamma^2}{[2\omega_{min}/\sqrt{s} - (1 - r_Z^2 + r_H^2 )]^2 + \Gamma^2}$$

$$r_Z = m_Z/\sqrt{s} \ , \ \Gamma = m_Z \Gamma_Z /s .$$

---


[1] *A. Abada et all.* THE INTERNATIONAL LINEAR COLLIDER. Technical Design Report, Volume 2: Physics. EDMS Nr.: D00000001021165 Rev: A Ver: 1 Status: Released - for publication Dat.: 11. Jun 2013.

[2] *C. Quigg*. Particle physics after Higgs discovery: opportunities for the Large Hadron Collider. Contemporary Physics, v.57, p.177-187, 2016.

[3] *J. Ellis, M. K. Gaillard, D. V. Nanopoulos.* A Phenomenological Profile of the Higgs Boson**.** Nucl.Phys., B106, p.292-340, 1976.

[4] *R.L. Kelly, T. Shimada.* Dilepton signature in $e^+e^- \rightarrow Hl^+l^-$ . Phys. Rev., D23, p.1940-1956,1981.

[5] *E. Ma, J. Okada.* Possible means of detecting the Higgs boson in $e^+e^-$ annihilation. Phys. Rev. D 20, p.1052-1070,1979.

[6] *T. Morioka, M. Biyajima, O. Terazawa.* Detection of Light Standard Higgs Particle in $e^+e^-$ Annihilation. Prog. Theor. Phys 76 (5), p.1089-1097, 1986.

[7] *N.A. Guliev, I.G. Djafarov, V.Y. Faynberq, F.T. Xalil-zade.* YF, t.40, vip. 1(7), str.174-180. 1984. (In Russian).

[8] *N.A. Guliev, I.G. Djafarov, V.Y. Faynberq, F.T. Xalil-zade.* Kratkie Soobsheniya po Fizike, №11, str.35-40,1983. (In Russian).

[9] *Y. Abe et all.* Beam polarization effects on Higgs particle production in $e^+e^-$ annihilation. Lett. al Nuovo Cim. Volume 32, Issue 13, p. 361-365, 1981.

[10] *N.A. Guliev, I.G. Djafarov, F.T. Xalil-zade, P.Sh. Yaxyaev.* Preprint №107, Institut Fiziki AN Azerbaydjanskoy SSR, str. 1-23, Baku-1984. (In Russian).


*Received: 15.12.2017*

# PLASMA METHODS FOR NANOSTRUCTURING THE POLYMER MATRIX OF PIEZOELECTRIC NANOCOMPOSITES

**F.N. TATARDAR[1, 2]*, M. A. KURBANOV[1], N. A. SAFAROV[2], Sh. Sh. AMIROV[2,3], O. A. ALİYEV[1]**

*[1]G.M.Abdullayev Institute of Physics Azerbaijan National Academy of Sciences, Baku, AZ1143, H. Javid ave., 131, Azerbaijan*

*[2]Department of Electronics and Telecommunications, Khazar University, 41 Mehseti str., AZ 1096, Baku, Azerbaijan.*

*[3]Chair of Medical Physics and Informatics, Azerbaijan Medical University, Baku, Azerbaijan.*

**Author to whom correspondence should be addressed: E-mail: tatardar.farida@rambler.ru*

The actual problems of developing nanocomposites using gas discharge plasma in a dielectric system - dielectric - air gap - dielectric cylinder with a polymer solution are considered. In the conditions of simultaneous action of electric discharge plasma, temperature and nanoparticle ejection into the polymer solution, immobilization of nanoparticles was carried out.

**Keywords:** polymer composites, nanocomposites, electric discharge plasma, plasma assisted crystallization.
**PACS:** 83.85.Hf, 82.35.Np, 83.80.Tc.

## 1. INTRODUCTION

It is well-known that composites on the basis of rhombohedra, tetragonal, heterogeneous structure as well as polar and nonpolar polymers possess higher piezoelectric characteristics and can be employed as the converters of various purposes. These composites possess a higher sensitivity in the regime of receiving the acoustic waves. Main reason of this effect is sufficient higher piezo-modulus ($d_{ij}$) and lower dielectric permittivity so that the piezosensitivity is defined as $g_{ij}= d_{ij}/\varepsilon\varepsilon_0$. However the above described piezoelectric composites have a small efficiency in the regime of generation of acoustic waves because of relatively small value of Young's modulus ($Y^E$), coefficient of electro-mechanical binding and mechanical quality. The main reason of the lesser piezomodulus is an existence of subsurface polymeric phase formed as a result of thermal compressing on the surface of piezoelement. Numerous experimental results showed that the sub-electrode region always is the region enriched with polymer regardless of the obtaining technology of matrix composites. Existence of sub-polymeric layer is accompanied by decrease in mechanical and thermal properties of composite entirely. We may assume that, an achievement in the field of nanotechnology enables to obtain piezoelectric elements, energetic capacitive and low-power piezoelectric materials. [1-4,13]. It is well-known that the nanostructured polymer composites of various assignments have been recently developed. The scientific investigations are mainly doing in two directions:

1. Performance of nano-structuring in the process of polymers' synthesis;
2. Development of new piezoelectric materials on the base of the hybrid nano - and micro-sized piezoelectric composite materials like $Pb(ZrTi)O_3$.

Nanosized piezoelectric materials are synthesized by using $SiO_2$, $TiO_2$ and $BaTiO_3$ [5, 6]. It is worthy to note that, fabrication of nanoparticles on the basis of multicomponent Pb $(ZrTi)O_3$ ceramics is of particular interest, since they are good piezoelectric materials with high values of $d_{ij}$, $K_{ij}$, $Q_m$ ($d_{ij}$ is a piezo-modulus, $K_{ij}$ are refers to electromechanical coupling coefficient, and $Q_m$ indicates mechanical quality factor ). However, nowadays the reliable experimental results are absent in the literature on the synthesis of nanosized particles from the family of $Pb(ZrTi)O_3$.

The aim of our activities in this work is a development of plasma methods for immobilization of nanoparticles in the polymeric matrix of piezoelectric composites.

To achieve this aim following tasks were performed:

− Immobilization of nanoparticles and their uniform distribution in the polymer matrix (PVDF and LDPE) by simultaneous influence of the electrical discharge plasma and temperature;

− Development of a deposition technology for nanostructured polymeric solution on the surface of the piezoelectric substrate by simultaneous electrical discharge plasma exposure and temperature.

## 2. MATERIAL AND METHODS

We consider the matrix composites (0-3 type) on the basis of PKR-7M (tetragonal) type piezoelectric ceramics from family of lead zirconate titanate, thermoplastic polymer polyethylene of high density PEHD with a melt fluidity index of 1.3 g / 10 min (load- 2.0 kg, temperature 190°C) and silicon dioxide $SiO_2$ dielectric. Selection of carbon-chain polymer- polyethylene is related to the fact that it is characterized with high reproducibility due to its composition, structure and physical and chemical properties. A PKR-7M (PZT-5H) piezoceramic was selected due to its high piezoelectric modulus $d_{33}$ = 760 · $10^{-12}$ C/N),), Young's modulus ($Y_{11}^E$ = 0.57 · $10^{11}$ Pa) and dielectric permittivity ($\varepsilon_{33}/\varepsilon_0$ = 5 000). The silicon dioxide $SiO_2$ particles were used in spherical shape with density of 22 g/m$^3$, specific surface area of 200 m$^2$/g, and the electrical conductivity of $10^{-12}(\cdot m)^{-1}$. The plasma crystallization of composite promotes arising the active centers with physical and chemical nature in the polymeric phase [12-15]. Duration of discharge exposure

131 H.Javid ave, AZ-1143, Baku
ANAS, G.M.Abdullayev Institute of Physics
E-mail: jophphysics@gmail.com

was varied from 15 to 30 min. depending on the properties and volumetric content of polymer and piezoelectric ceramic in composite. A thickness of the gas gap, where micro-discharges were initiated was 0.5 - 4 mm. The voltage applied to the gas-insulator-composite system was $(3-20)$ kV [6-12]. Selected $SiO_2$ nanoparticles possess significant surface activity and enough high activity. The high surface energy of nanoparticles leads to unusual surficial properties and reactions. Therefore, one of the problems in the development of polymeric nanocomposites is effective dispersing, stabilizing the nanoparticles and preventing their mobilization in the polymer matrix of composite. Specified tasks were solved by employment the technology suggested by us for modification of polymeric phase; this consists of the crystallization starting at the melting temperature under effect of electric discharge plasma in electronegative gas electro-thermo-plasmonic crystallization of [1-7]. The stabilizing effect is explained by the formation of active centers of oxidation and submicro-size regions of stapling of macromolecules for localization of the dielectric nanoparticles owing to the effect of plasma of electric discharge in the polymeric phase of composite. This leads to the formation of a strong structure composed of $SiO_2$ particles as well as oxidized and cross-linked local regions of the polymer macromolecules. Wherein nanoparticles of dielectric occupy active sites in the polymer matrix without destroying the macrostructure of the piezoelectric composite. It should be pointed out that a strengthening of the polymer with dispersed nano fillers is a fundamental issue for the creation of polymer materials with various purposes [13-15]. Two main factors for strengthening are assumed to be the particle size or specific surface area of the filler and the polymer-filler binder [13]. Note that among all broad class of polymeric composites a new types of filled materials are polymeric nanocomposite in which one of the sizes (length, width and height) of dispersed phase does not exceed 100 nm at least [13]. Due to ultra-dispersive property of inorganic dispersant (filler), such systems may exhibit unusual electrical [11-15], mechanical [13], and thermo-physical [1-6,13] properties which do not possess microcomposites. The functional components of polymeric HC may be metals, dielectrics, semiconductors, and organic as well as inorganic substances [13]. For our studies it is necessary to use the dielectric ultra-dispersed particle as nano dispersant since electret , piezo – and pyro electric composites gain the mentioned properties after their electro-thermal polarization [1-15], which requires a high dielectric resistance and electrical strength. The above specified composites are obtained from a homogeneous powder mixture of components. The temperature and pressure for compressing of composites were selected within 437-463 K and 30 MPa respectively. The thickness and diameter of the piezo- composite were chosen as $250 \cdot 10^{-6}$ m, and $(160-200) \cdot 10^{-6}$ m respectively. Piezoelectric modulus of composites was determined in quasi-static mode, with an accuracy of 10%. Note that the thermal compressing process results in an additional purification of the composite from the solvent molecules and elimination of microphase separation of nano- and microcomposites at their intersection. Thus, a quasi-monolite structure is produced on the base of which the piezo electric converters of various purposes with high electromechanical and piezoelectric characteristics are prepared. The volume content of nanophase was varied in the range from 0.1 to 1%.

## 3. RESULTS AND DISCUSSION

The polymeric matrix materials proposed by us consist of a layer enriched by polymer phase dispersed by ferroelectric particles. Hybrid piezoelectric materials in turn, consist of the subsurface layer and the polymeric piezoelectric substrate. Nanostructured polymeric solutions are deposited on the surface of the piezoelectric substrate by employing chemical method. Thus, the polymer layer deposited on the surface of the piezoelectric substrate in the hybrid composite is a nanostructured composite. The dissolved polymeric layer deposited on the surface serves as a subsurface layer with high mechanical properties. The polymer- piezoceramic substrate in the hybrid composite serves as micro piezoceramics while the composite of polymer - $BaTiO_3$ as well as polymer - of $SiO_2$ corresponds to nanocomposite. Currently the microstructured polymer composites are well studied. It has been found that, a formation of the piezoelectric effect in the microstructured composites is mainly due to formation of a quasi-neutral system of polyer - ferroelectric ceramics. With the variation in size of piezo-phase particles, structure, volume, content and physico - chemical properties of components, as well as polarization conditions one can optimize the technological regimes for obtaining the piezoelectric composites. The effects of electron-ion and polarization processes on the piezoelectric properties are not studied enough. Therefore a piezoelectric, mechanical and electromechanical property of composites, as well as a production of a piezoelectric substrate is not sufficiently studied. The main reason of appearance of this effect is the presence of electrical and mechanical losses in the subsurface region of the composite element. It should be pointed out that the mentioned losses almost always occur in the piezoelectric elements independently on the fabrication technology of the elements. The main objective of the development of technology of hybrid piezoelectric materials fabrication of a piezoelectric substrate dispersed by of microsize particles of PZT. This is mainly due to the fact that the interfacial losses are noticeably reduced due to lack of a polymer-rich layer in the composite. In order to solve this problem, the modification of the surface layer by the electric discharge plasma is required.

The dielectric substrate modifications were carried out by effect of barrier discharge existed in the system of polymer - gas - polymer. These technological operations are performed as follows:

- The possibility of a uniform modification of the discharge of the composite;
- The possibility of varying the surface of the piezoelectric substrate with energy entering from the discharge channel up to the surface of the piezoelectric substrate;

- It is also necessary to develop the technology for uniform erosion of the polymer phase surface.

In Fig.1, the optical picture of the development of a barrier discharge channels is demonstrated. Fig. 1b shows the electric barrier discharge pattern. It is seen that the barrier discharge is discrete in time and space. As can be seen, micro-discharges arise in different sections of the surface of the dielectric substrate.

That is, the mentioned characteristics allow us to treat uniformly the surface of the dielectric substrate. In our experiments the voltage applied to the test cell was 20 $\cdot 10^3$ V, while the length of the plasma channel varied between 0.5-6 mm dependently on the experiment conditions.

It should be pointed out that, in the conditions of electric discharge plasma the modification piezo-substrate surface develops as follows:

− The substrate is subjected to the action of electrons and ions, ionizing radiation, and local discharge surface.

− The chemical factors in the process of etching of piezoelectric element surface are a thermal destruction, cut off the polymer’s main chain and the photo-destruction.

− The degree of etching under the influence micro-discharge is mainly determined by the energy transferred from the channel to piezo-substrate surface.

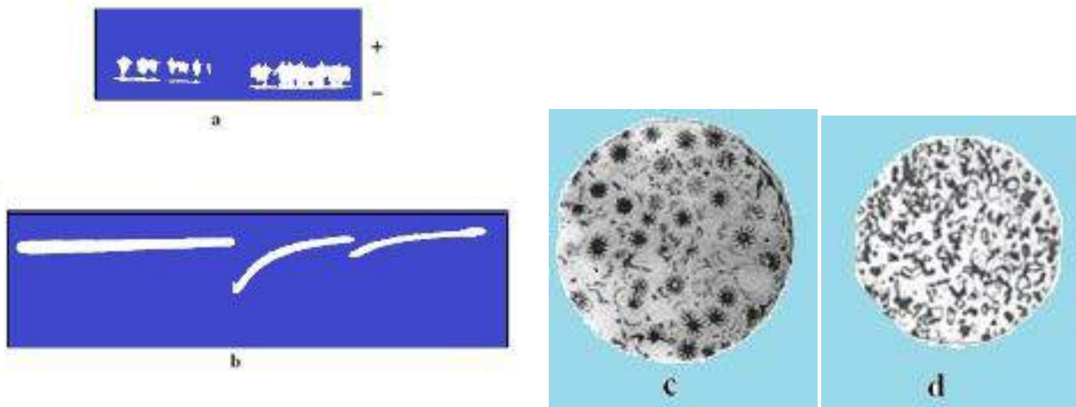


*Fig.1.* The test cell consists of a dielectric, gas layer and a dielectric. The micro-discharges appear under the influence of high voltages, which lead to erosion of the subsurface layer of composite.

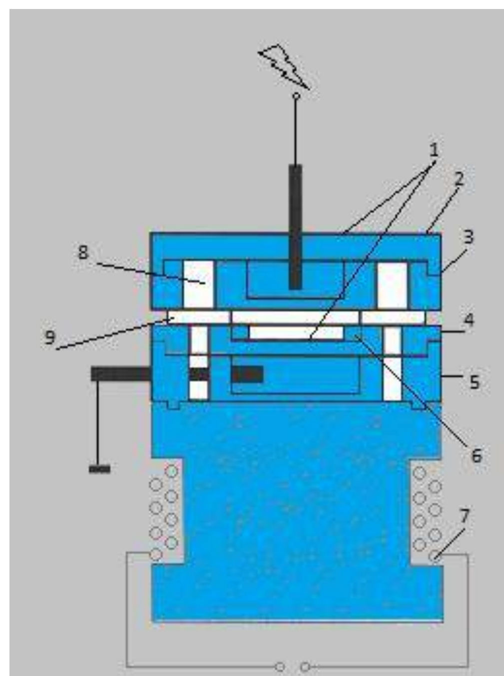


*Fig. 2.* A core proposed for nanostructuring of polymer solution .The core consists of a metal - dielectric - gas - polymer solution - piezoelectric substrate - metal structure:
1 - electrodes, 2 – dielectric safety washer, 3 - dielectric anode, 4 - dielectric cathode, 5 - insulator, 6 - metallic cylinder, 7 - heating element, 8 - leading, 9 – limiters of dielectric distance: $T_p$ =383 K; $t_p$ = 0.5 hours.

One can assume that etching of piezo-substrate surface occurs as a result of transfer of energy entering from the channel in the fields of contact between plasma and composite surface. Due to the local energy transfer, a heating of piezo substrate surface with subsequent erosion takes place.

It is known that, the electrons and ions of high energy, low molecular oxygen containing groups, atomic oxygen, ozone and ionizing radiation are synthesized in the plasma channel of barrier discharge. As a result, these physico- chemical processes including erosion provide uniform etching of the piezoelectric substrate. The next technological operation is a chemical deposition of previously nanostructured polymer solution on the substrate surface.

For this purpose a special dielectric core was constructed, which allows us to perform a plasma barrier discharge in it. The core consists of a metal electrode, dielectric substrate, an air layer, a polymeric solution and dielectric cathode.

Firstly, note that the immobilization of nanoparticles in polymeric phase is carried out by several methods:

1) Chemical method – inclusion of inorganic nano-particles into the polymer or obtaining and distribution of nanoparticles upon polycondensation, polymerization and copolymerization reactions.;

2) immobilization of nanoparticles in polymeric solution due to effect of acoustic waves.

3) immobilization of nanoparticles in polymeric solution by mechanical effects, e.g. under vibration.

4) immobilization of nanoparticles in polymeric solution due to the gas discharge (crown discharge).

Analysing of the above mentioned methods shows that the immobilization of nanoparticles in the polymer phase may be carried out by applying of these methods. However, the first method seems to be complicated in comparison with other mentioned methods. The second method is employed under realizing of the acoustic converters, which is constructively more complex and it is related to covitation effect. That is why immobilization implementation depends on the distribution of covitation centers. An energy released in the covitation process is not sufficient for immobilization and therefore it is impossible to increase and to regulate of energy in this process. It is difficult to provide the intencification of immobolization process by crown discharge, since one can not smoothly change the energy by increasing the voltage applied to channels of the crown discharge. An effective performance of the immobilization process under the mechanical vibrations is impossible, e.g. in the centrifugues.

In this work, a technology for effective performance of immobilization by using the barrier type electric gas discharge is developed. For this purpose, the following dielectric structure have been used : metal - dielectric - gas gap - polymer solution - dielectric - metal. The main aim in the selection of this system is the opprtunity of regulation of the released energy in the plasma channels upon gas discharge in the wide interval. Indeed, in the dielectric structure offered by us one can change parameters of gas discharge in the wide range by varying electrophysical parameters and geometrical sizes of dielectric, air gap, solution, and composite. One of the basic step of manufacturing of new type pieso-electrics on the base of hybrids of composites with polymeric matrix and nano and microsize phase is the obtaining of nanostructured polymeric solution, its deposition on the pieso electric substrate and prediction of physical characteristics.

Primaraly, a polymer solution is obtained in a solvent and then it is nanostructured under conditions of electrical gas discharge plasma with $BaTiO_3$ and $SiO_2$ nanoparticles of 70 nm sizes . As a solvent were taken toluene and kselol with boiling point >$100^0$ S. The solution process was carried out under combined effects of temperature and electric gas discharge plasma created by the sinusoidal voltage with $25{\cdot}10^3$ V voltage and 50Hz frequency. In order to accelerate the solution process of polymer in a solvent its macromolecules are divided into smaller segments under electric gas discharge and hence we provide the reasonable variant of polymer's solution in toluene. Destruction of the macromolecules is carried out by the combined effect of high energy electrons, ions; ionizing radiations synthesized in plasma channel as well as small molecule active compounds with oxygen origin. For this purpose a special experimental core was developed. Experimental core consists of metal - dielectric - gas - polymer solution - piezoelectric substrate - dielectric - metal system . The electric discharge is formed under influence of high voltage in the air gap between polymeric solution and dielectric anode. Thus, the polymer solution is continuously exposed to electric and gas discharge. The melting process of polymer in toluene and its next nanostructuring is carried out at the boiling temperature (20-40K) of solvent. One of the main next stages is an immobilization of pre-encapsulated $BaTiO_3$ and $SiO_2$ nanoparticles of of 60 - 70 nm sizes. In addition, it should be pointed out that the active gas products, ionizing radiations, high energy electrons, ions and mechanical waves are generated in the dielectric structure in the gap of dielectric-gas-polymeric solution due to electric duscharge in the gas phase. As a result, the immobilization process of nanoparticles breaks down and, nevertheless, the new immobilization centers can be created. One of the positive aspects of the use of dielectric structure is that there is an advantage of uniform distribution of plasma channels over its surface instead of their stabilization at certain point. The main reason of such distribution is the formation of electric charge spots on the dielectric surface whilst creation of every discharge channel. Stabilization of electric charges is observed at the contact region between channel and dielectric when each local discharge is created. Therefore, the second plasma channel is formed apart the first channel as soon as possible. Since this principle is valid also for the further micro discharges, this ultimately leads to uniform distribution of micro discharges over the dielectric's surface. (Figure 2). This means that the identical probability distribution of immobilization process is provided in the whole volume of polymer solution. In this case the volume of polymer solution undergoes the influence of electric gas discharge and possibility of mobilization of nanoparticles in this volume is destructed. To predict the nanostructuring of composites the TSD spectrum is used in this work. Our

activity can be summarized as follow: if an immobilization does not occur then the TSD spectrum obtained for microcomposites should not differ from that obtained for the element with the nanocomposite. This demonstrates that the nanoparticles added to polymer are mobilized as large clusters, i.e. they behave as a microparticle and therefore one can assume that the obtained TSD spectrum is similar to that obtained for the microcomposites. If a nanonostructuring of composite was already realized, then the TSC should be different and tempreture corresponding to the maximum of spectrum shifts toward its higher values. Therefore, in order to perform nanostructuring of the composites under investigation it should be found a certain relationship between this process and electric gas discharge obtained due to effect of higher voltage in the metal-dielectric-gas-solution-composite-metal structure used in producing of composite based hybrid systems.

A great significance has a prediction of influence of electric gas discharge formation in the dielectric structure, effect of liquid phase on the gas discharging parameters and influence of the electric gas discharging in the evaporation of liquid phase to the parameters of the plasma channels. For this purpose we use a Volt-Coulomb characteristic (Fig.3).

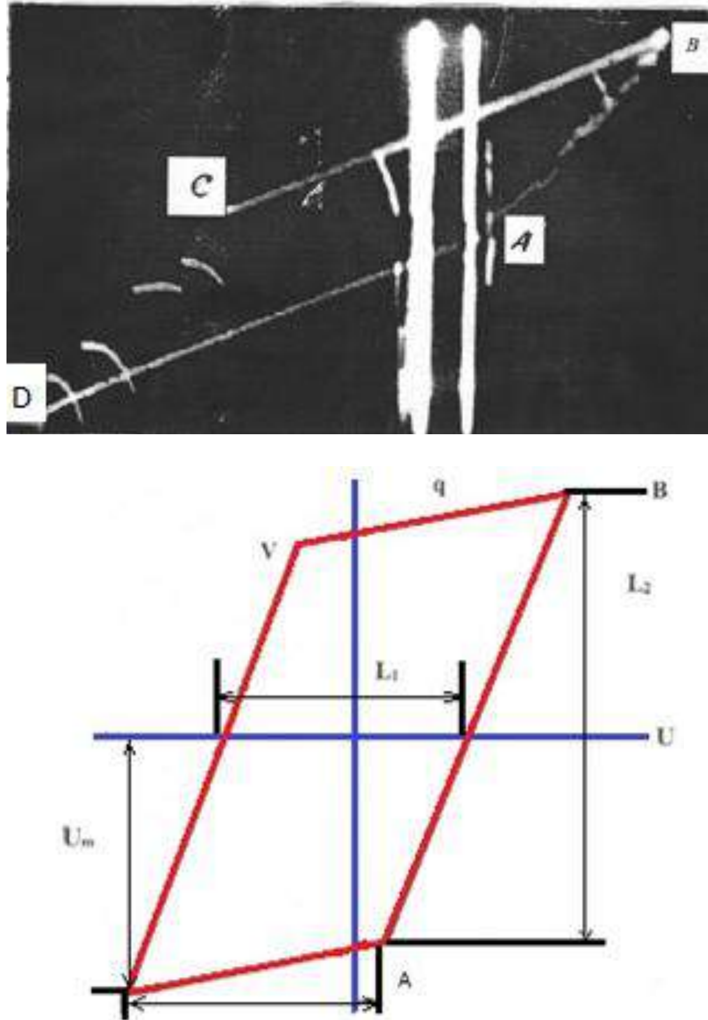


*Fig. 3.* Volt-Coulomb characteristic of the dielectric – air - polymer solution - piezo substrate - dielectric system corresponding to the core with a dielectric structure.

As it is seen from the Volt-Coulomb characteristic, the electric discharges in the dielectric structures under investigation have a dicrete chracter (Fig.1, a and b) . The liquid phase(solvent) evaporates under the combined influence of temperature and plasma, and it is deposited on the nanostructured polymer solution-composite system. During this process a variation in the thickness of liquid phase results in the following effects:

- A decrease in thickness with evaporation of liquid phase causes increase in its capasity and therefore a distributed voltage decreases gradually.

- The situation is oppositely for an air layer. A thicknes of air gap increases with evaporation of liquid phase and hence a voltage increases due to decrease of capasity.

The ignition voltage increases with increase of thickness of air gap.This causes the change of width of volt-coulomb characteristic.Therefore the volt-coulomb characteristic is used for diagnosis. Indeed, an increase in the width of Volt-Coulomb characteristic , a change in its height corresponding to the energy of further discharges and transferred charge quantity occurs. Therefore,

analysing Volt-Coulomb characteristics one can diagnose the electro-physical, electro-mechanical and electro-chemical processes occuring in the core under investigation.

If we accept that the volt - coulomb characteristic is simple and its parameters are valuable as a source of information, then the process of chemical deposition can be controlled by this method. In our experiments the time instant of a great significance is the accurate recording of the moment completion of the deposition process. Otherwise, an erosion processes will occur at the contact surfaces between electric gas discharge plasma channels and composite. To determine exact time instant of perfect vaporization of liquid phase as well as end of the deposition process following tasks were carried out:

− we determine ignition voltage of electric gas discharge in the metal - dielectric – air layer-liquid phase- composite-metal system;

− we determine ignition voltage of electric gas discharge in the system of metal-dielectric-air layer-composite-metal ;

− The greatest value of ignition voltage of the system studied is the voltage corresponding to the end of nanostructuring process.

The voltage circuit is automatically cutted off at this limit of width of volt-coulomb characteristic. As we noted earlier the ignitation voltage increases linearly (it is seen from figure) since the air layer thickness increases as the electrochemical deposition process is developed. Apart from the volt-coulomb characteristics a controlling scheme can be performed by the quantity of charge transferred in individual channels of electric gas discharge plasma , i.e. registration of current pulses.

Studies show that the nanostructuring of polymer phase that will be deposited on the composite can be provided through precisely regulation the vaporization temperature of nanaostructuring polymer solution as well as concentration of nanoparticles in solution in the investigated dielectric structure.

## CONCLUSIONS

Thus, the immobilization of nanoparticles in a polymeric matrix is carried out by plasma method in the following sequence:

4. A diagnosis of immobilization process of nanoparticles in solution is carried out by volt-coulomb characteristic.

5. Time instance corresponding to the maximum values of width (which corresponds to the ignitation voltage of electric discharge in a gas gap of core) and height of volt coulomb characteristic indicates a completion of both immobilization and nanostructuring.

---


[1] *M.A. Kurbanov, F.N. Tatardar, A.A. Mextili, I.S. Sultanaxmedova, G.G. Aliev, U.V. Yusifova.* Surface Engineering and Applied Electrochemistry, 2011, Vol. 47, No. 1, pp. 76-83.

[2] *M.A. Kurbanov, A.A. Bayramov, N.A. Safarov, F.N. Tatardar, A.A. Mextili, I.S. Sultanaxmedova.* Hybrid piezoelectric composites with high electromechanical characteristics. US Patent No.8,030,829 B1, 2011

[3] *M.K. Kerimov, A.A. Bayramov, A.A. Mamedov, A.I. Mamedov.* book 3. Book edited by John Cuppoletti, 2011, intect open Access publisher, pp. 375 – 404

[4] *M.A. Kurbanov, A.A. Bayramov, N.A. Safarov, F.N. Tatardar, I.S. Sultanakhmedova.* Scientific Israel – Technological Advantages, 2012, vol.14, no 1, pp. 1 -7

[5] *I.A. Starovoitova, V.G. Khozin, L.A. Abdrachmanova, O.Ye. Rodionova, A.L. Pomerantsev.* Journal Chemmometrics and intelligent Labaratory systems, 2009, v.97, p. 46 – 51

[6] *Y. Yi, S. Wolfgang, G. Rainer, Y. Zhong.* Journal of Central South University of Technology., 2005, v. 12, No 3, p. 324 – 328

[7] *V.E. Yudin, J.U. Otaigbe, A. Gladchenkos et.al.* New polyimide nanocomposites based on silicate type nanotubes: Dispersion, Processing and Properties, 2007, v.48, p. 1306 – 1315

[8] *Luana Persano, Andrea Camposeo, Dario Pisignano.* Progress in Polymer Science**,** Volume 43, April 2015, Pages 48–95

[9] *D.R. Paul, L.M. Robeson.* Polymer**,** Volume 49, Issue 15, 7 July 2008, Pages 3187–3204

[10] *Shivraj Puggal, Novepreet Dhall, Navjeet Singh and Manpreet Singh Litt.* Indian Journal of Science and Technology, Vol 9(4), DOI: 10.17485/ijst/2016/v9i4/81100, 2016

[11] *Levent Parali, Mirza A. Kurbanov, Azad A. Bayramov, Farida N. Tatardar.* Effects of, Journal of ELECTRONIC MATERIALS DOI: 10.1007/s11664-015-4010-3 2015 The Minerals, Metals & Materials Society. (Impact Factor: 1.798-SCI)

[12] *Havar A. Mamedov, Levent Paralı , Mirza A. Kurbanov, Farida.N. Tatardar, Azad A.Bayramov, İsrafil Şabikoğlu.* Piezoresistive and Posistor Effects in Polymer-Semiconductor and Polymer-Ferropiezoceramic Composite, 2016, том 50, вып. 5, c.633-638 (Impact Factor: 0.739-SCI)

[13] *A.D. Pomogailo, A.S. Rozenberg, and I.E. Uflyand,* Nanochastitsy metallov v polimerakh (Metal Nanoparti_cles in Polymers), Moscow: Khimiya, 2000.

[14] *M.A. Kurbanov, I.S. Sultanakhmedova, G.G. Aliev and G.M. Geidarov.* Piezoelectric Properties of Composites Polymer Piezoelectric Ceramic, Crystallized under Conditions of Effect of Plasma of Electric Discharge, Zh. Tekh. Fiz., 2009, vol. 79, no. 7, p. 63.

[15] *M.K. Kerimov, M.A. Kurbanov, F.G. Agaev, S.N. Musaeva and E.A. Kerimov.* Pyroelectric Effect in Composites, Crystallized under Conditions of Effect of Plasma of Electric Discharge, *Fiz. Tverd. Tela*, 2005, vol. 47, no. 4, pp. 686–690.


*Received:17.01.2018*

# THE SILVER SELENIDE SINGLE CRYSTAL GROWTH AND DEVICES ON ITS BASE

**G.S. HADJIEVA[1], F.A. KAZIMOVA[1], T.Sh. IBRAHIMOVA[1], K.O. TAGIEV[2], E.G. ASADOV[1]**

*[1]G.M.Abdullayev Institute of Physics Azerbaijan National Academy of Sciences, Baku, AZ1143, H. Javid ave., 131, Azerbaijan*

*[2] Institute of Catalysis and Inorganic Chemistry of Azerbaijan National Academy of Sciences, AZ1143, H. Javid ave. 29, Baku, Azerbaijan*

*E-mail: oktay58@mail.ru*

Silver selenide ($Ag_2Se$) single crystals on the base of which metal-semiconductor-metal (MSM) and metal-oxide-semiconductor (MOS) structures are prepared, grown by method of isothermal recrystallization from solid phase and their investigations in temperature interval 77 – 410K are carried out. It is shown that MSM structure W- $Ag_2Se$-W behaves itself as varistor and Ag-$Ag_2Se$-Ag structure behaves itself as diode in 376 – 400K region. The polar-dependent switching effect taking place in temperature interval 77-400K is obtained in MOS structure Al-$Al_2O_3$-$Ag_2Se$-Ag.

**Keywords:** crystal growth, diode, varistor, switching.
**PACS:** 41.52

## INTRODUCTION

The silver selenide ($Ag_2Se$) is included in number of semiconductors with narrow forbidden band and is related to group of semiconductor compounds of $A_2^I B^{VI}$ type with very interesting electrophysical properties many of which are studied by different investigators and obtained results are represented in the review in series of works [1-5]. In these and other works it is shown that $Ag_2Se$ has the two low-temperature (rhombic and tetragonal) and one high-temperature (cubic) modifications; the temperature of its polymorphous transformation varies in limits 126-133°C [6] and forbidden band width varies in limits 0,025-0.09 eV [7].

From the analysis of the reference it is revealed that single crystal silver selenide and also its possibility of its usage in the capacity of the main material in different semiconductor devices aren't studied enough [8 – 11].

The present work is dedicated to single crystal silver selenide growth and its application in different devices.

## EXPERIMENTAL TECHNIQUE

The method of isothermal crystallization from the solid phase is used by us for obtaining of $Ag_2Se$ single crystals. With that end in view the initial single crystal silver selenide synthesized from Ag-99,999 and Se-B5 and is put into quartz ampoule evacuated up to$10^{-5}$ millimeter of mercury the volume of which is chosen in definite ratio that causes the optimal conditions for the free crystal growing. The ampoule is treated by continuous vibration up to substance melting point at which it is endured during 30 – 40 minutes. Further the furnace is cooled with velocity 100 – 130 grad/h after which the ampoule is put from vertical furnace into horizontal one. The recrystallization process is carried out during 80 – 100 hours in isothermal conditions at 350-400°C. As a result the following fact is observed: the crystallization is begun from ampoule point in ampoule put along furnace, whereas the single crystals crystallize near with polycrystals in transversally put ampoule. $Ag_2Se$ single crystals of high purity with n-type conduction, concentration and mobility of electrons ~$10^{18}$ $cm^{-3}$ and ~ 2000 $cm^2$/V·sec correspondingly are obtained by the given method. The monocrystallinity of obtained crystal from which the sample is cut for electric measurements in the form of narrow parallelepiped, is tested by Laue method. Ag, W, Mo are applied in the capacity of metallic contacts. The sample forbidden band width defined from temperature dependence of electric conduction is equal to 0,008 eV.

## RESULTS AND DISCUSSION

The complex investigations of series of silver chalcogenide electric properties including $Ag_2Se$ carried by us during many years show that these compounds can be applied in computer engineering, automation devices in the capacity of commutators and also the multifunctional logic devices. The oscillogram of VAC of MSM-structure Ag-$Ag_2Se$ (single crystal) – Ag taken from ПНХТ-1 curve tracer screen in 77-410 K interval is shown in fig.1.

It is seen that VAC in 77 – 376K interval is ohmic and symmetrical at both polarities applied to voltage sample (a). VAC higher ~376K becomes asymmetrical one. i.e. behaves itself as diode.

Such state saves up to ~400K, i.e. the temperature of polymorphous transformation in $Ag_2Se$. The appearance of such "diode state" in $Ag_2Se$ single crystal in 376 – 400K interval is caused by the fact that the germs of new metastable tetragonal phase the specific resistance of which is bigger than the resistance of low-temperature modification appear in this temperature region inside low-temperature phase.

Thus, the contact of more high-ohmic (n) with low-ohmic tetragonal $Ag_2Se$ ($n^+$) takes place, i.e. $n^+$- n transition with current symmetrical dependence on voltage appears.

Further, the characteristics of varistor type is obtained on single crystal $Ag_2Se$ with tungsten and molybdenic contacts.

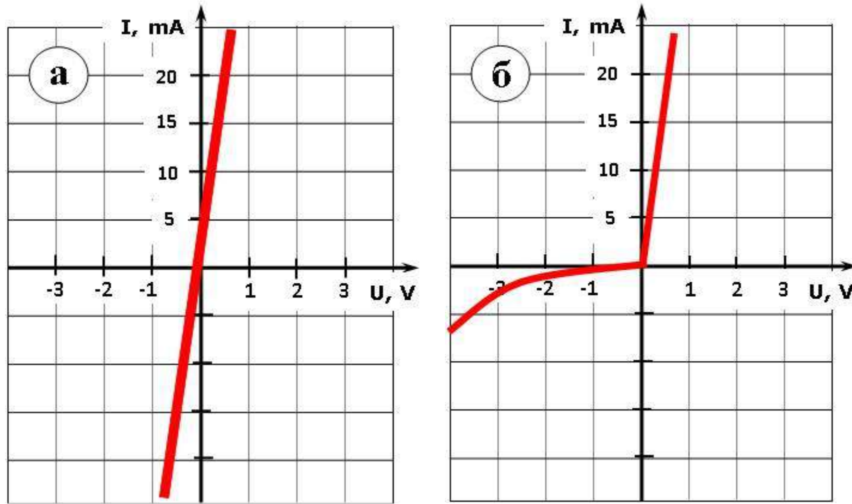


*Fig. 1.* The oscillogram of VAC of Ag- $Ag_2Se$ (single crystal) – Ag MSM-structure at - 376 (a) and 76-400K (b) (value of the big scale division horizontally is 1V, vertically is 5MA).

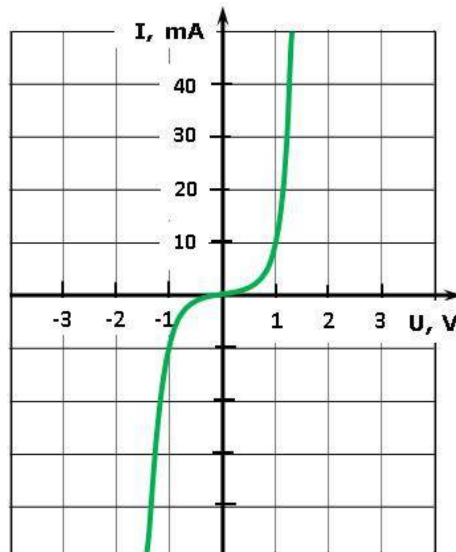


*Fig. 2.* The oscillogram of VAC of W- $Ag_2Se$-W varistor at room temperature. Scale: horizontally is 1V/grad and horizontally is 10MA/grad.

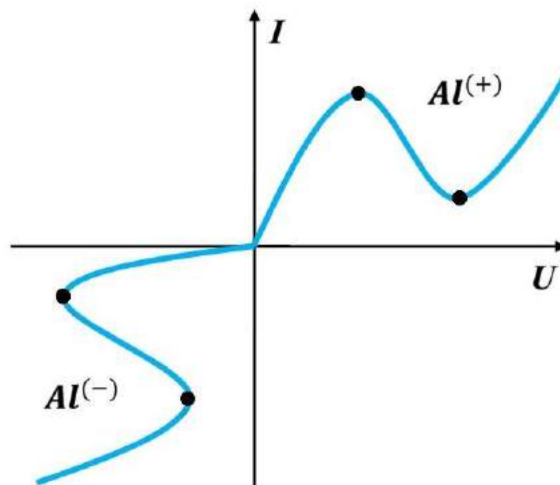


*Fig.3.* VAC symbolic representation with the negative-resistance region of Al-$Al_2O_3$-$Ag_2Se$-Ag structure.

VAC oscillogram of one of such varistors W-$Ag_2Se$-W taken at room temperature is presented in fig.2.

The nonlinearity factor (relation of static resistance to differential one) strives to eternity at small voltages. The mode of operation of such varistors is based on physical processes on contact metal – semiconductor of high purity. The low-voltage varistors can be applied in frequency multipliers, modulators, for voltage stability and etc.

The polar-dependent effect of switching and member (fig.3) [12] initiated by electron processes, i.e. by collisional ionization of band – deep trap level type is obtained in MOS-structures Al-$Al_2O_3$-$Ag_2Se$-Ag. The transient characteristics are defined: delay time ($10^{-6}-10^{-5}$ sec), turn-on time ($10^{-9}-10^{-8}$ sec) and number of switchings ($10^5$). Note that the observable phenomenon takes place in temperature wide interval (77 – 400K) with application of both polycrystal and single crystal $Ag_2Se$. As it is seen from fig.3 the transition of inductive (S-form) (III quadrant) into capacitive (N-form) (I quadrant) impedance at change of voltage polarity on Al electrode is observed. This structure can be used in logic and memory devices, in automatics and telemechanics because of control possibility by switching parameters.

## CONCLUSION

The single crystals of silver selenide ($Ag_2Se$) are grown by method of isothermal recrystallization from solid phase and MSM- and MOS-structures are prepared on their base. By investigation of VAC these structures in temperature interval 77 – 410K it is shown that MSM-structures W- $Ag_2Se$-W behave themselves as varistor, Ag-$Ag_2Se$-Ag structure behaves itself as diode and MOS-structure Al-$Al_2O_3$-$Ag_2Se$-Ag behaves itself as switching element with memory.

---


[1] *M. Xansen, K. Anderko.* Strukturi dvoynix splavov. T.1-2, Moskva. Metallurqizdat, 1962. (In Russian).

[2] *D.M. Chijikov, V.P. Chatliviy.* Selen I selenidi. Moskva, Izd-vo «Nauka», 1964. (In Russian).

[3] *N.X. Abrikosov, V.F. Bankina, L.B. Porechkaya, E.V. Skunova, S.N. Chijevskaya.* Poluprovodnikovie xolkoqenidi I splavi na ix osnove. Moskva, Izd-vo «Nauka», 1975. (In Russian).

[4] *Qorbachev V.V.* Poc. 5th Annu Int. Symp. Electron.Struct.Metals and Alloys, Gaubiq, 1975, Drezden, 1975.

[5] *G.S. Hadjieva.* Kandidatskaya dissertasiya, Baku. 1979. (In Russian).

[6] *K.P. Mamedov, M.D. Hadjiev, Z.D. Nurieva, Z.I. Suleymanov.* Kristalloqrafiya, 1974. 19. 1, 174. (In Russian).

[7] *V.V. Gorbachev, N.M. Putilin.* FTP, 1974. 8. 116, R. 2217-2219. (In Russian).

[8] *C.E. Gotliev* J.Phys.Chem.Sol., 1960. 15.P.183-187.

[9] *S.K. Sharma.* J. Mater.Sci., 1969. 4. N3.

[10] *Y. Bauer, G. Bush, C.Z. Frohlirch.* Naturforch, 1962. 17a, 10, P.886-890.

[11] *Yu.G. Asadov, G.A. Yabraibova*. Phys. Status.Solidi (a), 1972. 12. N1.P.13-17.

[12] *G.S. Hadjieva, I.A. Axmedov, N.N. Abdul-zade.* Injenerno-fizicheskiy jurnal, 2013. 86, №2, R.447. (In Russian).


*Received: 15.02.2018*

# DIELECTRIC PROPERTIES OF POLYMER COMPOSITES BASED ON HIGH-DENSITY POLYETHYLENE AND GALLIUM ARSENIDE

**N.N. GADZHIEVA[1], A.M. MAGERRAMOV[1], G.B. AKHMEDOVA[2]**

*[1]Instutute of Radiation Problems of NAS Azerbaijan, AZ1143, Baku, str.B.Vahabzade 9*

*[2] G.M.Abdullayev Institute of Physics Azerbaijan National Academy of Sciences, Baku, AZ1143, H. Javid ave., 131, Azerbaijan*

The dielectric properties of polymer composites based on high-density polyethylene (HDPE) and semiconductors of undoped (GaAs) and tellurium-doped gallium arsenide GaAs <Te> have been studied. The temperature and frequency dependences of the dielectric constant *ε (T, ν)* and the dielectric losses *tgδ (T, ν)* of the HDPE / GaAs and HDPE / GaAs <Te> compositions with different volume ratios of the components are obtained. It is shown that the changes in the dielectric properties of HDPE / GaAs and HDPE / GaAs <Te> compositions are due to the change in the supramolecular structure (SMS) of the polymer and are described by the two-phase Lichteneker model.

**Keywords:** polymer composite, high-density polyethylene (HDPE), semiconductors GaAs and GaAs <Te>, dielectric properties
**PACS:** 72.80.Tm.73.61.Ph.73.63.Eg

## INTRODUCTION

The production of new polymer compositions with distinctive electrophysical, spectral-luminescent, electrets and other properties [1-3] depends to a large extent on the nature of the filler, on the shape, size, distribution pattern and type of particle connectivity, and on the degree of interaction between the constituent components [4-8]. Usually, new fillers lead to the expansion of the possibilities of practical application of the composite material. From this point of view, polymeric composite materials such as polymer-semiconductor fillers are of particular interest [9-12]. The introduction of semiconductor fillers into the polymer matrix leads to a modification of its structure and properties. In this aspect, composites based on high density polyethylene (HDPE) with semiconductor compound GaAs are of interest. This is due to the fact that this semiconductor has a unique crystalline and band structure, is a promising material in micro and optoelectronics. [7] Since gallium arsenide GaAs, with a density of 5.31 g / cm$^3$ in the IR region (λ=1-12 μm) is optically anisotropic, for λ = 8 μm, the refractive index n = 3.34 is characterized by high thermal conductivity, magneto-optical, optical properties. Gallium arsenide is used in semiconductor lasers, diodes and other devices. Lasers have been created on the basis of heterostructures with one n-GaAs-p-GaAs-$Al_xGa_{1-x}As$ and two $Al_xGa_{1-x}As$-GaAs-$Al_xGa_{1-x}As$ heterojunctions. It should be noted that the production of GaAs layers, at present, is carried out by different methods; in the form of hybrid nanocomposites by sol-gel method or by molecular beam epitaxy method (MBE), etc. [8].

A nonmonotonic character of the dependence of the integrated impurity photoluminescence on the absorbed dose was found and the possibility of using GaAs <Te> as a dosimetric material in the region D <10$^6$rad was shown [9]. The problems of radiation defect formation, impurity photoluminescence and electrophysical properties of polymer/GaAs composites and polymer/GaAs<Te> are also poorly studied in heavily doped GaAs <Te> single crystals. The use of these materials as modifying additives for polymers can lead to the production of new composites with distinctive electrophysical, luminescent and mechanical properties. The choice of HDPE as a binder is due to the good knowledge of this polymer.

## EXPERIMENTAL METHOD

Homogeneous mixture from the HDPE powders and GaAs and GaAs <Te> semiconductors (with particle sizes~ 10 μm), was prepared by mechanical mixing in a ball mill. Then, the homogeneous mixture was hot-pressed at a temperature of T = 410 K with an exposure time of 15 minutes and cooled to room temperature for 30 minutes. This method makes it possible to obtain HDPE samples with a film thickness of 80-100 μm with a uniform distribution of semiconductor microparticles in the polymer volume [1], which seems to be a necessary factor for optical studies. Measurements of dielectric constant (ε), tangent of the dielectric loss angle (*tgδ*) and electrical conductivity ($ρ_v$) were carried out in the temperature range 290-410 K with linear temperature growth. Measurements of *ε* and *tgδ* were performed with the help of the E8-7 bridge at alternating current with frequency of 1 kHz.

## EXPERIMENTAL RESULTS AND DISCUSSION

Tables 1a and 1b show the temperature (a) and frequency dependences (b) of the dielectric constant of the HDPE / GaAs and Te-doped samples. It can be seen that the introduction of GaAs microparticles as a filler in HDPE leads to an increase in *ε* at the frequencies and temperatures tested. It is also seen from these tables that the doping of gallium arsenide with tellurium (GaAs <Te>) leads to some additional increase in the values of *ε* at a frequency of 10$^3$ Hz and a temperature range of 300-390 K. These and other changes in the structure of HDPE caused by the introduction of inorganic disperse fillers can be explained within the framework of the concept of a 3-phase structure (the presence of an interphase structure) in the supermolecular organization (NMA) of crystallizable polymers [1-10].

131 H.Javid ave, AZ-1143, Baku
ANAS, G.M.Abdullayev Institute of Physics
E-mail: jophphysics@gmail.com

Table 1 a.

The temperature dependences of dielectric constant *ε (T)* of the HDPE/GaAs and HDPE/GaAs<Te>

| Composites / ε | T,K ($\nu=10^3$Hz) | | | | | | | | | | | | |
|---|---|---|---|---|---|---|---|---|---|---|---|---|---|
| | 293 | 303 | 313 | 323 | 333 | 343 | 353 | 363 | 373 | 383 | 393 | 403 | 413 |
| 100%HDPE | 2,25 | 2,25 | 2,25 | 2,25 | 2,24 | 2,24 | 2,23 | 2,22 | 2,21 | 2,20 | 2,19 | 2,18 | 2,17 |
| 3%GaAs+97%HDPE | 2,52 | 2,52 | 2,52 | 2,52 | 2,51 | 2,51 | 2,5 | 2,48 | 2,47 | 2,45 | 2,44 | 2,43 | 2,4 |
| 7%GaAs+93%HDPE | 2,89 | 2,89 | 2,88 | 2,88 | 2,88 | 2,87 | 2,86 | 2,85 | 2,84 | 2,82 | 2,81 | 2,79 | 2,76 |
| 3%GaAs<Te>+97%HDPE | 3,02 | 3,01 | 3,01 | 3,01 | 3,01 | 3,00 | 2,99 | 2,98 | 2,97 | 2,95 | 2,95 | 2,93 | 2,93 |
| 7%GaAs<Te>+93%HDPE | 3,18 | 3,14 | 3,14 | 3,13 | 3,13 | 3,12 | 3,11 | 3,10 | 3,06 | 3,05 | 3,04 | 3,03 | 3,03 |

Table 1b.

The frequency dependences of dielectric constant *ε (ν)* of HDPE / GaAs and HDPE / GaAs <Te>

| Composites / ε | lgν, Hz | | | | |
|---|---|---|---|---|---|
| | $10^2$ | $10^3$ | $10^4$ | $10^5$ | $10^6$ |
| 100%HDPE | 2,25 | 2,25 | 2,22 | 2,21 | 2,31 |
| 3%GaAs+97%HDPE | 2,64 | 2,60 | 2,58 | 2,56 | 2,65 |
| 7%GaAs+93% HDPE | 3,07 | 2,97 | 2,92 | 2,90 | 2,99 |
| 3%GaAs<Te>+97% HDPE | 2,91 | 2,89 | 2,88 | 2,89 | 3,07 |
| 7%GaAs<Te>+93% HDPE | 3,08 | 3,04 | 3,02 | 3,02 | 3,24 |

The three-phase model of NMO-crystallizing polymers, in particular for HDPE, allows one to estimate the change in the glass transition temperature *Tc* when the polymer is modified by different fillers [1]. In filled HDPE at the boundaries of the polymer filler due to the nucleating activity of the fillers and their specific surface, the size of the spherulitic HMO polymer decreases and these changes of GaAs <Te> are undoubtedly reflected in the dielectric properties of the composites [1,3,12]. Similar changes in NMS of polypropylene binders were also noted in [13], where it was shown that the dielectric properties of *ε (T)* and *tgδ (T)* compositions based on polypropylene (PP) and $Na^+$ -montmorillonite are described by the Lichteneker model [13,14]. In particular, it was found that the value of *ε* decreases with increasing frequency to $6{\cdot}10^4$ Hz and then starts to increase. At high filler contents up to 30 wt% due to the increase in dipole-relaxation processes, the dielectric losses and conductivity of the composite as a whole also increase. According to the Lichteneker model [14-17], when the conductivity of the filler exceeds the values of the conductivity of the polymer, then the calculation of the values of $\varepsilon_k$. It can be seen from Tables 1a and 1b that the values of $\varepsilon_k$ and *tgδ* increase with an increase in the content of GaAs and GaAs <Te> fillers. $\varepsilon_k$ is realized as a static mixture, according to formula

$$lg\varepsilon_к = y_1 \cdot lg\, \varepsilon_1 + y_2 \cdot lg\, \varepsilon_2 \quad (1)$$

where $y_1$ and $y_2$ are the fraction of the components, $\varepsilon_1$ and $\varepsilon_2$ are the values of dielectric constant of the polymer and filler, respectively [17].

The $\varepsilon_k$ values of the samples of HDPE/GaAs and HDPE/GaAs <Te> compositions calculated from (1) are given in Table 2. In calculating the values of $\varepsilon_k$ for n-GaAs and n-GaAs <Te>, 11.2 and 12.8 were taken, respectively [7,8].

Tables 1a and 1b show that the values of $\varepsilon_k$ and tgδ increase with increasing content of GaAs and GaAs <Te> fillers. In addition, the doping of GaAs with Te atoms leads to an insignificant increase in $\varepsilon_k$, but there is a tendency to decrease dielectric losses.

Table 2.

Calculated values of $\varepsilon_k$ according to the Lichteneker model and the Maxwell-Wagner model and the values of $tg\delta$ at $10^3$ Hz quenched samples of HDPE / GaAs and HDPE / GaAs <Te>

| № | Composites | $\varepsilon_k$ | | $tg\delta$ |
|---|---|---|---|---|
| | | experimental | calculated[14] | |
| 1 | HDPE | 2,20 | - | 0,003 |
| 2 | HDPE +3 vol.% GaAs | 2,30 | 2,26 | 0,009 |
| 3 | HDPE +7 vol.%GaAs | 2,47 | 2,39 | 0,012 |
| 4 | HDPE+3 vol.% GaAs<Te> | 2,31 | 2,55 | 0,004 |
| 5 | HDPE +7 vol.% GaAs<Te> | 2,50 | 2,72 | 0,012 |

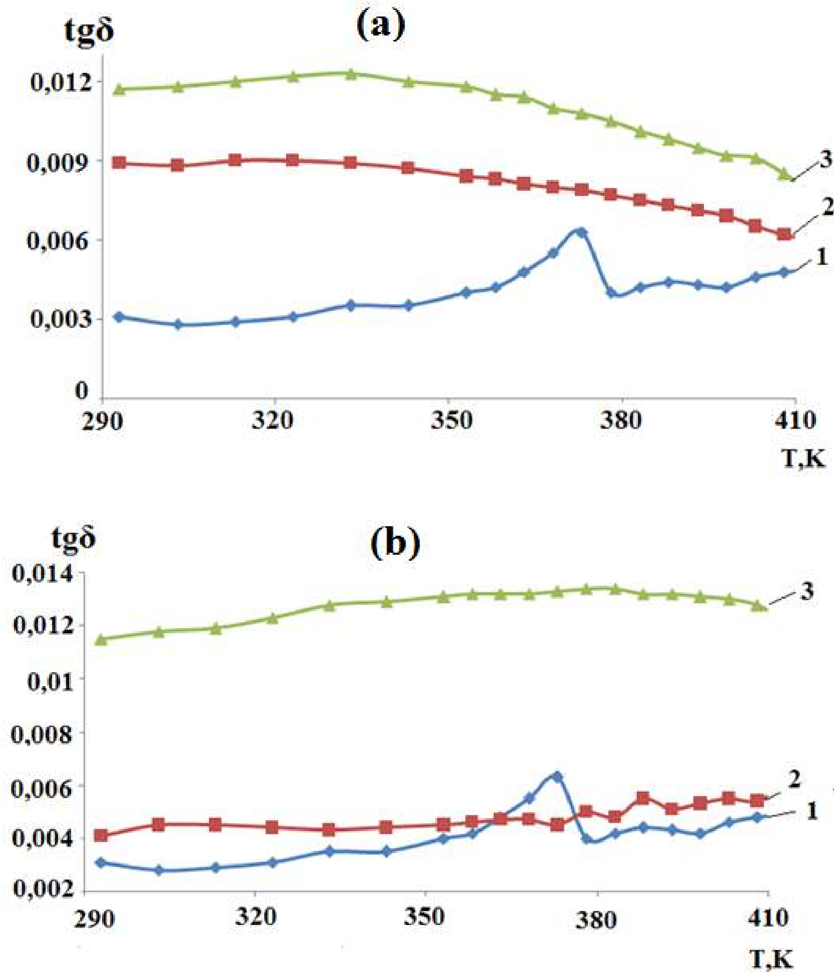


*Fig. 1.* The temperature dependences of the dielectric losses tgδ (T) of the HDPE / GaAs (a) and Te- doped samples of HDPE / GaAs <Te> (b) at 97: 3% (2) and 93: 7% (3) 1-100 vol. % HDPE

Figure 2 shows the frequency dependences of tgδ (ν) of HDPE / GaAs (a) and HDPE / GaAs <Te> (b) composites. It can be seen that for samples doped with Te atoms, an insignificant increase in tgδ is observed, and the nature of the frequency dependences does not change. At the same time, at doping frequences of $10^4$-$10^5$ Hz, doping leads to a slight decrease in dielectric losses (comparison of curves 3). At high frequences ($\nu>10^5$ Hz), dielectric losses are expected to increase somewhat. It should be noted that for the HDPE and Te alloyed samples the experimental values of dielectric losses tgδ and dielectric constant $\varepsilon$ are in accordance with the calculated values of $tg\delta$ and $\varepsilon$ for Te-doped atoms of HDPE / GaAs samples < Te>. While for the initial samples of HDPE / GaAs in the indicated frequency regions, it is more acceptable by the Maxwell-Wagner formula [14-15]:

$$\frac{\varepsilon-\varepsilon_2}{\varepsilon+\varepsilon_2} = \nu_1 \frac{\varepsilon_1-\varepsilon_2}{\varepsilon_1+\varepsilon_2} \qquad (2)$$

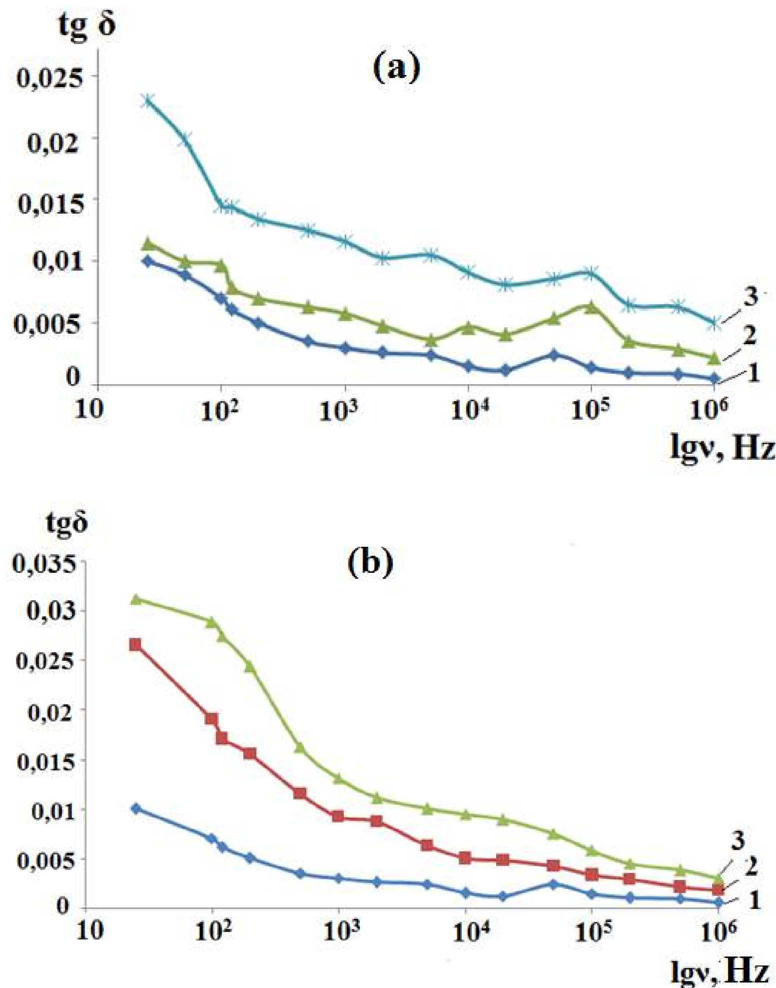


*Fig.2.* Frequency dependences of dielectric losses tgδ (ν) of HDPE / GaAs (a) and HDPE / GaAs <Te> (b) composites at 97: vol.3% (20 and 93: 7 vol.% (30.1 - 100 vol.% HDPE)

It is seen from Fig. 2 that for Te-doped samples dielectric losses in the resonant frequency range $5 \cdot 10^4$ - $10^5$ Hz decrease. At the same time, at low frequencies, a certain increase in dielectric losses is observed in doped samples.

The observed changes in the dielectric properties of composites according to the three-phase structure of crystallizable polymers in composites PE / GaAs (a) and PE / GaAs <Te> (b) and GaAs, as doped with Te, create new crystallizing regions due to the formation of less ordered new phase.

Indeed, by determining by the method of radio-thermoluminescence (RTL) the position of the β-transition, HDPE at 228 K [3,9] is shifted by 4-5° to the high-temperature side, and this fact explains only by the three-phase structure of the crystallized filled polymers.

## CONCLUSION

The dielectric properties of polymer composites based on high-density polyethylene (HDPE) and semiconductors of undoped (GaAs) and tellurium-doped gallium arsenide GaAs <Te> are investigated. The temperature and frequency dependences of the dielectric constant *ε (T, ν)* and the dielectric losses *tgδ (T, ν)* of the HDPE / GaAs and HDPE / GaAs <Te> compositions with different volume ratios of the components are obtained. The values of the dielectric constant are calculated, which are compared with the experimental values *ε (T, ν)*. It is shown that the changes in the dielectric properties of these compositions are due to a change in the supramolecular structure (NMS) of the polymer and are described by the two-phase Lichteneker model.

[1] *N.R.Ponomareva, G.P.Goncharuk, E.S. Obolonkova, Yu.M. Budnickij, O.A. Serenko*. Properties of composites based on polyethylene Chemical industry today. 2010. No. 5. p. 37-42.

[2] *N.R. Ponomareva, T.K. Bajramkulova, N.D.Goncharuk etc.* Invloed dispersie van houtvuller op die vorm wat in composites gebaseer op hoë digtheid poliëtileen gegenereer. Plast. Massa. 2010 No 10.

[3] *A.M. Magerramov*. Structural and Radiation Modification of Electret, Piezoelectric Properties of Polymer Composites, Baku, Elm, 2001, 3265p.

[4] *P.V. Morozov, E.I. Grigoryev, S.A. Zavianov*. Optical properties of hybrid nanocomposites of

poly-n-phenylene-vinylenylene-sulphide of cadmium . JTF, 2013, vol. 83, No.3, p.101-106.

[5] *M.I. Aliev, N.N. Gadzhieva, G.B. Akhmedova.* FT-Fourier spectroscopic study of the structure of polyethylene composite films containing GaAs and GaAs (Te). Polymer Science, ser.A, v.58, №3, 2016, p.293-297.

[6] *K.V. Shalimova.* Physics of semiconductors, Izd.Lan, 2010, 400p.

[7] *V.V. Starostin.* Materials and methods of nanotechnology, Izd. 'Binom', M, 2nd ed., 2010, 431 p.

[8] *V.N. Dubovik.* Detectors of gamma-radiation based on GaAs: Te single crystals, Proceedings of the International Conf. "Opto-nanoelectronics, nanotechnologies and microsystems", Ulyanovsk, 2005, p.141.

[9] *Kh.V. Bagirbekov, A.E. Chebotarevsky, A.M. Maharramov, A.I. Abdullaeva.* On the structure of interphase layers and features of radio-thermoluminescence of polyethylene compositions with divinylstyrene elastomer DST-50. Problems of Power Engineering, 2011, №4, p. 44-51.

[10] *IL Dubnikova, N.F. Kedrina, A.B. Soloviev and etc.* The influence of the nature of the filler on the crystallization and mechanical properties of the filled polypropylene Polymer Science, 2003, vol. 45, No. 3, p.468-475.

[11] *A.M. Magerramov, R.L. Mamedova, I.M. Ismayilov, Kh.V. Bagirbekov.* Dielectric properties of nanoparticles of polypropylene nanoglyn type Na + -montmorillonite in heating-cooling mode. JTF, 2017, No. 9, p.1367-1371.

[12] *D.F. Rustamova, A.M. Magerramov, Kh.V. Bagirbekov, M.A. Nuriev.* Dielectric properties and radiothermoluminescent features of polypropylene $\alpha$-$Al_2O_3$, highly filled compositions, Surface Engineering and Applied Electrochemistry, 2013, vol. 49, No. 2, pp.176- 179.

[13] Electrical properties of polymers, Ed. B.I. Sazhina, Chemistry, L, Third ed., 1986. S.80-128.14.

[14] *C.K. Chiang and R. Popiclarz.* Polymer composites with high dielectric constant. Ferroelectrics, 2002, v.275, pp.1-9.

[15] *R. Tomas, S. Satapathy, K. Dwarakanath, K.B.R. Varma.* Express polymer letters, 2010, v.4, №10, pp.632-643.

*Received:13.02.2018*

# THE PRODUCTİON OF THE HIGGS BOSON AND $t\bar{t}$ -PAIR İN POLARIZED $e^{-}e^{+}$ -BEAMS

**S.K. ABDULLAEV[1,a], M.Sh. GOJAYEV[1,b], N.A. NASIBOVA[1,b], G.A. SOLTANOVA[1,c]**
*[1]Baku State University, Azerbaijan, AZ 1148, Baku, Z. Khalilova str., 23,*
*[a]sabdullayev@bsu.edu.az, [b]m_qocayev@mail.ru, [c]guneshsoltanova@mail.ru*

In the framework of the Standard (Minimal Supersymmetric Standard) model the process of the Higgs boson and heavy $t\bar{t}$ -pair production in arbitrarily polarized colliding electron-positron beams $e^{-}e^{+} \to H_{SM}t\bar{t}$ ($e^{-}e^{+} \to Ht\bar{t}$, $e^{-}e^{+} \to ht\bar{t}$) is considered. The characteristic features in the behavior of cross sections and polarization characteristics (left-right spin asymmetry, transverse spin asymmetry) are investigated and revealed, depending on the Higgs boson energy and the invariant quark mass.

**Keywords:** Standard model, Higgs boson, quark pair, left and right coupling constants, Weinberg parameters.
**PACS:** 12.15-y, 12.15 Mm, 14.70 Hp, 14.80 Bn.

## 1. INTRODUCTION

The Standard model (SM), based on the local gauge symmetry group $SU_C(3)\times SU_L(2)\times U_Y(1)$ describes well the physics of strong, electromagnetic and weak interactions between leptons and quarks [1-3]. A doublet of scalar fields $\varphi = \begin{pmatrix} \varphi^{+} \\ \varphi^{0} \end{pmatrix}$ is introduced into the model, the neutral component of which has a vacuum value different from zero. As a result of spontaneous symmetry breaking due to quantum excitations of the scalar field, a new particle appears – the scalar Higgs boson $H_{SM}$, and due to interaction with this field gauge bosons, quarks and charged leptons acquire mass. Recently a scalar Higgs boson has been discovered at the LHC collider by the ATLAS and CMS collaborations [4, 5] (see also the reviews [6-8]). In this connection, the theoretical interest in the various channels for the production and decay of the Higgs boson has greatly increased [9-15].

Along with SM, the Minimal Supersymmetric Standard Model (MSSM) is widely discussed in the literature [16]. Here two doublets of the scalar field are introduced and after spontaneous symmetry breaking there appear five Higgs particles: CP-even *H* and *h* bosons, CP-odd *A*-boson and charged $H^{+}$, $H^{-}$ bosons.

In recent papers [10, 13], we studied the production of the Higgs boson and the light fermion pair $f\bar{f}$ ($f\bar{f} = \nu_e\bar{\nu}_e, \nu_\mu\bar{\nu}_\mu, \nu_\tau\bar{\nu}_\tau, \mu^{-}\mu^{+}, \tau^{-}\tau^{+}, d\bar{d}, s\bar{s}, c\bar{c}, b\bar{b}$) under the collision of an arbitrarily polarized $e^{-}e^{+}$-pair. In the present paper, we investigate the process of the Higgs boson $H_{SM}(H,h)$ and heavy quark pair $t\bar{t}$ production in annihilation of an arbitrarily polarized electron-positron pair:

$$e^{-}+e^{+} \Rightarrow H_{SM}+t+\bar{t},$$
$$e^{-}+e^{+} \Rightarrow H+t+\bar{t}, \tag{1}$$
$$e^{-}+e^{+} \Rightarrow h+t+\bar{t}.$$

## 2. THE RADIATION OF HIGGS BOSON BY A VECTOR Z-BOSON

Due to a rather strong connection with the vector Z-boson, the main source of the production of scalar bosons is their emission by the Z-boson, which is produced in colliding electron-positron beams. This process is described by the Feynman diagram shown in Fig. 1, where four-dimensional momenta of the particles are written in the parentheses and also the four-dimensional electron ($s_1$) and the positron ($s_2$) spins.

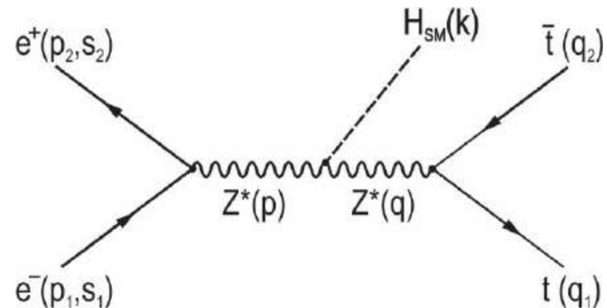


*Fig. 1.* The Feynman diagram of the reaction $e^{-}e^{+} \to H_{SM}t\bar{t}$.

It is known that the interaction Lagrangians $e^{-}e^{+}$ ($t\bar{t}$) with the Z-boson and the Z-bosons with the scalar Higgs boson $H_{SM}$ are written in the form [1-3]

$$L_{eeZ} = \frac{e}{2\sin\theta_W\cos\theta_W}[g_L(e)\bar{e}\gamma_\mu(1+\gamma_5)e + g_R(e)\bar{e}\gamma_\mu(1-\gamma_5)e]Z_\mu,$$

$$L_{t\bar{t}Z} = \frac{e}{2\sin\theta_W \cos\theta_W}[g_L(t)\bar{t}\gamma_\mu(1+\gamma_5)t + g_R(t)\bar{t}\gamma_\mu(1-\gamma_5)t]Z_\mu, \quad (2)$$

$$L_{ZZh} = \frac{e}{\sin\theta_W \cos\theta_W} M_Z Z_\mu Z_\rho g_{\mu\rho} H(k).$$

Here $M_Z$ is the mass of the $Z^0$-boson,

$$g_L(e) = -\frac{1}{2} + \sin^2\theta_W, \quad g_R(e) = \sin^2\theta_W,$$
$$g_L(t) = \frac{1}{2} - \frac{2}{3}\sin^2\theta_W, \quad g_R(t) = -\frac{2}{3}\sin^2\theta_W \quad (3)$$

are left and right coupling constants of an electron and a $t$-quark with a $Z^0$-boson, $\theta_W$ is the Weinberg angle

On the basis of the Lagrangians (2) we write the matrix element corresponding to the diagram in Fig. 1:

$$M = -i\left(\frac{e}{2\sin\theta_W \cos\theta_W}\right)^3 2M_Z D_Z(s) D_Z(xs)\times$$

$$\times[\bar{\upsilon}(p_2,s_2)\gamma_\mu(g_L(e)(1+\gamma_5) + g_R(e)(1-\gamma_5))u(p_1,s_1)]\times$$

$$\times[\bar{u}(q_1)\gamma_\mu(g_L(t)(1+\gamma_5) + g_R(t)(1-\gamma_5))\upsilon(q_2)], \quad (4)$$

where

$$D_Z(s) = \frac{1}{s - M_Z^2}, \; D_Z(xs) = \frac{1}{xs - M_Z^2}, \quad (5)$$

$s = (p_1 + p_2)^2$ is the square of the total energy of the electron and positron in the center of mass system, $x$ is the invariant mass of the *t*-quark pair in units of *s*

$$x = \frac{(q_1+q_2)^2}{s} = 1 - \frac{2E_H}{\sqrt{s}} + \frac{M_H^2}{s}, \quad (6)$$

$E_H$ and $M_H$ are energy and mass of a scalar boson $H_{SM}$.

The square of the matrix element (4) is given by:

$$|M|^2 = \left(\frac{e^2}{4x_w(1-x_w)}\right)^3 \cdot 4M_Z^2 D_Z^2(s) D_Z^2(xs)\cdot T_{\mu\nu}^{(1)} \cdot T_{\mu\nu}^{(2)}, \quad (7)$$

where $x_W = \sin^2\theta_W$ is Weinberg parameter, $T_{\mu\nu}^{(1)}$ and $T_{\mu\nu}^{(2)}$ are tensors of electron-positron and *t*-quark pair determined by the expressions:

$$T_{\mu\nu}^{(1)} = Sp[\upsilon(p_2,s_2)\bar{\upsilon}(p_2,s_2)\gamma_\mu(g_L(e)(1+\gamma_5) + g_R(e)(1-\gamma_5))\times$$

$$\times u(p_1,s_1)\bar{u}(p_1,s_1)\gamma_\nu(g_L(e)(1+\gamma_5) + g_R(e)(1-\gamma_5))] =$$

$$= Sp\left[\frac{1}{2}(\hat{p}_2 - m)(1-\gamma_5\hat{s}_2)\gamma_\mu(g_L(e)(1+\gamma_5)+g_R(e)(1-\gamma_5))\times\right.$$

$$\left.\times\frac{1}{2}(\hat{p}_1 + m)(1-\gamma_5\hat{s}_1)\gamma_\nu(g_L(e)(1+\gamma_5)+g_R(e)(1-\gamma_5)\right] = 2[g_L^2(e)+g_R^2(e)]\times$$

$$\times[p_{2\mu}p_{1\nu}+p_{1\mu}p_{2\nu}-(p_1p_2)g_{\mu\nu}-m^2(s_{2\mu}s_{1\nu}+s_{1\mu}s_{2\nu}-(s_1s_2)g_{\mu\nu})-$$

$$-im\varepsilon_{\mu\nu\rho\sigma}(p_{2\rho}s_{1\sigma}+p_{1\rho}s_{2\sigma})]+2[g_L^2(e)-g_R^2(e)][m(s_{2\mu}p_{1\nu}+p_{1\mu}s_{2\nu}-(p_1s_2)g_{\mu\nu}-$$

$$-p_{2\mu}s_{1\nu}-s_{1\mu}p_{2\nu}+(p_2s_1)g_{\mu\nu})-i\varepsilon_{\mu\nu\rho\sigma}(p_{1\rho}p_{2\sigma}-m^2s_{1\rho}s_{2\sigma})]+4g_L(e)g_R(e)]\times$$

$$\times[-(p_1p_2)(s_{1\mu}s_{2\nu}+s_{2\mu}s_{1\nu}-(s_1s_2)g_{\mu\nu}-(s_1s_2)(p_{2\mu}p_{1\nu}+p_{1\mu}p_{2\nu})+(p_2s_1)(s_{2\mu}p_{1\nu}+$$

$$+p_{1\mu}s_{2\nu}-(s_2p_1)g_{\mu\nu})+(p_1s_2)(s_{1\mu}p_{2\nu}+p_{2\mu}s_{1\nu})-im\varepsilon_{\mu\nu\rho\sigma}(p_{1\rho}s_{1\sigma}+p_{2\rho}s_{2\sigma})],$$

$$T_{\mu\nu}^{(2)} = Sp[u(q_1)\bar{u}(q_1)\gamma_\mu(g_L(t)(1+\gamma_5)+g_R(t)(1-\gamma_5))\times$$

$$\times\upsilon(q_2)\bar{\upsilon}(q_2)\gamma_\nu(g_L(t)(1+\gamma_5)+g_R(t)(1-\gamma_5))]=$$

$$= Sp[(\hat{q}_1+m_t)\gamma_\mu(g_L(t)(1+\gamma_5)+g_R(t)(1-\gamma_5))\times$$

$$\times(\hat{q}_2-m_t)\gamma_\nu(g_L(t)(1+\gamma_5)+g_R(t)(1-\gamma_5)]=$$

$$=8[g_L^2(t)+g_R^2(t)][q_{2\mu}q_{1\nu}+q_{1\mu}q_{2\nu}-(q_1q_2)g_{\mu\nu}]+$$

$$+8i[g_L^2(t)-g_R^2(t)]\varepsilon_{\mu\nu\rho\sigma}q_{1\rho}q_{2\sigma}-16g_L(t)g_R(t)m_t^2g_{\mu\nu}. \quad (9)$$

Here $m$ and $m_t$ are the masses of the electron and $t$-quark.

The product of tensors $T_{\mu\nu}^{(1)}$ and $T_{\mu\nu}^{(2)}$ gives an expression (in the integration over the momenta of the t-quark pair the antisymmetric part of the tensor $T_{\mu\nu}^{(2)}$ vanishes, for this reason this part is not taken into account):

$$T_{\mu\nu}^{(1)}T_{\mu\nu}^{(2)} = 32[g_L^2(e)+g_R^2(e)]\{[g_L^2(t)+g_R^2(t)][(p_1q_1)(p_2q_2)+(p_1q_2)(p_2q_1)-$$

$$-m^2((s_1q_1)(s_2q_2)+(s_1q_2)(s_2q_1))]+2g_L(t)g_R(t)m_t^2[(p_1p_2)-m^2(s_1s_2)]\}+$$

$$+32[g_L^2(e)-g_R^2(e)]m\{[g_L^2(t)+g_R^2(t)][(p_1q_1)(q_2s_2)+(p_1q_2)(q_1s_2)-(p_2q_2)(s_1q_1)-$$

$$-(q_1p_2)(s_1q_2)]-2g_L(t)g_R(t)m_t^2[(p_2s_1)-(p_1s_2)]\}+64g_L(e)g_R(e)[g_L^2(t)+g_R^2(t)]\times$$

$$\times\{-(p_1p_2)[(s_1q_1)(s_2q_2)+(s_1q_2)(s_2q_1)]-(s_1s_2)[(p_1q_1)(p_2q_2)+(p_1q_2)(p_2q_1)-$$

$$-(p_1p_2)(q_1q_2)]+(p_2s_1)[(s_2q_1)(p_1q_2)+(s_2q_2)(p_1q_1)]\}. \quad (10)$$

The integration over the momenta of the t-quark pair is carried out by the invariant method [1, 2, 10].

Integral

$$I_{\mu\nu} = \int q_{1\mu} q_{2\nu} \frac{d\vec{q}_1}{E_1} \frac{d\vec{q}_2}{E_2} \delta(q_1 + q_2 - q) \tag{11}$$

is a second-rank tensor depending only on the 4-dimensional momentum $q = p - k$:

$$I_{\mu\nu} = Aq^2 g_{\mu\nu} + Bq_\mu q_\nu , \tag{12}$$

where $A$ and $B$ are scalar functions. To find them, we multiply expression (11) first by $g_{\mu\nu}$, and then by $q_\mu q_\nu$:

$$\begin{aligned} g_{\mu\nu} I_{\mu\nu} &= (4A + B) q^2, \\ q_\mu q_\nu I_{\mu\nu} &= (A + B) q^4. \end{aligned} \tag{13}$$

Hence we find:

$$A = \frac{1}{3q^2} \left[ g_{\mu\nu} I_{\mu\nu} - \frac{1}{q^2} q_\mu q_\nu I_{\mu\nu} \right]. \tag{14}$$

Let us calculate the integrals

$$g_{\mu\nu} I_{\mu\nu} = \int (q_1 q_2) \frac{d\vec{q}_1}{E_1} \cdot \frac{d\vec{q}_2}{E_2} \delta(q_1 + q_2 - q) = (q_1 q_2) \cdot I = \left( \frac{1}{2} q^2 - m_t^2 \right) \cdot I,$$

$$q_\mu q_\nu I_{\mu\nu} = (q \cdot q_1)(q \cdot q_2) \cdot I = \frac{1}{4} q^4 I.$$

The resulting integral $I$ is easily calculated in the center of mass system of the quark and antiquark

$$I = \int \frac{d\vec{q}_1}{E_1} \frac{d\vec{q}_2}{E_2} \delta(q_1 + q_2 - q) = 2\pi \sqrt{1 - \frac{4m_t^2}{q^2}} . \tag{15}$$

For the scalar function $A$ we obtain the expression:

$$A = \frac{\pi}{6} \left( 1 - \frac{4m_t^2}{q^2} \right)^{\frac{3}{2}} . \tag{16}$$

Similarly, the function $B$ is calculated:

$$B = \frac{1}{q^4} q_\mu q_\nu I_{\mu\nu} - A = \frac{\pi}{3} \sqrt{1 - \frac{4m_t^2}{q^2}} \left( 1 + \frac{2m_t^2}{q^2} \right). \tag{17}$$

When annihilating electron-positron pair is arbitrarily polarized for the angular and energy distributions of the Higgs boson in the reaction $e^- + e^+ \Rightarrow H_{SM} + t + \bar{t}$ is obtained expression:

$$d\sigma = \frac{N_C}{24\pi} \left( \frac{\alpha_{KED}}{x_W (1 - x_W)} \right)^3 M_Z^2 s k_H dE_H d\Omega_H D_Z^2(s) D_Z^2(xs) \times$$

$$\times \sqrt{1 - \frac{4m_t^2}{xs}} \Big\{ [g_L^2(e)(1-\lambda_1)(1+\lambda_2) + g_R^2(e)(1+\lambda_1)(1-\lambda_2)] \cdot \Big[ (g_L^2(t) + g_R^2(t)) \Big( 2\Big( x - \frac{m_t^2}{s} \Big) +$$

$$+\left(1+\frac{2m_t^2}{xs}\right)\frac{k_H^2}{s}\sin^2\theta\Bigg)+12g_L(t)g_R(t)\cdot\frac{m_t^2}{s}\Bigg]+2g_L(e)g_R(e)[(g_L^2(t)+g_R^2(t)]\times$$

$$\times\left(1+\frac{2m_t^2}{xs}\right)\frac{k_H^2}{s}\sin^2\theta\cdot\cos 2\varphi\cdot\eta_1\eta_2\Bigg\}. \quad (19)$$

Here $N_C=3$ is the color factor, $\lambda_1$ and $\lambda_2$ are the helicity of the electron and positron, $\eta_1$ and $\eta_2$ are the transverse components of their spin vectors, $\theta$ and $\varphi$ are the polar and azimuth angles of the Higgs boson.

In the case of a longitudinally polarized electron-positron pair the differential cross section of the process can be represented in the form:

$$\frac{d\sigma(\lambda_1,\lambda_2)}{dxd\Omega_H}=\frac{d\sigma_0}{dxd\Omega_H}\;[(1-\lambda_1\lambda_2)+(\lambda_2-\lambda_1)A_{LR}], \quad (19)$$

where

$$\frac{d\sigma_0}{dxd\Omega_H}=\frac{N_C}{48\pi}\left(\frac{\alpha_{KED}}{x_W(1-x_W)}\right)^3 M_Z^2 s\sqrt{s}k_H D_Z^2(s)D_Z^2(xs)\times$$

$$\times\sqrt{1-\frac{4m_t^2}{xs}}[g_L^2(e)+g_R^2(e)]\cdot\Bigg\{(g_L^2(t)+g_R^2(t))\Bigg[2\left(x-\frac{m_t^2}{s}\right)+$$

$$+\left(1+\frac{2m_t^2}{xs}\right)\frac{k_H^2}{s}\sin^2\theta\Bigg]+12g_L(t)g_R(t)\cdot\frac{m_t^2}{s}\Bigg\} \quad (20)$$

is differential cross section of the process in the case of unpolarized particles and

$$A_{LR}=\frac{g_L^2(e)-g_R^2(e)}{g_L^2(e)+g_R^2(e)}=\frac{\frac{1}{4}-x_W}{\frac{1}{4}-x_W+2x_W^2}. \quad (21)$$

is left-right spin asymmetry due to longitudinal polarization of the electron. This asymmetry depends only on the Weinberg parameter $x_W$ and at a value of this parameter $x_W=0.232$ it is equal to $A_{LR}=14\%$ .

When the electron-positron pair is polarized transversally the cross section is:

$$\frac{d\sigma(\eta_1,\eta_2)}{dxd\Omega_H}=\frac{d\sigma_0}{dxd\Omega_H}\;[1+A(\theta,\varphi)\cdot\eta_1\eta_2], \quad (22)$$

where

$$A(\theta,\varphi)=\frac{2g_L(e)g_R(e)}{g_L^2(e)+g_R^2(e)}\cdot\frac{\left(1+\frac{2m_t^2}{xs}\right)\frac{k_H^2}{s}\sin^2\theta\cdot\cos 2\varphi}{2\left(x-\frac{m_t^2}{s}\right)+\left(1+\frac{2m_t^2}{xs}\right)\frac{k_H^2}{s}\sin^2\theta+\frac{12g_L(t)g_R(t)}{g_L^2(t)+g_R^2(t)}\cdot\frac{m_t^2}{s}} \quad (23)$$

is azimuthal angular asymmetry (this asymmetry is also called transverse spin asymmetry, since it is connected by transverse polarizations of the electron and the positron).

Fig. 2 shows the angular dependence of the transverse spin asymmetry $A(\theta,\varphi=0)$ at $\sqrt{s}=1000$ *GeV*,

$E_H$ =440 $GeV$, $M_H = 125$ $GeV$ and $x_W = 0{,}232$ (everywhere taken $\sin^2\theta_W = x_W = 0{,}232$).

As can be seen the transverse spin asymmetry is negative, the asymmetry at zero angle of the Higgs boson emission is zero, with an increase in the angle $\theta$ the asymmetry decreases and reaches a minimum at an angle of $\theta = 90°$ and then the asymmetry again increases and reaches a zero at the end of the angular spectrum.

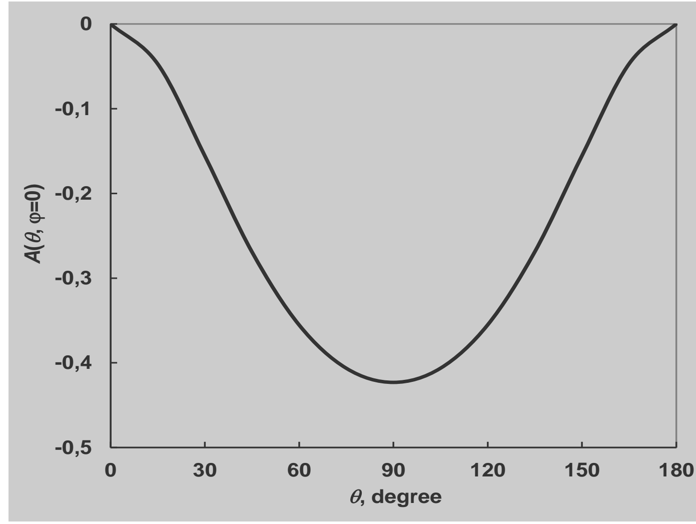


*Fig. 2.* The angular dependence of the transverse spin asymmetry in the process $e^-e^+ \to H_{SM}t\bar{t}$ .

The transverse spin asymmetry integrated over the polar angle $\theta$ is expressed by the formula

$$A(\varphi) = \frac{2g_L(e)g_R(e)}{g_L^2(e)+g_R^2(e)} \cdot \frac{\left(1+\frac{2m_t^2}{xs}\right)\frac{k_H^2}{3s}\cdot\cos 2\varphi}{x-\frac{m_t^2}{s}+\left(1+\frac{2m_t^2}{xs}\right)\frac{k_H^2}{3s}+\frac{6g_L(t)g_R(t)}{g_L^2(t)+g_R^2(t)}\cdot\frac{m_t^2}{s}}. \tag{24}$$

Fig. 3 illustrates the dependence of the transverse spin asymmetry $A(\varphi = 0)$ on the energy of the scalar Higgs boson at $\sqrt{s} = 1000$ $GeV$ and $M_H = 125$ $GeV$.

At a minimum Higgs bosons energy of the $E_H = M_H = 125$ $GeV$, the transverse spin asymmetry is zero, from Fig. 3 it follows that the asymmetry is negative and decreases with increasing boson energy, and at the end of the enegy spectrum reaches the value $A(\varphi = 0) = -0{,}79$.

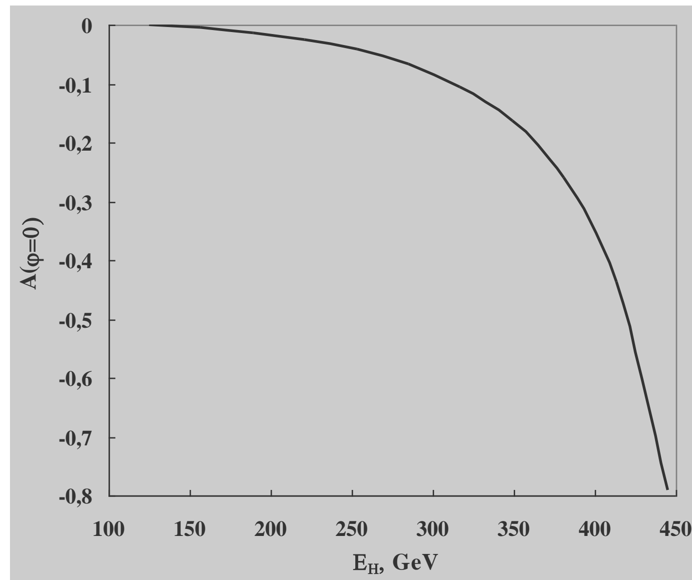


*Fig. 3.* The energy dependence of the transverse spin asymmetry in the reaction $e^-e^+ \to H_{SM}t\bar{t}$ .

Integrating the cross section (20) over the angles of the emission of the Higgs boson, in the case of unpolarized particles we find the following expression for the distribution of $t\bar{t}$ -quark pairs with respect to the invariant mass:

$$\frac{d\sigma_0}{dx}=\frac{N_C}{6}\left(\frac{\alpha_{KED}}{x_W(1-x_W)}\right)^3 M_Z^2 s\sqrt{s}k_H D_Z^2(s)D_Z^2(xs)\sqrt{1-\frac{4m_t^2}{xs}}[g_L^2(e)+g_R^2(e)]\times$$

$$\times\left\{(g_L^2(t)+g_R^2(t))\left[x-\frac{m_t^2}{s}+\left(1+\frac{2m_t^2}{xs}\right)\frac{k_H^2}{3s}\right]+6g_L(t)g_R(t)\cdot\frac{m_t^2}{s}\right\}. \quad (25)$$

Fig. 4 shows the dependence of the cross section of the process $e^- + e^+ \to H_{SM} + t + \bar{t}$ on the invariant mass of *x* at an energy of $e^-e^+$-beams $\sqrt{s}=1000$ GeV and a mass of $M_H = 125$ GeV. According to this figure, with an increase in the invariant mass the cross section decreases monotonically from 2.6 fb to 0.07 fb.

As for the differential cross sections for the processes $e^- + e^+ \to H + t + \bar{t}$ and $e^- + e^+ \to h + t + \bar{t}$, we note that, according to the MSSM, the vertex of the interaction ZZH (ZZh) contains a constant $g_{ZZH}(g_{ZZh})$, where $g_{ZZH}=\frac{eM_Z}{\sin\theta_W\cdot\cos\theta_W}\cdot\cos(\beta-\alpha)$ $\left(g_{ZZh}=\frac{eM_Z}{\sin\theta_W\cdot\cos\theta_W}\cdot\sin(\beta-\alpha)\right)$, where $\beta$ and $\alpha$ are some parameters of the MSSM [16]. Consequently, the differential cross sections of the processes $e^- + e^+ \to H + t + \bar{t}$ and $e^- + e^+ \to h + t + \bar{t}$ will differ from the cross section of the reaction $e^- + e^+ \to H_{SM} + t + \bar{t}$ by the presence of an additional factor $\cos^2(\beta-\alpha)$ and $\sin^2(\beta-\alpha)$.

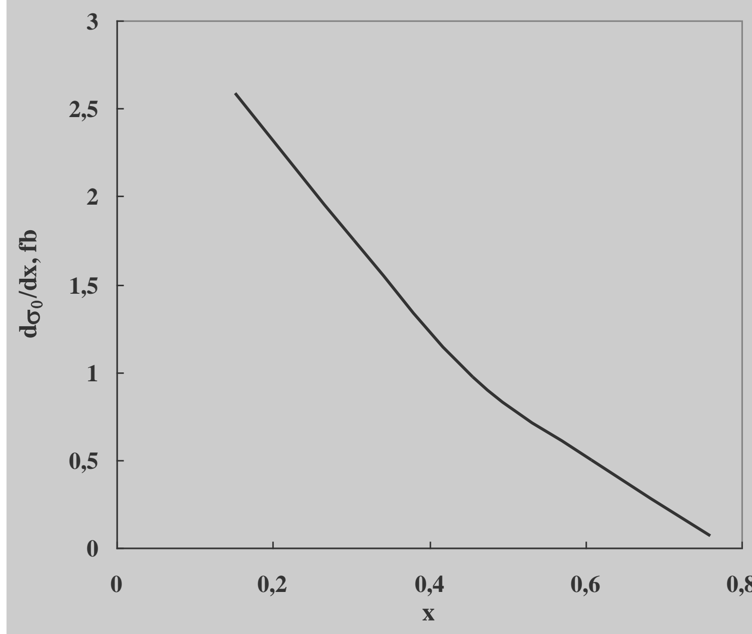


*Fig. 4.* Dependence of the cross section for the process $e^-e^+ \to H_{SM}t\bar{t}$ on the invariant mass x

We note that in the process $e^- + e^+ \to H_{SM} + t + \bar{t}$ along with the Feynman diagram, shown in Fig. 1, there are other diagrams where the Higgs boson $H_{SM}$ radiation comes from the $t$-quark or $\bar{t}$-antiquark line (see Fig. 5). However, the calculation of these diagrams will be given in a separate article.

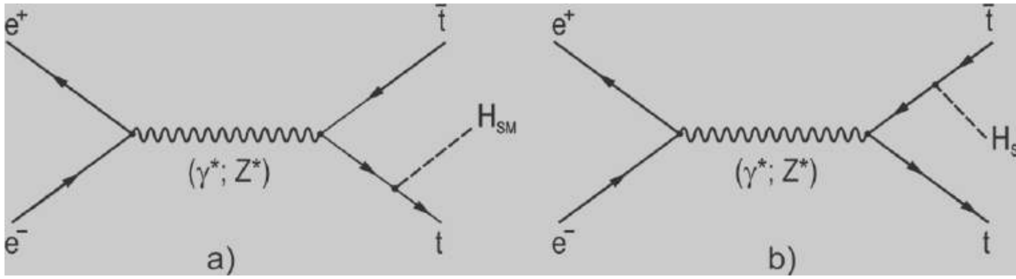


*Fig. 5.* The Feynman diagrams of the reaction $e^- + e^+ \to H_{SM} + t + \bar{t}$

## 3. CONCLUSION

Thus, we discussed the processes of the production of a Higgs boson $H_{SM}(H;h)$ and a $t$-quark pair in the annihilation of an arbitrarily polarized electron-positron pair:

$$e^- + e^+ \to H_{SM} + t + \bar{t},\ e^- + e^+ \to H + t + \bar{t},\ e^- + e^+ \to h + t + \bar{t}.$$

Analytic expressions are obtained for differential cross sections, left-right and transverse spin asymmetries. The dependences of the polarization characteristics and cross sections on the emission angle and the energies of the scalar boson, on the invariant mass the $t$-quark pair, are investigated. The results are presented in the form of graphs.

[1] *S.Q. Abdullayev.* Lepton-lepton və lepton-hadron qarşılıqlı təsirlərində zəif cərəyan effektləri (I hissə), Bakı, «AM 965 MMC», 2012, səh 484.

[2] *S.Q. Abdullayev.* Standart model, lepton və kvarkların xassələri. Bakı, «Zəka-Print», 2017, səh. 284.

[3] *A. Djouadi.* The Anatomy of Electro-Weak Symmetry Breaking. Tome I: The Higgs bosons in the Standart Model. arXiv: hep-ph/0503173v2,3 may, 2005.

[4] ATLAS Collaboration. Observation of a new particle in the search for the Standard Model Higgs boson with the ATLAS detector at the LHC Phys. Letters, 2012, B176, p. 1-29.

[5] CMS Collaboration. Observation of a new boson at mass of 125 *GeV* with the CMS experiment at the LHC Phys. Letters, 2012, B716, p.30-60.

[6] *V.A. Rubakov.* Uspexi fizicheskix nauk, 2012, t.182, №10, s.1017-1025 (*İn Russian*).

[7] *A.V. Lanev.* Uspexi fizicheskix nauk, 2014, t.184, №9, c.996-1004 (*İn Russian*).

[8] D.İ. Kazakov. Uspexi fizicheskix nauk, 2014, t.184, № 9, c. 1004-1017 (*İn Russian*).

[9] *S.K. Abdullayev, M.Sh. Gojayev, F.A. Saddigh.* Decay Channels of the Standart Higgs Boson, Moscow University Phusics Bulletin, 2017, Vol.72, №4, pp.329-339; published in Vestnik Moscovskoqo Universiteta, Seriya 3: Physics, Astronomy, 2017, №4, s.3-11.

[10] *S.K. Abdullayev, L.A. Agamaliyeva, M.Sh. Qocayev, F.A. Saddigh.* İssledovaniye rojdeniya higgsovskix bozonov v lepton-antileptonnıx stolknoveniyax. GEST: Physics, 2015, №1(13), pp.36-55. (İn Russian).

[11] *S.K. Abdullayev, L.A. Agamaliyeva, M.Sh. Qocayev, F.A. Saddigh.* Hiqqs bozon Decay Channels $H \Rightarrow \gamma\gamma, H \Rightarrow \gamma Z, H \Rightarrow gg$ Azerbaijan. Journal of Physics Fizika, 2015, №2, pp.17-22.

[12] *S.K. Abdullayev, L.A. Agamaliyeva, M.Sh. Gojayev.* İssledovaniye rojdeniya higgsovskoqo bozona v qlubokoneupruqom lepton-nuklonnom rasseyanii. GESJ: Physics, 2015, №2(14), pp.28-40 (İn Russian)

[13] S.K. Abdullayev, M.Sh. Gojayev, Saddigh F.A. Hiqqs bozon production in lepton collisions Azerbaijan Journal of Physics, Fizika, 2015, №3, pp.21-29.

[14] *Abdullayev S.K., Gojayev M.Sh., F.A. Saddigh.* Hiqqs bozon production in electron-positron scattering Azerbaijan Journal of Physics, Fizika, 2014, №3, pp.31-41.

[15] *S.K. Abdullayev, M.Sh. Gojayev.* Production and decay of Hiqqs bozons in muon colliders International conference «Modern trends in Physics», Baku, 2017, 20-22 April.

[16] *A. Djouadi.* The Anatomy of Electro-Weak Symmetry Breaking, tome II: The Higgs bosons in the Minimal Supersymmetric Model: arXiv: hep-ph/0503173v2, 2003.

*Received:29.12.2017*

# THE FORMATION OF NANO-DEFECT STRUCTURES IN PROCESS OF DOUBLE CROSS SLIP

**(This article is devoted to memory of M.B.Abdullayev)**

**A.Sh. KAKHRAMANOV[1], N.M. ABDULLAYEV[2], K.Sh. KAKHRAMANOV[2]**

*[1]Baku State University*
*Z.Khalilov str., 23, Baku Azerbaijan*
*[2]Institute of Physics of Azerbaijan NAS,*
*H.Javid ave., 33, Baku, Azerbaijan*
*E-mail:nadirabdulla@mail.ru*

It is shown that volume defects and slip bands form because of double cross slip (DCS). At small voltages the plastic deformation takes place in shift band area an it stays constant behind the wave area. On the base of crystal AFM-images it is shown that the formation of nano-islands (NI) can be considered on the base of conception of double cross slip. The possibility of synergetic approach for the analysis of concrete phenomena developing in dislocation ensemble in the forms of slip lines and slip bands, is demonstrated.

**Keywords:** plasticity, annihilation, dislocation, localization, deformation.
**PACS:** 68.37, 68.35.bg, 68.35.Dv, 68.35.Ja, 68.37.Ps

## INTRODUCTION

The defect formation process on the base of the conception of double cross slip (DCS) are considered in work.

The plastic deformation in crystals begins at achieving of critical value by shear stress. Moreover the dislocation loops begin to move in slip plane and expand, in the result of which the shift bands appear [1]. At deformation increase the shift bands can join to packs forming the slip bands in macrolevel [2]. The slip bands play the important role in process of plastic deformation and they are intensively studied theoretically and experimentally. The expansion of shift band takes place as a result of *(DCS)* screw dislocation regions [3-7].

The crystal deformation takes place only in front of shift band. The velocity behind the band front strives to zero in the result of the internal stresses on accumulation of their dislocation, that's why the plastic deformation inside the band stays constant. The math models describing the expansion the shift bands in the result of *DCS* action are constructed in [4-6]. However, the approach realization suggested in [4-6] have disadvantages; the assumption on constancy of dislocation rate of motion contradicts to experiment data on dislocation deceleration inside shift band [3]. The math model of shift band distribution is constructed in [1]; the solutions describing the shift band structure considered in [3] are obtained. The scheme of slip band development in plane sample at uniaxial extension along $x_1$ axis (dislocation motion is along $x$ axis, the expansion of slip bands is along y axis) is given in [1]. Using the given scheme the plane sample which is extended along $x_1$ axis under $\sigma_1$ voltage action, is considered. The dislocation motion takes place in slip plane inclinated to $x_1$ axis on $\psi$ angle. The plastic deformation takes place because of motion of dislocation loops up to the moment of their deceleration on obstructions of different nature (impurities and extractions). The screw region of dislocation loop can be put into neighbor slip plane under the influence of local voltages. The dislocation loop in initial slip plane rounds the obstruction and continues its motion. The time and distance of the screw segement surge has the occasional character, that's why the process of dislocation multiplication is described by kinetic balance equation [4]. Note that if the surge distance is $h < h_o$ then this segment doesn't move because of elastic interaction of surged segment with dislocation in initial plane and two edge dipoles appear in the result of surge [3]. In $h > h_o$ case the expansion of dislocation segment the motion of which leads to new *DCS* acts takes place in neighbor plane. The critical distance of segment surge is defined by formula given in [3]:

$$h_0 = \mu b/(8\pi(1-\nu)(\sigma-\sigma_f)),$$

where μ is shear modulus; $\nu$ is Poisson ratio; b is strength of dislocation; σ is voltage tangent lines; $\sigma_f$ is dry friction voltage.

In case when dislocation motion has thermoactivated character then dislocation rate of motion in slip plane is approximated b the following formula [3,7]:

$$u = u_0\left(\frac{\sigma-\sigma_f-\sigma_\mu}{\sigma_0}\right)^m \qquad \sigma_\mu = \alpha\mu b\sqrt{\rho},$$

where $\alpha$, $u_0$, $\alpha_o$ are empirical constants; m = $H_o/(kT)$; $H_o$ is character activation energy*;* $k$ is Boltzman constant; T is temperature; $\alpha_\mu$ is voltage caused by interaction of given dislocation with nearest surrounding.

The plastic deformation begins from $\sigma > \sigma_*$ equation carrying out where $\sigma_* = \sigma_f + \sigma\mu$ is shift critical voltage. The dislocation velocity υ in direction perpendicukar to slip plane is defined by diffusion of point defects.

The deformation linearly increases at shift from wave front to band center. This solution can be interpreted as deformation localization taking place because of voltage increase in region of shift band development.

Our aim is the consideration of NI mechanism, their coalescence and coagulation on the base of DCS conception.

131 H.Javid ave, AZ-1143, Baku
ANAS, G.M.Abdullayev Institute of Physics
E-mail: jophphysics@gmail.com

## EXPERIMENT AND DISCUSSION

The samples are obtained by the method of directed crystallization at hot zone temperature 900K. The plates with surface orientation *(0001)* are cut from the samples. The mechanical treatment isn't carried out.

The electron-microscopic images are obtained on atomic-force microscope (AFM) of *SOLVER NEXT* mark.

NI of (0001) $A_2^V B_3^{VI}$ semiconductor surface and processes of heir localization taking place in the result of DCS are considered.

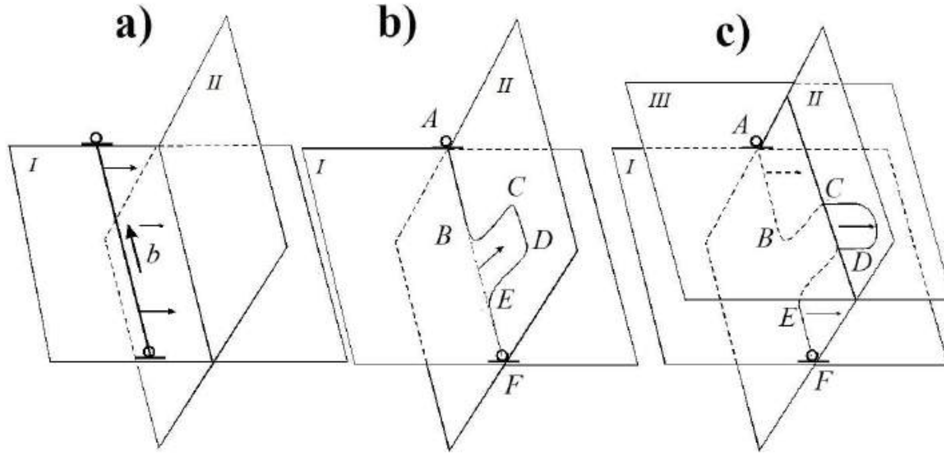


*Fig. 1. DCS* scheme.

*Fig.2. AFM*-images *$Bi_2Te_3$<Se>, NI* are ordered formed nano-islands on the places of dislocations on surface (0001).

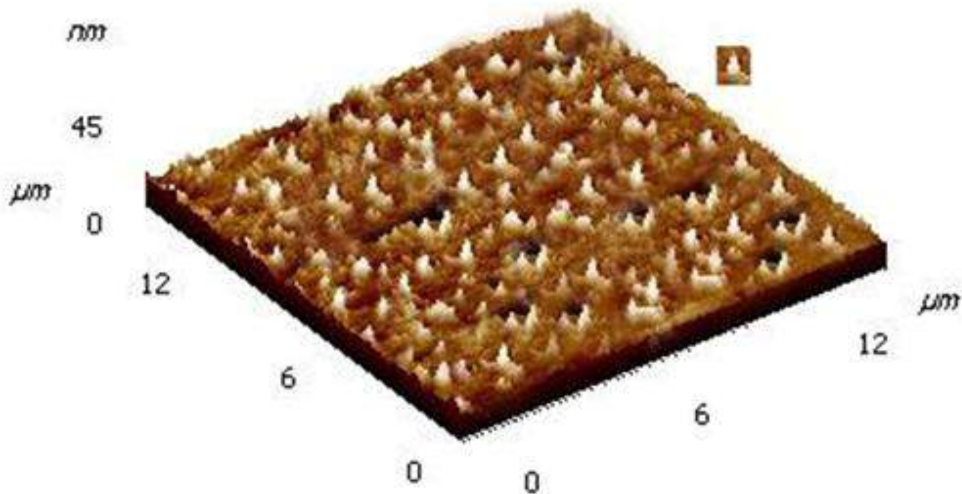


*Fig.3. AFM*-images in 3D-scale on surface *$Bi_2Te_3$ <Ni>*. Here the "smeared" nano-islands (NI) round, which the nano-islands (NI) of small sizes presenting the places of cross slip take place, are seen.

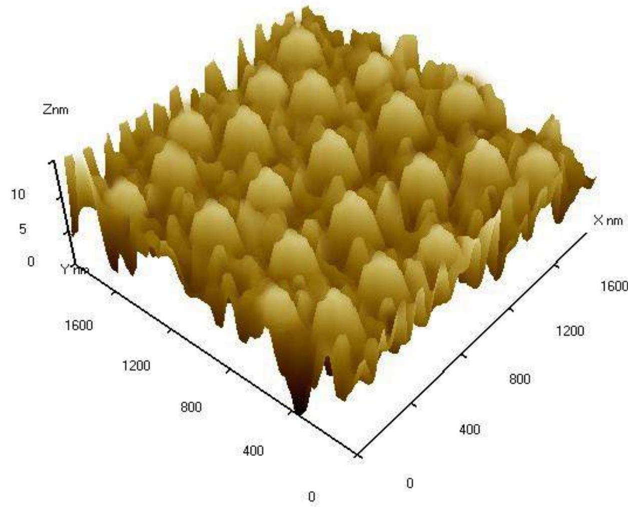


*Fig.4. AFM*-images by height 10nm of big and small NI on surface $Bi_2Se_3$. The aligning arrangement of such NI can be evidence of their redistribution in process of cross slip of screw dislocation.

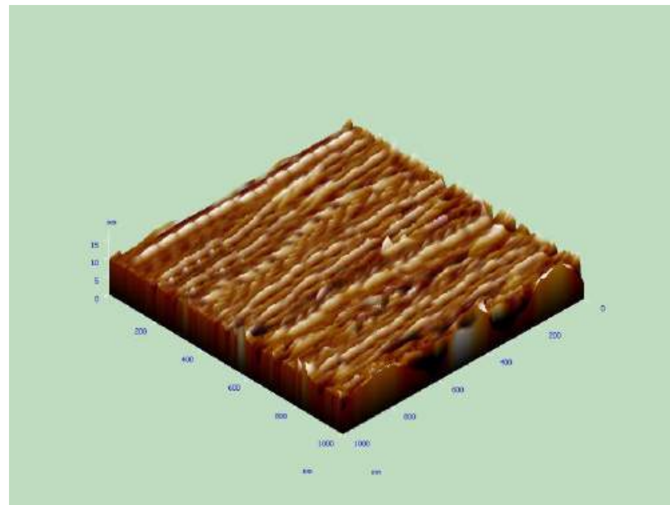

*Fig.5.* Line defects in solid solution $Bi_2Te_3$ *90mole%*- $Bi_2Se_3$ presenting the localized slip lines in layered semiconductors of $A^V{}_2B^{VI}{}_3$ type.

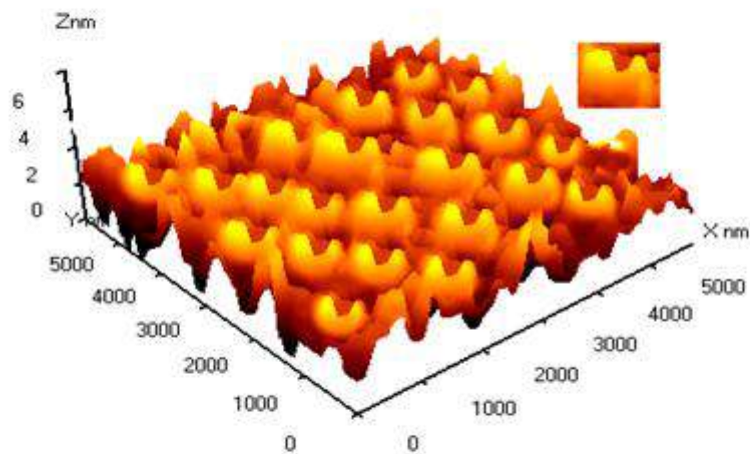


*Fig.6.* Double *AFM*-images $Bi_2Te_3$ *<Ni>* characterising *DCS* mechanism. The double nano-islands with the saddle characterising the transition of slip lines is emphasized in right in insertion.

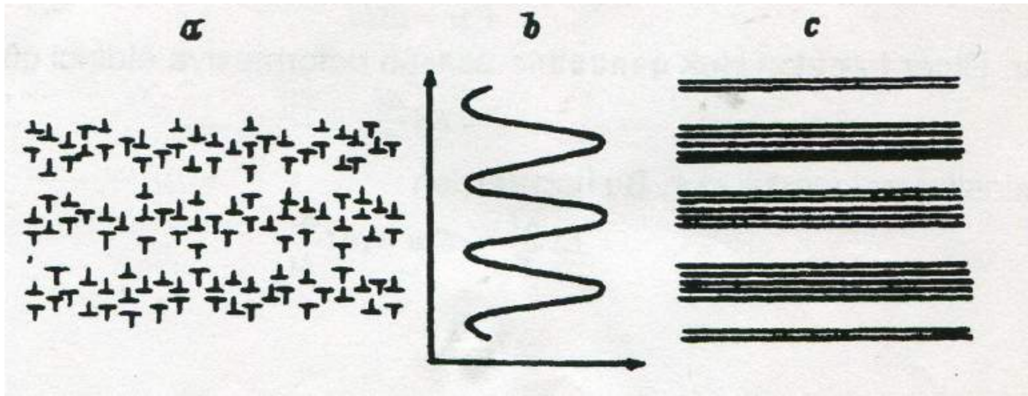


*Fig.7.* Microscopic (a) and mezoscopic (c) levels of self-organization>dislocation in slip lines. Such lines are experimentally revealed and presented in fig.5. This circumstance is revealed in the form of thin and more rude slip lines visible in optic microscope on crystal surface. The heterogeneity of deformation redistribution in crystal is the result of space-heterogeneous distribution (in the fiven case layered one) of mobile dislocation density in it.

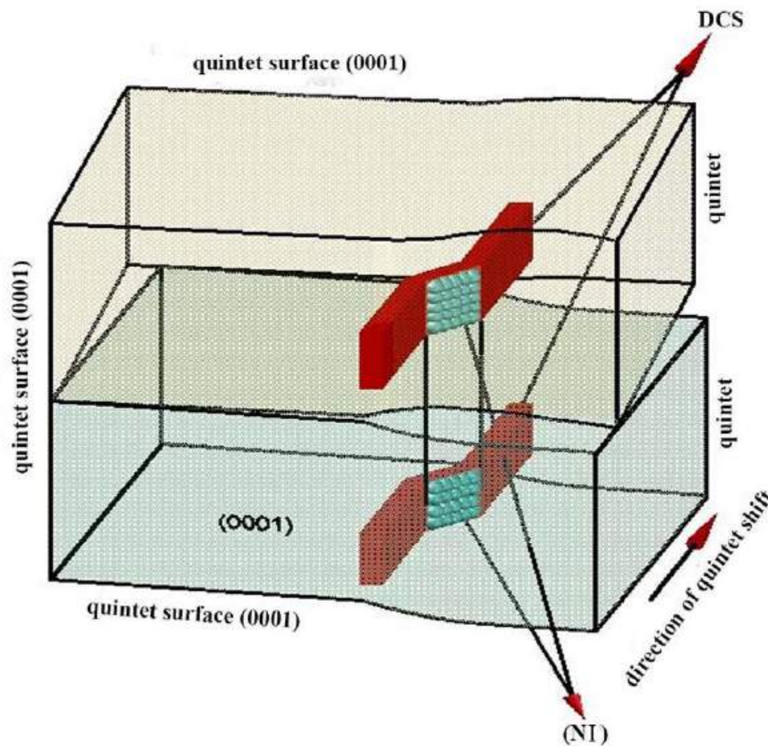


*Fig.8. DCS* scheme with screw dislocation between two quintets $A_2^VB_3^{VI}$.

## CROSS SLIP IN $Bi_2Te_3$

The multiplication of dislocations and the precipitation of impurities in dislocation pits can be considered in limits of cross slip of screw dislocations. Note that the screw dislocations (SD) in $Bi_2Te_3$ and $Sb_2Te_3$ compounds have the ability to cross slip.

Let's consider the slip circuit including *DTS* in which screw dislocations *AF* (see fig.1a) have the main (I) and additional (II) plane of cross slip.

If the obstruction in the form of impurity or defect appears in plane of primary slip in *CE* direction (see fig.1b) then *AF* dislocation can change the direction and conntinues the slip by plane *II* showing *BCDE* double kink in this plane.

Such transition of dislocation part from one plane to another one for $Bi_2Te_3$ can be cross slip. (0001) is the main plane of slip in layered crystals of $Bi_2Te_3$ type. The plane perpendicular to (0001) $Bi_2Te_3$ one (fig.1b) should be the plane (*II*) of cross slip; it presents itself *BCDE* kink; the motion directions in all planes are shown by arrows.

The first kink *BCDE* moving in *II* plane can carry out the cross slip moving to *III* plane parallel to main plane (fig.1.c).

Such two consistent acts of cross slip can form as *DTS*. The localized *NI* are their example (see fig.2-5). Burger vector change in II plane for bismuth telluride is

shown by arrorw (see *DTS* circuit, fig.1). Moreover, the dislocation changed the slip plane for the second time transits into parallel surface level or on surface of nearest quintet of crystal lattice.

In principle, the multiple cross slip when dislocation changes the quintet planes many times with more profitable thermodynamic conditions of slip and formation of *(NI)* nano-islands on dislocations, is possible.

The nano-islands settled in places of *ABCDE* paired kink are shown in fig.2-6.

Such paired kinks can be in interplanar space in planes of cross slip.

Earlier such places of accumulations in (0001) $Bi^{V}_{2}Te^{VI}_{3}$ plane form the different volume defects [8,9]. *NI* and their accumulations are especially interest ones, AFM-images of such structures are presented in fig.3-6.

The wide diversity of forms and sizes including the linear defects (see fig.5) are seen in fig.5-6.

If one can consider *NI* as settling impurities on dislocation surface (0001) $Bi_2Te_3$ then cross slip area can be considered as places of formation of different nano-islands.

Moreover, one can consider *DCS* character on interlaminar surface (0001) $Bi^{V}_{2}Te^{VI}_{3}$ by density and line dislocation.

The scheme of short-wave thin slip lines is given in fig.7. This demonstrates the corresponding layered distribution of dislocations on microscopic level.

The existing of several scale levels of slip localization is the character feature of plastic deformation.

## SLIP BANDS

The appearance and widening of slip bands in crystals is the another character element of initial degree of crystal deformation. The kink bands causing the lattice disorientation between neighbor crystal volumes are the special case of deformation localization on its initial degree. The theoretical analysis of formation mechanism of both type bands is based on nonlinear equations of dislocation local density evolution. The solution examples of these equations in the form of stationary moving fronts are in [3] (in case of slip bands), in [6] (in case of kink bands), in [7] (in case of Luders bands in polycrystals).

The another difference of present approach to the problem is in the fact that formation of slip of lines and bands can be considered in the limits of one system of initial dislocation equations using the slip lines.

The density of dislocation sources also defines the conditions of appearance and stable expansion of slip bands. For band appearance it is necessary that dislocation source density is less than some critical value.

The interaction of such system open to each other and external influence leads to formation of essentially nonequilibrium space and time structures with thermodynamic point of view.

The formation mechanism scheme of other heterogeneous dislocation structures in more late deformation stages from the given positions is given in fig.8.

## CONCLUSION

The math development model of plastic deformation because of action of DCS mechanism and also the solution of running wave type and its structure are analysed. The stability of single crystal heterogeneous state has been investigated. It is seen that if the disturbance is in instable region then its growth takes place after that two shift bands each of which is described by solution of running wave type propagate in opposite directions.


[1] *S.P. Kiselev.* Prikladnaya mexanika I texnicheskaya fizika. 2006. T. 47, № 6, s. 202-113. (In Russian).

[2] *A. Chiqenbayn, Y. Plessinq, Y. Noyxayzer.* Fiz. mezomexanika. 1998. T. 1, № 2. s. 5-20. (In Russian).

[3] *B.M. Smirnov.* Dislokachionnaya struktura I uprochnenie kristallov. L.: Nauka. Leninqr. otd-nie, 1981, s 323. (In Russian).

[4] *G.A. Maliqin.* Uspexi fiz. nauk. 1999. T. 169, № 9. s. 979-1010. (In Russian).

[5] *P. Hahner.* Theory of solitary plastic waves. 1. Luders bands in polycrystals. Appl. Phys. A.1994. V. 58. P. 41-48.

[6] *P. Hahner.* Theory of solitary plastic waves. 2. Luders bands in single glide-oriented crystals. Appl. Phys. A. 1994. V. 58. P. 49-58.

[7] *S.P. Kiselev.* Vnutrennie napyajeniya v tverdom tele s dislokachiyami PMTF. 2004. T. 45, № 4. s. 131-136. (In Russian).

[8] *F. K. Aleskerov, S.Sh. Kaxramanov, K.Sh. Kaxramanov, E.M. Derun, M.G. Pishkin.* J. Fizika. tom XII, № 4, 2006, s. 33-40. (In Russian).

[9] *A.P. Alieva, S.Sh. Kaxramanov, F.K. Aleskerov, S.A. Nabieva, K.Sh. Kaxramanov.* J. MNPK «Sovremennie informachionnie I elektronnie texnoloqii».2015, s. 287-288. (In Russian).


*Received:06.02.2018*

# TEMPERATURE DEPENDENCE OF PHOTOLUMINESCENCE OF $ZnGa_2S_4$

**T.G. KERIMOVA, I.A. MAMEDOVA, I.G. NASIBOV, S.G. ASADULLAEVA, Z. KADIROGLU**
*Institute of Physics named by G.M. Abdullaev of NAS of Azerbaijan*
*taira-kerimova@mail.ru, irada_mamedova@yahoo.com*

Influence of temperature on the photoluminescence of $ZnGa_2S_4$ in the temperature range 10-300K has been investigated. Activation energy of temperature quenching of two observed energy bands at 440 and 540 nm was determined. The scheme of radiation transitions is constructed.

**Keywords:** Antistructural defects, photoluminescence, activation energy, $ZnGa_2S_4$
**PACS:** 71.35.Cc

## INTRODUCTION

$ZnGa_2S_4$ belong to $A^2B_2^3C_4^6$ type semiconductors, crystallizing in the space gr. $S_4^2$. Their unique properties as birefringence, optical activity, high values of the nonlinear susceptibility coefficient, intensive luminescence make them perspective materials in using as semiconducting and nonlinear transformers [1,2], in particular, due to the large width of the band gap and high photosensitivity, ultraviolet radiation detectors were created used in medicine, biology, space physics and other fields were created on their basis.

Wide band gap compounds are of special interest in using as sources and detectors in short-wave region of the spectrum (blue, green and near ultraviolet). In this connection, the study of the radiative properties of these compounds is an actual task. ZnGa2S4 with an ordered cation vacancy crystallizes in a tetragonal structure and has a band gap of 3.2 eV [3,4]. In [5] the band structure of $ZnGa_2S_4$ was calculated by the pseudopotential method. The calculated width of the band gap is equal to 3.6 eV. The first studies of the luminescent properties of $ZnGa_2S_4$ single crystals were carried out in [6]. The radiative properties of $ZnGa_2S_4$ were also investigated by us in [7]. In the PL spectrum, maxima were observed at 460, 530, 640 nm. A wide photoconductivity band of $ZnGa_2S_4$ with a maximum at 3.18 eV at 300 K was observed in [8].

In the present work, the effect of temperature on photoluminescence in $ZnGa_2S_4$ in the temperature range 10-300 K was investigated. Since the crystal structure refers to defective chalcopyrites, the cationic ordered vacancy and the cation-induced substitution in the cation sublattice [9], create the deep levels in the band gap. As it is known, deep levels strongly influence on the radiative properties and therefore, for applied purposes, information on deep levels is important.

## SYNTHESIS AND EXPERIMENTS

Samples for measurements were synthesized from the initial components of Zn, Ga and S were taken in the stoichiometric ratio in graphitized quartz ampoules. X-ray diffraction measurements were carried out on a Bruker D8 device. The lattice parameters a = b = 5.2870 Å, c = 10.428 Å with / a = 1.972. ZnGa2S4 crystallizes in the tetragonal structure (sp. gr. $S_4^2$). The lattice parameters are in good agreement with the results of the authors [4, 10, 11]. For photoluminescence measurements the excitation source with the wavelength of 325 nm was used.

## DISCUSSION OF RESULTS

On fig. 1 photoluminescence spectra of $ZnGa_2S_4$ at 300, 202, 110, 74 K in the range 350÷650 nm are presented. As it is shown, at 300 K in a spectrum two wide bands are observed: at 2,82 eV (440 nm), more intensive band which covers spectral range approximately from 450 nm to 640 nm, with a maximum 2,29 eV (540 nm) and a weak shoulder at 3,31 eV (375 nm). As value of band gap width of $ZnGa_2S_4$ is equal 3,18 eV [3], 3,22 eV [4] the observed shoulder (375 nm), can be connected with interband transition, which with temperature decreasing disappears. Intensity of bands with maxima of 440 and 540 nm increase with the decrease of temperature up to 74 K, and further, up to 10 K remain almost invariable.

Temperature dependences of the photoluminescence intensity lgI=f ($10^3$/T) for both of radiation bands are presented in fig. 2. As it is shown from fig. 2, the slow temperature quenching of luminescence occurs in temperature interval 74 K to 135 K, while above 150 K it relatively increases. In temperature dependence lgI=f ($10^3$/T) the linear part of high-temperature range over 150 K is described by a following equation [12]:

$$I=K\exp(\Delta E/kT) \qquad (1)$$

where $I$ is the PL intensity, $K$ is a constant, $\Delta E$ is activation energy. Value of the activation energies $\Delta E$ for the given temperature quenching process for emission bands with a maximum of 440 nm and 540 nm are determined as 28 meV and 23 meV, accordingly. Due to near positions of these bands, in all investigated temperature region, it was not possible clearing up their splitting and determination of change of halfwidth with temperature. It was not easy to distinguish the shifting of the bands with varying temperature because of their superposition. In the given crystal authors [6] investigated temperature dependence of emission band (1,8 эВ (660 nm)) at 80-300 K. Activation energy for this band is determined as 110 meV.

131 H.Javid ave, AZ-1143, Baku
ANAS, G.M.Abdullayev Institute of Physics
E-mail: jophphysics@gmail.com

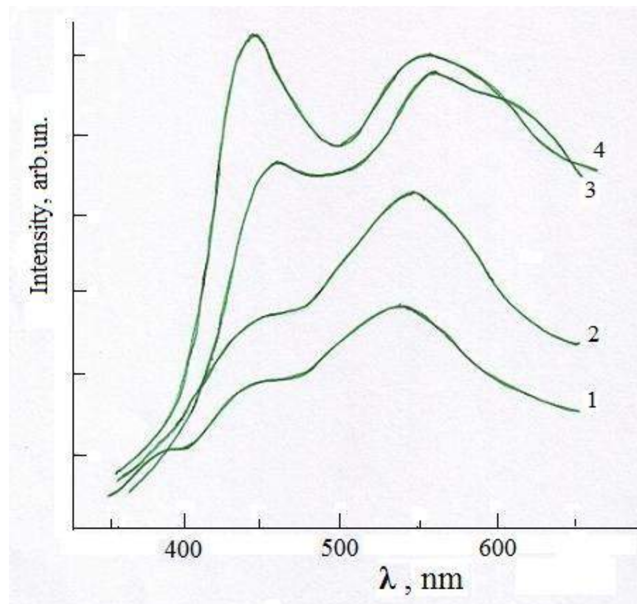


*Fig. 1* Photoluminescence spectra of $ZnGa_2S_4$ at *1*- 300, *2*- 202, *3*- 110, *4*- 74 K

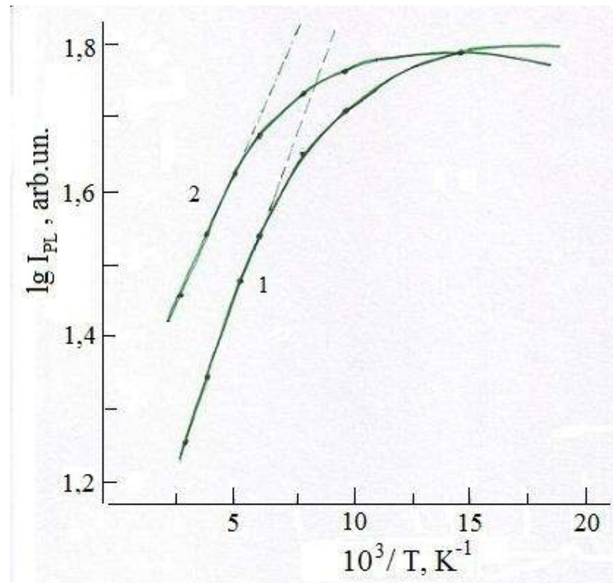


*Fig. 2.* Temperature quenching of photoluminescence intensity of $ZnGa_2S_4$ for emission bands *1*– 440 nm, *2*- 540 nm

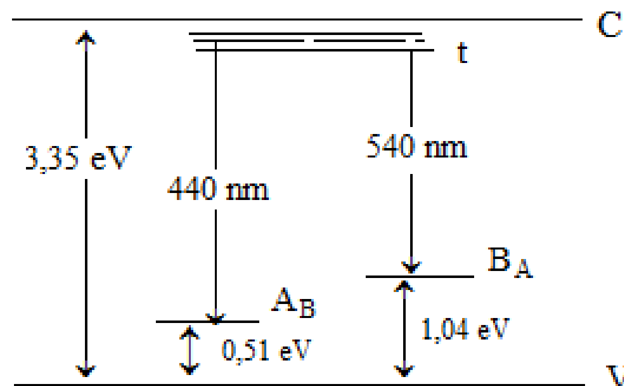


*Fig. 3.* Scheme of local states and electron transitions in $ZnGa_2S_4$

On the base of results of the given experiment, one can construct the scheme of radiation transitions in the band gap (fig. 3). As it is known, the given crystals are characterized by the high probability of disorder in cation sublattice which causes presence in ternary semiconductors quasi-continuously and exponentially distributed states below a bottom of the conduction band [1].

As shown from fig. 3, the emission band at 440 nm is connected with transition from quasi-continuously distributed traps to the state, which is above the valence band top for 0,51 eV, and emission band with maximum at 540 nm is connected with the transition from traps to the deep states localized on 1,04 eV above the top of valence band.

## CONCLUSION

In the given work temperature influence (10-300K) on PL of $ZnGa_2S_4$ is investigated. In spectra emission bands are found at 440 and 540 nm. The scheme of radiative transitions is constructed. It is established, that these bands are connected with radiative transitions from the quasi-continuously distributed states located below the bottom of conduction band to 28 and 23 meV to the deep states located above the valence band top as 0,51 eV and 1,04 eV, accordingly.

---


[1] *A.N. Georqobiani, S.I. Radauchan, I.M. Tiqinyanu.* Wide-Gap II-$III_2$-$VI_4$ semiconductors: optical and photoelectric properties and potential applications, FTP, 19 (1985) 193-212.

[2] *I.S. Yahia, M. Fadel, G.B. Sakr, F. Yakub Hanoglu, S.S. Shenouda and W.A. Faroog.* Analysis of current-voltage characteristics of Al/p- $ZnGa_2Se_4$/-n-Si nanocrystalline heterojunction diode, J. Alloys Compounds 509 (2011) 4414-4419.

[3] *Kim Hyung-Gon, Kim Wha-Tek.* Optical absorption in $ZnGa_2S_4$ and $ZnGa_2S_4$:$Co^{2+}$ crystals Physical Review B (condensed matter), 41 Issuse12 (1990) 8541-8544.

[4] *Claudia Weckeder, Shuang Zhang and Hartmu Haeuseler*. Photoluminescence of $ZnGa_2S_4$ : $Eu^{2+}$, Z. Kristallograf, 220 (2005) 277-280.

[5] *V.L. Panyutin, B.E. Ponedelnikov, A.E. Rozenson, B.I. Chijikov.* FTP, т.15, в.2 (1981) 311-315.

[6] *Yu.O. Derid, E.I. Kozachenko, S.I. Radautsan, I.M. Tiginyanu.* Radiative recombination in $ZnGa_2S_4$ single crystals Phys. Stat. sol. (a), 113 (1989) k 265-266.

[7] *I.G. Nasibov, I.A. Mamedova, Z. Kadiroqlu, T.G. Kerimova.* Izvestiya NAN Azərb. Fiz.-tex. i mat. nauk (Transactions), XXXVI, N2 (2016) 28-31. (In Russian).

[8] *J.A. Beun, R. Nitsche, and M. Lichtensteiger.* Physica 27, 448 (1961) 448-452.

[9] *A. Aneda, L. Garbato, F. Raga, A. Serpi.* Phys. St. Sol.(a), v.46, N2(1978) 589-593.

[10] *H. Hahn, G. Frank, W. Klinger, A. D. Storger and G. Storger.* “Untersuchungen Uber Ternare Chalkogenide. VI. Uber Ternare Chalkogenide des Aluminiums, Gal- liums und Indiums mit Zink, Cadmium und Quecksilber,” Zeitschrift fur Anorganische und Allgemeine Chemie, Vol. 279, No. 5-6 (1955) pp. 241-270.

[11] *K. Charlotte, Lowe-Ma and Tezzell A. Wanderall.* Structure of $ZnGa_2S_4$ a defect sphalerit derivated, Acta Cryst, 47 (1991) 919-924.

[12] *E.W. Williams.* Evidence for self-activated luminescence in GaAs: The gallium vacancy-donor center, Physical Review, 168, 3(1968) 922-928.


*Received:15.02.2018*

# THE PRODUCTION OF HIGGS BOSON ON POLARIZED COLLIDING LINEAR $e^+e^-$ COLLIDERS AND SUPERSYMMETRY

**F.T. KHALIL-ZADE**
*Institute of Physics of Azerbaijan NAS, H.Javid ave.,33, Baku*

Taking into account the polarizations of the linear colliding electron-positron beams, differential cross-sections of the process $e^+ + e^- \to \tilde{\mu}_a + \overline{\tilde{\mu}}_b + H$ are calculated. The characteristic features of the differential cross-sections and the polarization effects of the process on the linear accelerator ILC (International Linear Collider) are investigated.

**Keywords:** Standard Model, ILC, Higgs boson, Lepton production, $e^-e^+$ interactions.
**PACS:** 12.15-y, 13.66.Fg, 14.80-j, 14.70 Hp

## INTRODUCTION

As it is known the search of possible deviations from Standard Model and physics being in its base [1-4] is the one of the main directions of experimental programs of Large Hadron Collider (LHC) in CERN in such projects as ATLAS and SMS. The supersymmetry is the one of the powerful and attractive conceptions in theoretical particle physics stimulating the search of New Physics. The number of theoretical articles studying the structure and consequences of supersymmetric theories is calculating by thousands. The experimental search of supersymmetry revealings is also intensive one.

This series of works becomes the very important last years when Large Hadron Collider has the total power. The collaborations as ATLAS and SMS now carry out the more than hundreds diferent searches of particles-super-partners and they are still negative ones. Before LHC starting up the physicists carry out the very simple realizations as Minimal Supersymmetric Standard Model (MSSM) [5-6].

The scientists hope that as soon collider is starting up the new particles reveal themselves very rapidly and then one can take the adaptation in framework of this or that realization. But situation becomes another one. Run1 doesn't make any discoveries and physicists become the search more wider. But even in such extended searches ther are no any garanties that particles-superpartners will be acessible for discovery on LHC as experiments themselves carried out on proton-proton collisions aren't 'pure" and "dirty" strong interactions. Inspite of the fact that LHC doesn't reval anything this fact doesn't ignor the supersymmetry idea itself.

The modern investigations in high energy regions on LHC in CERN in nearest future will be added by investigations on electron-positron linear colliders, in particular, on ILC (International Linear Collider) [7]. The pure signals and accurate measurements which can be obtained with the help of linear collider of high luminosity give us the possibility for new ideas in our understanding of fundamental interactions of nature and substance structure, space and time. Moreover, experiments with polarized beams play the essential role as the diferent polarized characteristics can be used for significant increase of signal velocity and also for effective suppression of undesirable background processes.

$e^+ + e^- \to \tilde{\mu}_a + \overline{\tilde{\mu}}_b + H$ process on polarized colliding $e^+e^-$- beams in framework of MSSM had been considered earlier in work [8]. The differential cross-section by $\tilde{\mu}_a\overline{\tilde{\mu}}_b$-pair invariant mass, process total cross-section are investigated in detail and also character features in behaviour of cross-sections and process polarization characteristics are revealed in this work (at $m_H = 10\,GeV$).

The necessity in calculation of characteristics of this process is appeared in connection with the discovery of the Higgs boson on LHC by collaborations ATLAS and SMS and planning investigations on electron-positron linear colliders in particular on ILC (International Linear Collider).

## 1. PROCESS $e^+ + e^- \to \tilde{\mu}_a + \overline{\tilde{\mu}}_b + H$ $(a,b = 1,2)$. ON POLARIZED COLLIDING ELECTRON-POSITRON LINEAR COLLIDERS

The present work is dedicated to investigation of process of scalar muon-antimuon pairs production on polarized colliding electron-positron linear colliders with H- boson radiation.

$$e^+ + e^- \to \tilde{\mu}_a + \overline{\tilde{\mu}}_b + H \quad (a,b = 1,2). \tag{1}$$

The differential cross-section of the process on $\tilde{\mu}_a\overline{\tilde{\mu}}_b$ -pair invariant mass is calculated taking under consideration of arbitrary polarizations of colliding electron-positron beams [1]. The investigations of differential cross-sections of considered process for energies of ILC initial beams are carried out and the character features in behavior of cross-sections and process polarized characteristics are revealed.

Note that the process

$$e^+e^- \to \mu^+ + \mu^- + H. \tag{2}$$

131 H.Javid ave, AZ-1143, Baku
ANAS, G.M.Abdullayev Institute of Physics
E-mail: jophphysics@gmail.com

is the main competitive process in considered case.

A detailed analysis of different characteristics of the process (2) is devoted to [9-16].

The (1) process amplitude is written in the following form:

$$M = i2^{3/4} G_F^{3/2} D_Z(q_1) D_Z(q_2) H(\chi) sin(\beta - \alpha) \sum S_{ab} \cdot$$
$$\bar{u}(-p_2)\gamma_\mu (g_V - g_A\gamma_5) u(p_1)(k_1 - k_2)[\delta_{\mu\nu} - q_{2\mu}q_{2\nu}/m_Z^2], \quad (3)$$

where

$$D_Z(q_i) = (1 - q_i^2/m_Z^2 + i\Gamma_Z m_Z)^{-1}, \quad S_{ab} = \sum_{c=1}^{2} \lambda_c R_{ac} R_{bc}^*,$$

$\Gamma_Z$ and $m_Z$ are width and mass of $Z$-boson, $q_1 = p_1 + p_2 = k_1 + k_2 + \chi$, $q_2 = p_1 + p_2 - \chi = k_1 + k_2$; $p_1, p_2, k_1, k_2$ and $\chi$ are $4$ - impulses of electron, positron, scalar muon, scalar antimuon and $H$-бозона correspondingly, $\lambda_1 = g_V + g_A, \lambda_2 = g_V - g_A$, $g_V = -1/2 + 2sin^2\theta_W$, $g_A = -1/2$, $R_{ab}$ is matrix diagonalizating the mass matrix of scalar leptons, $sin(\beta - \alpha)$ is multiplier caused by $HZZ$ interaction, $tg\beta = \langle H_2^0 \rangle / \langle H_1^0 \rangle$, angle $\alpha$ appears at transition from weak to mass basis for Higgs boson and it is defined by expression:

$$sin2\alpha = -\frac{m_h^2 + m_H^2}{m_h^2 - m_H^2} sin2\beta .$$

Here $m_h$ and $m_H$ are masses of heavy and light Higgs boson (in comparison with Higgs boson mass).

Note that the interaction constant of scalar muons with $H$-boson is proportional to $sin(\alpha + \beta)$ and if we are limited by consideration of $\beta = -\alpha \approx \pi/4$ angles then in the given case the diagram contribution with $H$-boson radiation by scalar muons is negligible small one.

Further we will consider the following possibilities of scalar muon production:

1) production of scalar muons $\tilde{\mu}_1 \bar{\tilde{\mu}}_1$

$$e^+ + e^- \to \tilde{\mu}_1 + \bar{\tilde{\mu}}_1 + H, \quad (4)$$

in this case we have $S_{ab} = \lambda_1 cos^2\phi + \lambda_2 sin^2\phi$ where $\phi$ is mixing angle of left and right scalar muons:

2) production of $\tilde{\mu}_2 \bar{\tilde{\mu}}_2$ - pair

$$e^+ + e^- \to \tilde{\mu}_2 + \bar{\tilde{\mu}}_2 + H, \quad (5)$$

in this case $S_{ab} = \lambda_1 sin^2\phi + \lambda_2 cos^2\phi$;

3) production of $\tilde{\mu}_1 \bar{\tilde{\mu}}_2$ - pair

$$e^+ + e^- \to \tilde{\mu}_1 + \bar{\tilde{\mu}}_2 + H, \quad (6)$$

in this case $S_{ab} = -(\lambda_1 - \lambda_2) sin\phi cos\phi$;

4) production of left scalar muons

$$e^+ + e^- \to \tilde{\mu}_L + \bar{\tilde{\mu}}_L + H, \quad (7)$$

in given case $S_{ab} = \lambda_1$;

5) production of right scalar muons

$$e^+ + e^- \to \tilde{\mu}_R + \bar{\tilde{\mu}}_R + H, \quad (8)$$

here $S_{ab} = \lambda_2$. For the case of production of left and right scalar muons $S_{ab} = 0$.

All numerous calculations are carried out at mixing angle value $\phi = \pi/4$ and $m_h = 135$ *GeV*. It is obvious that in this case the cross-sections of (4) and (5) processes are similar ones.

Carried out the calculations on (3) base at arbitrary polarization of initial beams colliding in center-of-mass system we obtain the following expressions for differential cross-section of process (1):

$$\frac{d\sigma}{dx d\Omega} = \frac{d\sigma_0}{dx d\Omega}\{1 + [(\vec{n}\vec{s}_1) + (\vec{n}\vec{s}_2)]b_1 + [(\vec{s}_1\vec{s}_2)sin^2\theta +$$
$$+ 2((\vec{n}\vec{s}_1)(\vec{n}_\chi\vec{s}_2) + (\vec{n}\vec{s}_2)(\vec{n}_\chi\vec{s}_1))cos\theta -$$
$$2(\vec{n}_\chi\vec{s}_1)(\vec{n}_\chi\vec{s}_2)]b_2 + (\vec{n}\vec{s}_1)(\vec{n}\vec{s}_2)b_3\}, \quad (9)$$

where

$$\frac{d\sigma_0}{dxd\Omega}=\frac{G_F^3 s^2 r_Z^8 \beta_H}{3\sqrt{2}\cdot 2^{11}\pi^4 x^3}\left[1+\frac{x-2(r_a^2+r_b^2)}{r_Z^2}\right]^2\times$$
$$\times\frac{sin^2(\beta-\alpha)\sum_{a,b}\left|S_{ab}\right|^2\{[x-(r_a+r_b)^2][x-(r_a-r_b)^2]\}^{1/2}}{[(1-r_Z^2)^2+\Gamma^2][(x-r_Z^2)^2+\Gamma^2]}B_0 \quad (10)$$

is cross-section of process (1) averaged on particle polarization. The following designations are taken in (9) and (10):

$$b_i=B_i/B_0 \qquad (i=1,2,3)$$
$$B_0=(g_V^2+g_A^2)\{8x[x^2-2x(r_a^2+r_b^2)+(r_a^2-r_b^2)^2]+$$
$$+\beta_H^2[x^2-2x(r_a^2+r_b^2)+4(r_a^2-r_b^2)^2]sin^2\theta\},$$
$$B_1=2g_V g_A B_0/(g_V^2+g_A^2),$$
$$B_2=(g_V^2-g_A^2)\beta_H^2[x^2-2x(r_a^2+r_b^2)+4(r_a^2-r_b^2)^2],$$
$$B_3=B_0-(1+cos^2\theta)B_2. \quad (11)$$

In expressions given below $\vec{s}_1$ and $\vec{s}_2$ are unit vectors in polarization directions of electron and positron correspondingly; $\vec{n}$ and $\vec{n}_\chi$ are unit vectors in directions of impulses of electron and $H$-boson in relation to direction of electron impulse; $\beta_H=[(1+r_H^2-x)^2-4r_H^2]^{1/2}$, $r_Z=m_Z/\sqrt{s}$, $r_a=m_a/\sqrt{s}$, $r_b=m_b/\sqrt{s}$, $\Gamma=r_Z\Gamma_Z/\sqrt{s}$; $m_H$, $m_a$ and $m_b$ are masses of $H$-boson and $\tilde{\mu}_a$ and $\tilde{\mu}_b$ scalar muons correspondingly.
The value $x$ is invariant mass of final scalar fermion pair in $s$ units, $x=(k_1+k_2)^2/s$ is limited to $(r_a+r_b)^2$ to $(1-r_H)^2$.
Let's analyze the (9) formula in different cases of initial beam polarizations.

## 2. CASE OF UNPOLARIZED COLLIDING BEAMS

In case of unpolarized colliding beams the differential cross-section of the process (1) is defined by formula (10). Integrating (10) over angles for differential cross-section on $\tilde{\mu}_a\bar{\tilde{\mu}}_b$-pair invariant mass of process we obtain the following expression:

$$\frac{d\sigma}{dx}=\frac{G_F^3 s^2 r_Z^8 \beta_H}{9\sqrt{2}\cdot 2^8\pi^3 x^3}\left[1+\frac{x-2(r_a^2+r_b^2)}{r_Z^2}\right]^2\times$$
$$\times\frac{sin^2(\beta-\alpha)\sum_{a,b}\left|S_{ab}\right|^2\{[x-(r_a+r_b)^2][x-(r_a-r_b)^2]\}^{1/2}}{[(1-r_Z^2)^2+\Gamma^2][(x-r_Z^2)^2+\Gamma^2]}C_0, \quad (12)$$

Where

$$C_0=(g_V^2+g_A^2)\{12x[x^2-2x(r_a^2+r_b^2)+(r_a^2-r_b^2)^2]+$$
$$+\beta_H^2[x^2-2x(r_a^2+r_b^2)+4(r_a^2-r_b^2)^2]\}. \quad (13)$$

The dependences of differential cross-section (12) on $x$ at $\sqrt{s}=350\,GeV$ and $\sqrt{s}=500\,GeV$, at $m_H=125$ $GeV$ and $m_{\tilde{\mu}_a}=m_{\tilde{\mu}_b}=94$ $GeV$ [17] are presented in fig.1 and 2.

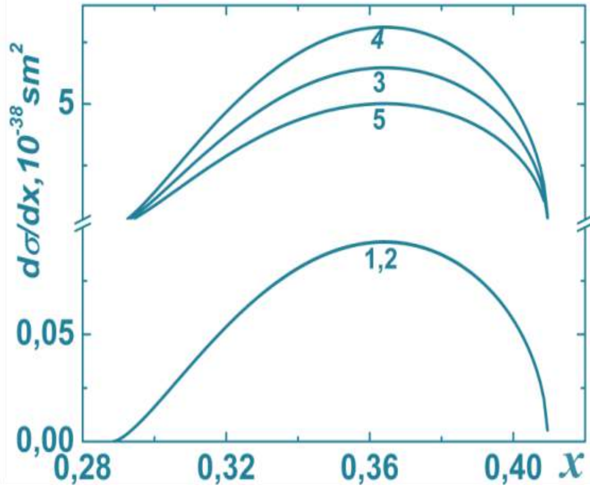


*Fig.1.* The dependence of differential cross-section of $e^+ + e^- \to \tilde{\mu}_a + \bar{\tilde{\mu}}_b + H$ process on $x$ at $\sqrt{s} = 350\, GeV$

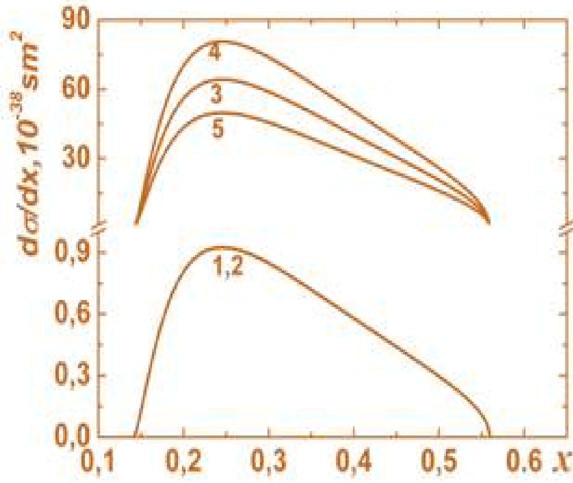


*Fig.2.* The dependence of differential cross-section of $e^+ + e^- \to \tilde{\mu}_a + \bar{\tilde{\mu}}_b + H$ process on $x$ at $\sqrt{s} = 500\ GeV$

The following numeration of curves are taken in fig.1 and 2: 1 is related to process (4), 2 is related to process (5), 3 is related to process (6), 4 is related to process (7), 5 is related to process (8). In addition, here and below $sin^2\theta_W = 0,22$, $m_Z = 91\, GeV$ and $\Gamma_Z = 2,49\, GeV$ [17].

As it is seen from the figures there are maximums in differential cross-sections of the processes (4) – (8). At energies of initial beams $\sqrt{s} = 350\, GeV$ the maxima of processes (4) – (8) are at $x{\sim}0,37$ and don't exceed the value $d\sigma/dx < 7 \cdot 10^{-38} cm^2$ (fig.1). From fig.2 it is seen that at energies of initial beams $\sqrt{s} = 500\, GeV$ the maxima of processes (4) – (8) are at $x{\sim}0,25$ where the differential cross-section of (4) – (8) processes is larger by one order.

As it is above mentioned the process (2) is the main competitive process in considered case. Note that at energies of initial beams $\sqrt{s} = 500\, GeV$ and $x{\sim}0,25$ the differential cross-section of process (2) is approximately smaller by two orders than the ones of processes (4) and (5) and it is smaller by five orders than cross-sections of processes (6) – (8) (see fig.3 in work [18]).

## 3. THE CASE OF LONGITUDINAL POLARIZED LINEAR COLLIDING BEAMS

As it is seen in ILC plans the high degree longitudinal polarization of electron and positron is predicted [7]. In this connection let's consider the differential cross-section of process (1) taking under consideration the longitudinal polarizations of initial particles. In this case the differential cross-section of process (1) has the form:

$$\frac{d\sigma(h_-, h_+)}{dx d\Omega} = \frac{d\sigma_0}{dx d\Omega}[1 - h_- h_+ + (h_- - h_+) b_1], \quad (14)$$

where $h_-$ and $h_+$ are longitudinal polarizations of electron and positron correspondingly.

The quantity $b_1$ defines the spin asymmetry caused by the difference $h_- - h_+$

$$A_s = b_1 = 2 g_V g_A (g_V^2 + g_A^2). \quad (15)$$

The polarization effect of electron beam found on the base of (4) formula has the form:

$$N(h_-) = -h_- b_1 / (2 + h_- b_1). \quad (16)$$

The polarization effect of positron beam is described by the formula obtained from (16) by substitution $h_- \to = -h_+$.

The spin asymmetry (15) and polarization effect of (16) beam are related to both to differential cross-sections by $dx d\Phi$, $d\Phi$ and $dx$ separately. At value of Weinberg angle $sin^2\theta_W = 0,22$ is equal to $A_s = 23,7$ %. The beam polarization effect which at value of Weinberg angle $sin^2\theta_W = 0,22$ is equal to $N(h_- = 1) = N(h_+ = -1) = -10,6$ % and $N(h_- = -1) = N(h_+ = 1) = 13,4$ % has the same property.

Note that in ILC at $h_- = 0,8$ the polarization effect of electron beam is $N(h_- = 0,8) = -10,4$ % and at $h_+ = 0,5$ the polarization effect of positron beam is $N(h_+ = 0,5) = -0,56$ %.

## CONCLUSION

In conclusion we note that the spin asymmetry and beam polarization effect in processes (1) and (2) differ by the sign (see [8] and [18] for comparison) that can be the well test for identification of supersymmetry.

The given work is supported by Science Development Foundation under the President of the Republic of Azerbaijan – **Grant № EİF-KETL-2-2015-1(25)-56/02/1.**

---


[1] The ALAS Collaboration. Atlas detector and physics performance. Technical Design Report, Volume I, ATLAS TDR 14, CERN/LHCC 99-14, p. 1- 475. 1999.

[2] The ALAS Collaboration. Atlas detector and physics performance. Technical Design Report, Volume II, ATLAS TDR 15, CERN/LHCC 99-15, p. 1- 521.

[3] The CMS Collaboration. CMS Physics TDR: Volume I (PTDR1), Detector Performace and Software. CERN/LHCC 2006-001,p.1-547, 2006.

[4] The CMS Collaboration. CMS Physics TDR: Volume II (PTDR1), Detector Performace and Software. CERN/LHCC 2006-021, p.1-669, 2006.

[5] *H.P. Nilles.* Supersymmetry, supergravity and particle physics. Phys. Rep. v.110C, p.1-162, 1984.

[6] *H.E. Haber, G.L. Kane.* The search for supersymmetry: Standard Model. Phys. Rep. v.117C, p.1-189, 1985.

[7] *A. Abada et all.* THE INTERNATIONAL LINEAR COLLIDER. Technical Design Report, Volume 2: Physics. EDMS Nr.: D00000001021165 Rev: A Ver: 1 Status: Released - for publication Dat.: 11. Jun 2013.

[8] *T.M. Aliev, F.T. Khalil-zade.* YaF, t. 48, vip. 5(11), str. 1461-1465, 1988. (In Russian).

[9] *J. Ellis, M.K. Gaillard, D.V. Nanopoulos.* A Phenomenological Profile of the Higgs Boson**.** Nucl.Phys. B106, p.292-340, 1976.

[10] *R.L. Kelly, T. Shimada.* Dilepton signature in $e^+e^-\rightarrow Hl^+l^-$ . Phys. Rev., D23, p.1940-1956,1981.

[11] *E. Ma, J. Okada.* Possible means of detecting the Higgs boson in $e^+e^-$ annihilation. Phys. Rev. D 20, p.1052-1070,1979.

[12] *T. Morioka, M. Biyajima, O. Terazawa.* Detection of Light Standard Higgs Particle in $e^+e^-$ Annihilation. Prog. Theor. Phys 76 (5), p.1089-1097, 1986.

[13] *N.A. Guliev, I.G. Djafarov, V.Ya. Faynberq, F.T. Khalil-zade.* Ya.F, t. 40, vip. 1(7), str. 174-180. 1984. (In Russian).

[14] *N.A. Guliev, I.G. Djafarov, V.Ya. Faynberq, F.T. Khalil-zade.* Kratkie Soobsheniya po Fizike. №11, str. 35-40, 1983. (In Russian).

[15] *Y. Abe et all.* Beam polarization effects on Higgs particle production in $e^+e^-$ annihilation. Lett. al Nuovo Cim. Volume 32, Issue 13, p. 361-365, 1981.

[16] *N.A. Guliev, I.G. Djafarov, F.T. Khalil-zade. R.Sh. Yaxyaev.* Preprint №107, Institut Fiziki AN Azerbaydjanskoy SSR, str. 1-23, Baku-1984. (In Russian).

[17] *C. Patrignani et al.* Particle Data Group. Chinese Physics C Vol. 40, No. 10, pp. 1-101808, 2016.

[18] *F.T. Khalil-zade.* The production of the Higgs boson on electron-positron linear colliders. “Fizika“,vol. XXII, №1,pp. 8-17, 2018.


*Received: 04.01.2018*

# SPECTRA OF OPTICAL PARAMETERS OF $Bi_2Te_3$ FILM IN 1÷6 eV INTERVAL

**N.Z. JALILOV**

*Institute of Physics of Azerbaijan NAS*
*Az-1143, H.Javid ave.,33 Baku*
*xmamedova1986@gmail.com*

Reflection spectra *R(E)* of $Bi_2Te_3$ film samples in energy interval1÷6 eV of beam falling normally on the surface are measured in work.

**Keywords:** reflection coefficient, optical conduction.
**PACS:** 535.3; 539.2/6: 539./.04

## 1. INTRODUCTION

*R(E)* reflection coefficients of some materials (amorphous and monocrystalline) Se, Se-S, $InSnTe_2$, $TlIn_{0.9}Ce_{0.1}Se_2$, $TlInSe_2Ce_{0.04}$, $TlInSe_2$, $Cu_3GdTe_3$, $Cu_5GdTe_4$, $CuGdTe_2$, $Se_{95}As_5$ (with Sm impurity), $Bi_2Te_3$(Ni, Cu, Zn), $Bi_2Te_3$, $Bi_2Se_3$) are measured by us and their optical parameters such as reflected light phase $\theta$, indexes of absorption $\kappa$ and refraction $n$, real $\varepsilon_1$and imaginary $\varepsilon_2$ parts of dielectric constant, α absorption coefficient, function of characteristic $-Img\ \varepsilon^{-1}$ volume and $-Img(\varepsilon+1)^{-1}$ surface electron loss, electro-optical differential functions$(\alpha,\ \beta)$, optical conduction $\varepsilon_2 E$, integral function of bound state density $\varepsilon_2 E^2$, effective static dielectric constant $\varepsilon_0$(E), effective number of valence electrons $n_{ef}(E)$ [1] taking part in transitions up to the given $E$ energy, are calculated.

Bismuth telluride is known as effective material for thermo-electric transformations. This material is easy to prepare in the form of perfect single crystals and obtain n- and p-types by doping [2,6]. $Bi_2Te_3$ crystals have the packet structure and the bound between neighbor packets has the mixed Van-der-Waals covalent character [7]. The additional bound because of transition of one p-electron on d-levels and overlapping of some d-levels with valence band takes place between packets. All this facts causes the significant metallic properties and comparably small values of its forbidden band energy in 0,15÷0,35 *eV* interval. $Bi_2Te_3$ and its analogies are the uniaxial crystals in optical respect. The dielectric constant in them is the tensor of second order and depends on falling wave direction in respect of C optical axis. The optical properties of bismuth telluride are investigated in region of higher frequencies in work [5].

The structure of crystal bands is theoretically calculated in work [5]. The absence of data on value of spin-orbit interaction ($\Delta$) and character complexity of chemical bond between $Bi_2Te_3$ atoms make significant difficulties. Bismuth telluride and solid solutions on its base apply at preparation of different energy transformers [7].The single-crystal or polycrystalline $Bi_2Te_3$ and its solid solutions with $Bi_2Se_3$ are mainly used. The single crystal samples $Bi_2Te_3$ are easily splitted off by cleavage planes [0001] forming the mirror surface which is stable to oxidation that is very important for carrying out of optical measurements and doesn't require the special chemical treatment.

The study of $Bi_2Te_3$ band structure hasn't achieved such level as germanium, $A^{III}B^{V}$ compounds that is connected with the complexity of its crystal and band structure [3].This makes necessary for new investigations in this direction. The measurement of crystal reflection coefficient of n- and p-types parallel and perpendicularly to C axis and also its polycrystalline film samples and definition of spectra of their optical parameters on the base of reflection coefficient are the task of the given work.

## 2. EXPERIMENT TECHNIQUE

The split of $Bi_2Te_3$ single crystals having the mirror surface is used for measurement of R(E) reflection coefficient. The reflection coefficient is measured by method of two-beam spectroscopy. The crystals are doped by Cl impurities having n-type conduction and Tb impurities having p-type conduction.

The obtaining technology of $Bi_2Te_3$ single crystals and films is described in works [8,9,10]. The single crystals are obtained by Bridgman method as in [3] and $Bi_2Te_3$ films by thickness 0,3mkm of polycrystalline on the split of rock salt crystals are its sublimation in vacuum. The definition methods of optical parameters are given in work [11] and procedure is explained in [12].

The special computer programs are used for calculation of optical parameters. The optical parameters of investigated materials are calculated by programs made by work author [13]. These programs are checked at calculation of optical parameters of some materials in works [14 – 18].

## 3. THE RESULTS AND THEIR DISCUSSION

R(E) reflection coefficients of single-crystal of n- and p-types parallel and perpendicularly to C axis and also its film samples of n- and p-types are measured in the work and spectra of their optical parameters: α absorption coefficient, $\varepsilon_1$ real and $\varepsilon_2$ imaginary parts of dielectric constant, indexes of $\kappa$ absorption and $n$ refraction, effective number of valence electrons $n_{ef}(E)$ taking part in transitions up to the given $E$ energy, $\varepsilon_0(E)$ effective static dielectric constant, $Img(\varepsilon+1)^{-1}$ surface electron loss, θ reflected light phase, $\varepsilon_2 E$ optical function of characteristic $-Img\ \varepsilon^{-1}$ volume and –conduction, $\varepsilon_2 E^2$ integral function of bound state density and $(\alpha,\ \beta)$ electro-optical differential functions are defined.



131 H.Javid ave, AZ-1143, Baku
ANAS, G.M.Abdullayev Institute of Physics
E-mail: jophphysics@gmail.com

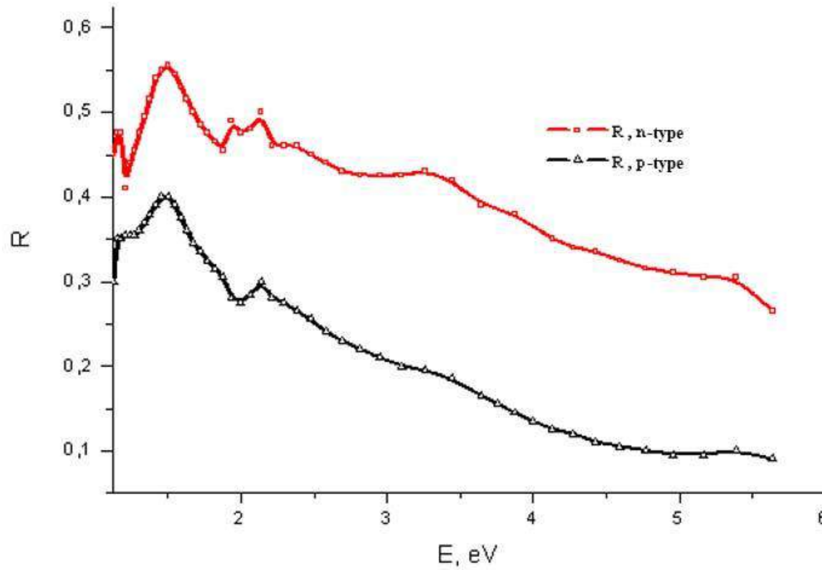


*Fig.1.* Reflection spectra of film $Bi_2Te_3$ of n- and p-types.

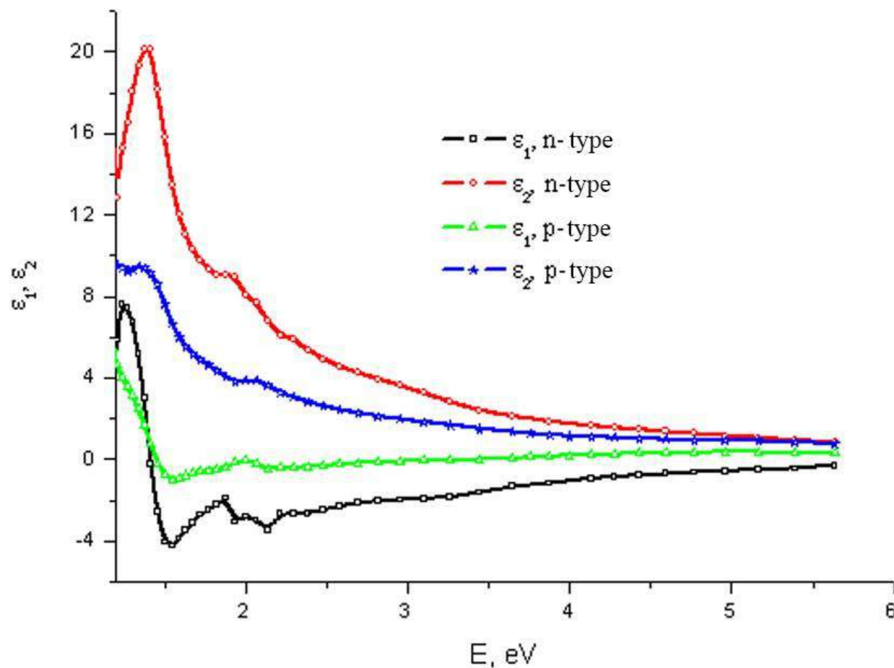


*Fig.2.* Spectra of coefficients $\varepsilon_1$ and $\varepsilon_2$ of film $Bi_2Te_3$ of n- and p-types.

Only R(E) reflection coefficients, $\varepsilon_1$ real and $\varepsilon_2$ imaginary parts of dielectric constant, function of characteristic $-Img\ \varepsilon^{-1}$ volume and $-Img(\varepsilon+1)^{-1}$ surface electron loss, spectra of electro-optical differential functions $(\alpha, \beta)$, spectra of optical conduction of $\sigma$ massive and film samples correspondingly are presented in fig.1-10 and values of interband optical transitions defined by maximums of $\sigma$ optical conduction are presented in tables 1 and 2.

The given data give us the possibility to compare the optical spectra, transitions of $Bi_2Te_3$single crystals and film samples. The transitions 1,4eV and 1,1eV are found by authors of work [5] for the case of high energies for $Bi_2Te_3$ single crystals. As it is seen from table 1 the same transitions are observed for n- and p-types correspondingly. As it is seen from table 2 the transitions corresponding to energies 1,4eV and 1,15eV are found for $Bi_2Te_3$ film samples of n- and p-types. From this we can conclude that values of some optical transitions for noncrystalline samples at material transition from crystalline to noncrystalline state are saved.

As it is mentioned in [18] the study of absorption transitions in materials is impossible because of absorption big value in region of interband transition energies $E>E_g$ ($E_g$ is forbidden band width). The reflection is the one effective method.

The analytical singularities of imaginary part of complex dielectric constant $\varepsilon_2(E)$ and $dN/dE$ functions

connected by state density almost coincide and interband space gradient makes the main contribution in *dN/dE* functions:

$$\frac{dN_{ij}}{dE} \sim \int \frac{dS_k}{\left|\nabla_k E_{ij}\right|} \quad , \qquad (1)$$

where $E_{ij}(k)=E_j(k)-E_i(k)$ is distance between conduction and valence bands. *dN/dE* values near critical points in *k*-space defined by expression and also the position of critical points and transition type can be theoretically calculated from band structure.

The analysis of $\varepsilon_2(E)$, *dN/dE* functions and *R(E)* reflection coefficient shows that disposition and character of maximums in their spectra are similar or very close ones. That's why one can define the values of corresponding interband intervals and band nature with the help of direct comparison of experimental data in $E>E_g$ region with theoretical calculations of *dN/dE* function. As it is mentioned in [18] $E_0$ resonance frequency presents itself that frequency at which $2nk \cdot E$ conduction achieves maximum by which the interband transitions are defined. The high transparency in wide $E<E_g$ energy region is character for noncrystalline materials and several methods of $E_g$ definition are known.

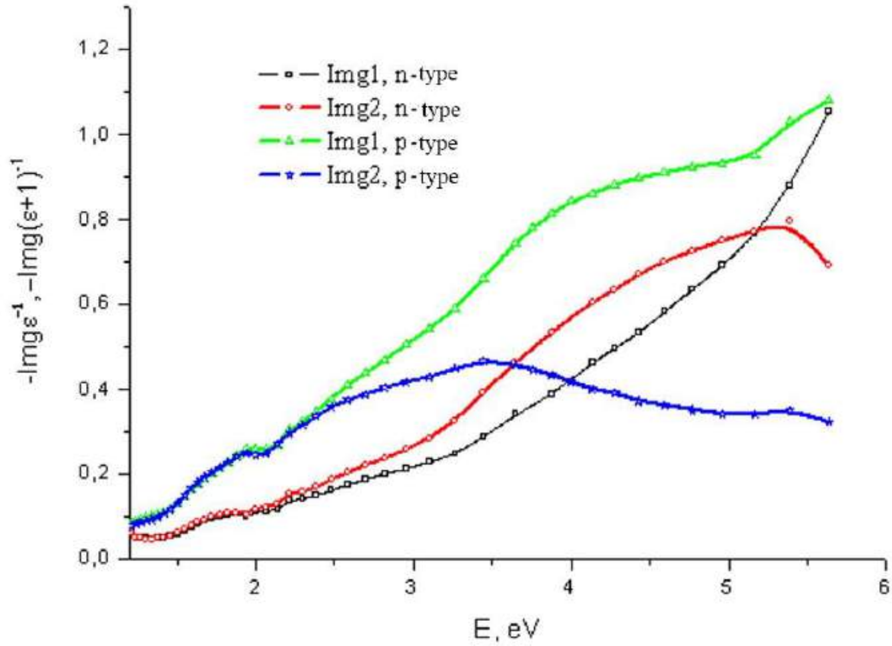


*Fig.3.* Spectra Img1 ($-Img\varepsilon^{-1}$) and Img2 ($-Img(1+\varepsilon)^{-1}$ of film $Bi_2Te_3$ of n- and p-types.

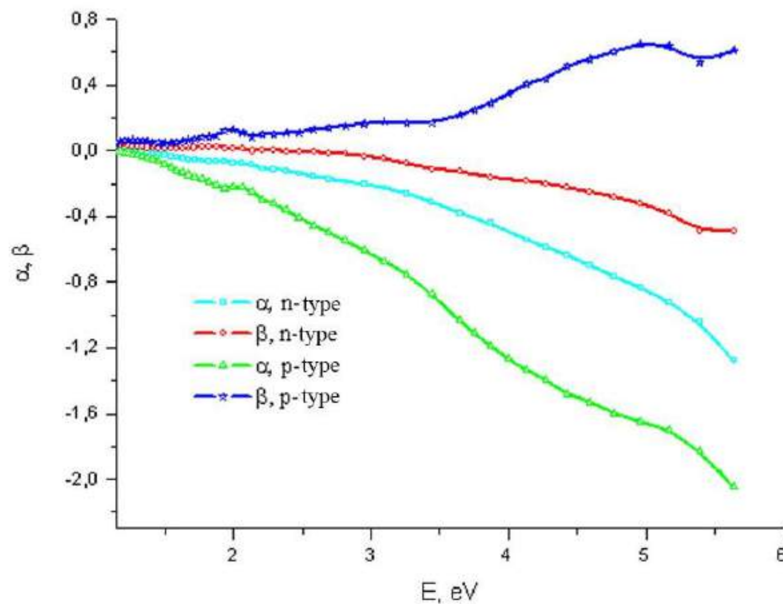


*Fig.4.* Spectra of electro-optical coefficients $\alpha$ and $\beta$ of $Bi_2Te_3$ film of n- and p-types.

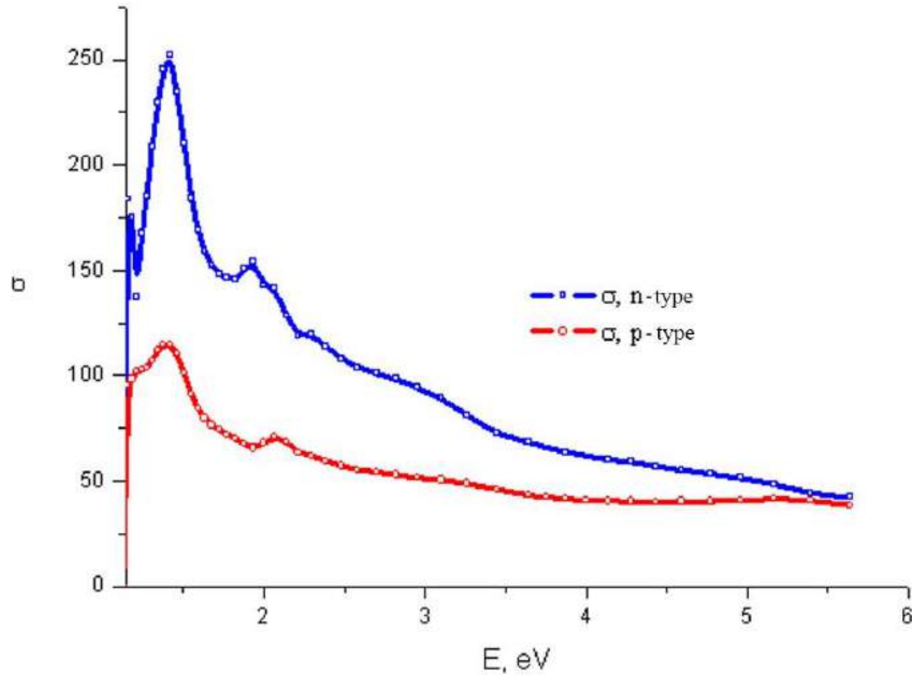


*Fig.5.* Optical conduction spectraσ of $Bi_2Te$ film of n- and p-types.

Table 1.

| Optical transitions in film $Bi_2Te_3$ in energy interval1÷6 eV of n- and p-types defined by optical conduction maximums. | |
|---|---|
| n - type | p - type |
| 1.15 | 1.15 |
| 1.37 | 1.19 |
| 1.41 | 1.37 |
| 1.84 | 1.41 |
| 1.93 | 2.05 |
| 2.06 | 2.13 |
| 2.29 | - |

The transparency estimation by the level of *α(E)* absorption coefficient of long-wave edge is the one of these methods. $E_g$ detail value for noncrystalline semiconductors is discussion one and usually the discussion of *α(E)* spectrum character in Urbach and Tauz models is carried out without $E_g$ estimations [20,21]. $E_g$ is defined by Tauz model for $\alpha(E) = 10^3 cm^{-1}$ value.

As it is mentioned in [20] N(E) state density is the similarly available conception for crystalline and noncrystalline substances. By existing results of experimental data the step of state density in noncrystalline substance not strongly differs from the corresponding one in crystal. In first case the thin structure can be blurred and local states can appear in forbidden band. The band structure saves as it is defined by short-range order in materials.

The author of work [22] notes that it is impossible to delimit the single crystal, polycrystalline and amorphous substance state. The presence of band structure which are forbidden and conduction bands can be obtained from short-range order and for such conclusion there is no need to require the atom periodic disposition.

As authors show [23 – 25] the structure of disordered binary compound can be considered as the assemblage of different basis clusters presented in structural matrix with different static height and put into effective medium. As authors of work [26] note the short-range order makes the main contribution into electron state density. However, as short-range order in binary compounds can significantly change from node to node in structural matrix of amorphous substance then especially statistics of basis clusters defines the final electron state density.

Thus, low-molecular structural configurations can appear at melt cooling or in process of amorphous substance formation by another way that is accompanied by definite advantage in energy. Such formations can't serve neither as crystal germs nor as growth centers of solid amorphous phases because of the fact that they are characterized by special symmetry.

The ambiguity of structural ordering in compositional amorphous solid substances of type can be considered as their general property. The peculiarities of short-range ordering near each node are caused firstly by physical methods of $A_xB_{1-x}$ system preparing, secondly by principle of chemical ordering taking into consideration the "rule 8-N" [20] and values of bound energies of neighbor atoms.

The decay of ideal structure in noncrystalline solid substance takes place in systems including atoms with lone-electron pairs. Often at bound breakage the electron pair stay on the one of fragments, i.e. the heterolytic bound breakage takes place. The one positive and one negative charged defect centers in sort-range orders appears. The energy necessary for bound breakage is partly compensated by existing lone-electron pair of atoms being near and number of chemical bounds doesn't change. Thus, there is structural disordering along with density oscillations and topological disordering of different types in homogeneous noncrystalline materials of stoichiometric composition. It is revealed in the form of positive and negative charged defect centers as in the case of point defects in crystals. As a result the reaction defects the formations of which are characterized by least change of free energy, dominate.

The short-range order idea at formation of electron energy bands is the one of fundamental conceptions in physics of disordered systems. This idea has experimental and theoretical demonstration on example of many noncrystalline solid and liquid semiconductors [27]. The formation mechanism of valence and conduction bands in noncrystalline semiconductors is formed mainly by work authors [28,29]. In works of these authors the similarity of main peculiarities of spectral dependence of imaginary part of $\varepsilon_2(E)$ dielectric constant for noncrystalline semiconductors and their crystal analogues is emphasized. This similarity is shown on example of selenium [28]. The analogous conclusion is made in relation to $a$-$As_2S_3$ and $a$-$As_2Se_3$ of works [28,29]. For cases of amorphous materials only maximum smoothing takes place in their $\varepsilon_2(E)$, but similarity of curves for amorphous and crystalline samples is saved.

Nowadays it is established that one can directly change the optical, photo-electric and electric properties of noncrystalline semiconductors with change of chemical composition and also by introduction of impurities. The change if concentration of charged defect centers $D^+$ and $D^-$ ($U^{-1}$-centers) in them takes place and these defects form from initial neutral defects $D^0$ by reaction:

$$2D^0 \rightarrow D^+ + D^- , \qquad (2)$$

which can be eigen or impurity and mixed defects which give us the possibility to control by their physical properties.

## CONCLUSION

Thus, $R(E)$ reflection coefficients of single crystals and $Bi_2Te_3$ film samples of n- and p-types in energy interval 1÷6 eV of beam falling normally on surface are measured in work. For case of $Bi_2Te_3$ single crystals the measurements are carried out parallel and perpendicularly to C axis. It is shown that for noncrystalline samples the values of some optical transitions $Bi_2Te_3$ from crystal to noncrystalline state are saved.

Only spectra of $R(E)$ reflection coefficients, $\varepsilon_1$ real and $\varepsilon_2$ imaginary parts of dielectric constant, functions of characteristic $-Img\ \varepsilon^{-1}$ volume and $-Img(\varepsilon+1)^{-1}$ surface electron loss, spectra of electro-optical differential functions $(\alpha,\ \beta)$, spectra of optical conduction of $\sigma$ massive and film samples correspondingly are shown in fig.1-5 and values of interband optical transitions defined by maximums of optical conduction $\sigma$ are shown in table1.

---


[1] *N.Z. Djalilov.* AMEA Fizika-riyaziyyat və texnika elmləri seriyası, fizika və astronomiya 2011, № 2

[2] *B.M. Golchman, V.A. Kudinov, I.A. Smirnov.* Poluprovodnikovie termoelektricheskie materialov na osnove $Bi_2Te_3$ (M:. Nauka,1972), s.216. (In Russian).

[3] *P.M. Lee, L. Pincherle.* Pros. Phys. Soc. 81, 461 (1963).

[4] *D.I.Greenaway and G. Harbeke.* I.Phys.Chem.Solids Pergamon Press, 26, 1585 (1965).

[5] *E.V. Oleshko, V.N. Korolishin.* FTT, 27, 2856 (1985). (In Russian).

[6] *V.L. Gurevich.* Kinetika fononnix system (M:. Наука,1980) 14. (In Russian).

[7] *E. Mooser, W.C. Pearson.* Phys. Chem. Solids **7**, 5 (1958).

[8] *B.M. Golchman, Z.M. Dashevskiy, V.I. Kaydanov, N.V. Kolomoech.* Plenochnie termoelementi: fizika I primenenie (M.: Наука, 1985) s.233. (In Russian).

[9] *S.A. Semiletov.* Trudi institute kristalloqrafii. 10, 74 (1954). (In Russian).

[10] *V.V. Sobolev, V.V. Nemoshkalenko.* Elektronnaya struktura poluprovodnikov (Kiev, nauk. Dumka, 1988). (In Russian).

[11] Opticheskie svoystva poluprovodnikov, pod red. Bira (IL, M, 1970). (In Russian).

[12] *N.Z. Djalilov.* Trudi X Mejd. konf. «Opto–nanoelektronika, nanotexnoloqii I mikrosistemi» (Ulyanovsk, 2008) 2008) 46-47. (In Russian).

[13] *N.Z. Djalilov, G.M. Damirov.* Trudi X Mejd. konf. «Opto–nanoelektronika, nanotexnoloqii I mikrosistemi» (Ulyanovsk, 2008) 45. (In Russian).

[14] *N.Z. Djalilov, G.M. Damirov.* FTT, 45, 500 (2011). (In Russian).

[15] *N.Z. Djalilov, G.M. Damirov.* Izv. NAN Azerb., seriya fiz.-mat. I texn., fiz. i astr., XXVIII, №5, 134 (2008); XXIX, 125 (2009). (In Russian).

[16] *N.Z. Djalilov, M.A. Maxmudova.* Izv. NAN Azerb., seriya fiz.-mat. I texn., fiz. i astr., XXX, 71 (2010). (In Russian).

[17] *N.Z. Djalilov, S.I. Mextieva, N.M. Abdullaev.* Izv. NAN Azerb., seriya fiz.-mat. i texn., fiz. i astr. XXVII, 114 (2007). (In Russian).

[18] *J.C. Phillips.* Phys. Rev. 125, 1931 (1962), 133, A452 (1964).
[19] *T. Moss, G. Barrel, B. Ellis.* Poluprovodnikovaya optoelektronika (M,. Мир, 1976) (In Russian).
[20] *N. Mott, E. Devis.* Elektronnie prochessi v nekristallicheskix prochessi v nekristallicheskix veshestvax. (M., Mir, 1982). (In Russian).
[21] Elektronnie yavleniya v xalkoqenidnix stekloobraznix poluprovodnikax. Pod red. K.D. Chendina. (SPb.: Nauka 486 (1996). (In Russian).
[22] *A. Rouz.* Osnovi teorii fotoprovodimosti. Izd. Mir, M. (1966). (In Russian).
[23] *Yu.N. Shunin, K.K. Shvarch.* JSX, 27, №6, 146-150 (1986). (In Russian).
[24] *K.K. Shvarch, Yu.N. Shunin, Ya.A. Teteris*. Izv. AN Lat SSR, ser. fiz. I tex. Nauk. №4, 51-57 (1987). (In Russian).
[25] *K.K. Shvarts, F.V. Pirgorov, Yu.N. Shunin, J.A. Teteris.* Cryst. Latt. Def. Amorph. Mat., **17**, 133-138 (1987).
[26] *Yu.N. Shunin, K.K. Shvarch.* FTP, 23, №6, 1049-1053 (1989). (In Russian).
[27] *A.I. Gubanov*. Kvantovo – elektonnaya teoriya amorfnix provodnikov. M., L.: Izd. AN SSSR, 1966, 250 s. (In Russian).
[28] *M. Kastner.* Phys. Rev. Lett., 1972, 26, N7, p.355.
[29] *R.E. Drews, R.L. Emerald, M.L. Slade, R. Zallen.* Solid State Comm., 1972, 10, N3, p.2.

*Received: 25.01.2018*

# MORPHOLOGY AND PHOTOLUMINESCENCE STUDY OF InGaN/GaN(In) HETEROJUNCTIONS

**G.K. GAHRAMANOVA, R.B. JABBAROV**
*Institute of Physics, Azerbaijan National Academy of Sciences, G. Javid av., 131, Baku 1143, Azerbaijan*
*Email: gulnaz qehremanova@hotmail.com,*

The characterization of the MOVPE (Metal Organic Vapour Phase Epitaxy) grown semi-polar {11-22}InGaN multiple quantum wells have been demonstrated and the excitation source power-dependent photoluminescence properties of InGaN/(In)GaN multiple quantum wells heterojunctions were investigated.

**Keywords:** III-nitrides, heterostructures, multiple quantum wells, semipolar, photoluminescence, InGaN, Atomic Force Microscopy
**PACS:** 78.20.±e, 81.05.Ea, 81.10.±h

## 1. INTRODUCTION

Over the last three decades group III-nitrides semiconductors have been studied extensively for their optoelectronic and electronic applications such as Light Emitting Diodes (LEDs), high temperature/power devices and chemical, gas and biological sensors [1-5]. The pioneering research on nitride semiconductors by Pankove, Amano, Akasaki, Nakamura and many others established the potential applications of these semiconductors in optoelectronics. It was only in the 1990's that high quality defects free GaN was successfully grown using Metalorganic Vapour Phase Epitaxy (MOVPE) and Metal Organic Chemical Vapor Deposition (MOCVD) [6-8]. With the recent developments in crystal growth technology and the ability to control the doping there has been an increased interest in GaN based heterostructures. Due to the combined effect of spontaneous and piezoelectric effects these heterostructures can form a high density and a high mobility electron gas channel. This high density electron gas makes these hetero structures ideal to be used as sensors. [9]

Most importantly, semipolar InGaN/GaN multiple quantum wells (MQWs) interesting compromise for achieving emission in the green–yellow region. Semipolar crystal directions are those, where the above mentioned internal fields are strongly reduced as a consequence of the crystalline symmetry, but not totally avoided. The semipolar {11-22} plane, being inclined by about 60° with respect to the polar c-plane. Thus, semipolar {11-22} plane has substantially reduced piezoelectric polarization compared to the c-plane [10]. Ultimately, nonpolar and semipolar nitrides may play a role in enabling both LEDs and laser diodes in the green–yellow region. Continued improvements in longer wavelength device efficiencies as well as sustained development of larger-area, high-quality, nonpolar substrates, will be critical for their commercial success. Unfortunately, the optical performance of these devices typically degrades with increasing In content in these layers, leading to the so-called "green gap" [1]. In addition, the quantum efficiency (EQE) in InGaN QWs LEDs decreases significantly in green oblast due to high dislocation density results from the lattice mismatch between the sapphire substrate and GaN leading to large non-radiative recombination rate, and charge separation from the polarization fields in the QW leading to reduction of the electron-hole wave function overlap and radiative recombination rate in particular for green-emitting QWs. We have proposed InGaN/InGaN MQW that focused mainly to improve the optical output power, and improved QE.

## 2. EXPERIMENT

### 2.1 Substrate preparation

In the prepare process of the semi-polar {11-22} structures, r-plane {10-12} sapphire substrate is used. The semi-polar {11-22} QWs orientation and related r-plane {10-12} (sapphire substrate have a tilting angle with respect to the c-plane {0001}, respectively $58,4^0$ and $57,6^0$.

In the photolithography process, a photoresist has been used and the substrate is rotated. By choosing a high speed of the rotation the thin photoresist was spread on the substrate and the substrate was covered by photoresist. In the next step the photoresist was exposed by UV light using pattered mask. After exposing, the unexposed parts of the photoresist are removed by chemical developer. The photoresist itself is patterned by optical lithography with a stripe shadow mask with an opening of 3 µm and a period of 6µm. In the next step the desired angle of trench side –wall was achieved via Reactive Ion Etching (RIE). After RIE, in order to remove the photoresist mask stripes on the substrate first oxygen plasma cleaning was done. Then in the chemical solutions of KOH and $H_2SO_4$ the sample was cleaned completely from residuals. Then the silicon dioxide ($SiO_2$) was sputtered on top of the sample (or c-plane facet) a mask to get covered with $SiO_2$ to avoid parasitic growth (Fig. 1). All non c-plane facets are covered with $SiO_2$. The GaN nucleates on the c-plane sidewall, forms triangular-shaped stripes and coalesces after a suitable growth time to a closed semipolar surface (Fig. 1).



131 H.Javid ave, AZ-1143, Baku
ANAS, G.M.Abdullayev Institute of Physics
E-mail: jophphysics@gmail.com

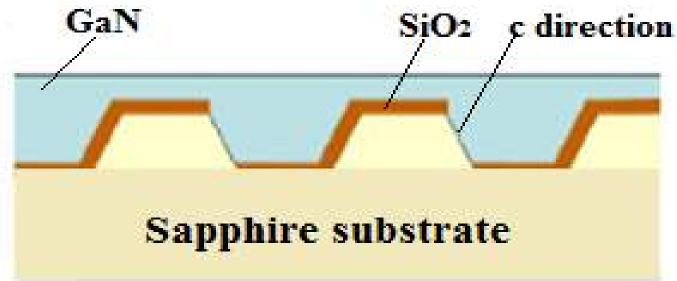


*Fig.1.* Demonstration of patterned sapphire substrate with 6 μm periodicity of trenches (3 μm opening and 3 μm grooves) and GaN template on it.

## 2.2 Structuring process and growth of {11-22}GaN and InGaN/GaN(In) quantum wells

The MOVPE growth was done in a commercial Aixtron-200/4 RF-S HT reactor using the standard precursors ammonia (NH3), trimethylgallium (TMGa), trimethylaluminum (TMAl), trimethylindium (TMIn) and triethylgallium (TEGa). The growth starts with about 20nm thick standard AlN nucleation layer at relatively low temperature of about 950°C. For the subsequent GaN growth, a reactor temperature of about 1020°C is chosen. The GaN gets pushed in c-direction and builds triangularly formed stripes, which coalesce after a suitable growth time to a semipolar {11-22}-oriented surface. An in-situ deposited SiN interlayer helps to improve the crystal quality by stopping defects penetrating to the sample surface. By decreasing the growth temperature of the topmost GaN layer to 970°C, the growth gets pushed further in c-direction and the coalescence of the stripes gets improved (Fig. 1).

After growing GaN template the two main MQWs samples have been grown and demonstrated in this paper. One of them InGaN/GaN (barrier layer without indium contents) MQWs heterojunctions second one is InGaN/InGaN (barrier layer with indium contents) MQWs heterojunctions.

On top of the {11-22} oriented GaN template, the growth conditions were same for these two samples, so that the 5 pair InGaN quantum wells with a thickness of 2.3 nm and the GaN or InGaN barriers with a thickness of about 8 nm were grown periodicity at a temperature of about 720°C and 755°C respectively.

## 3. RESULTS AND DISCUSSIONS

This study investigates the morphology of semipolar InGaN MQWs using Optical microscope and Atomic Force Microscopy (AFM). Figure 2a shows a typical optical microscope image of 5 pairs semipolar InGaN/GaN MQW heterostructures which modified by 100x, respectively figure 2b illustrates the surface of 5 pairs semipolar InGaN/GaNIn MQW heterostructures surface. From the images the morphology 3 µm opening and 3 µm grooves stripe on the surface easily visible on the two samples. AFM was performed to assess the morphology of the 50x50 µm$^2$ surface. The 2D AFM amplitude forward images have been demonstrated in Figure 3a and 3b for the InGaN/GaN and InGaN/GaNIn samples respectively. AFM measurements show a surface roughness of 22 nm, Root mean square (RMS) 26 nm for QWs with GaN barrier and the surface roughness of 24 nm, RMS 28 nm with GaInN barrier in an area of 50µm × 50µm$^2$ ( Fig 3c and 3d respectively). From the figure 3e and 3f the differences of AFM dimensions between the samples is clearly compared.

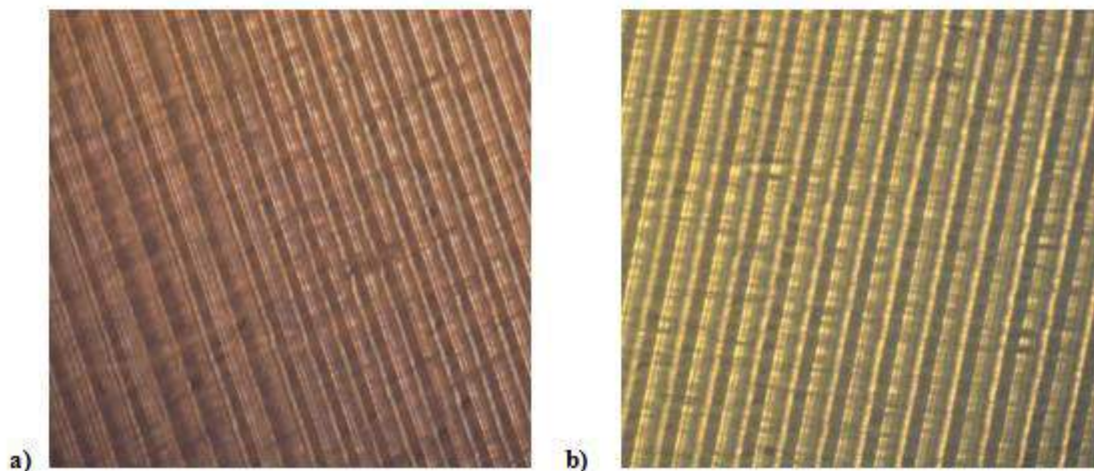


*Fig. 2.* Optical microscope images of {11-22} InGaN/GaN (a) and InGaN/GaNIn (b) MQW heterostructures .

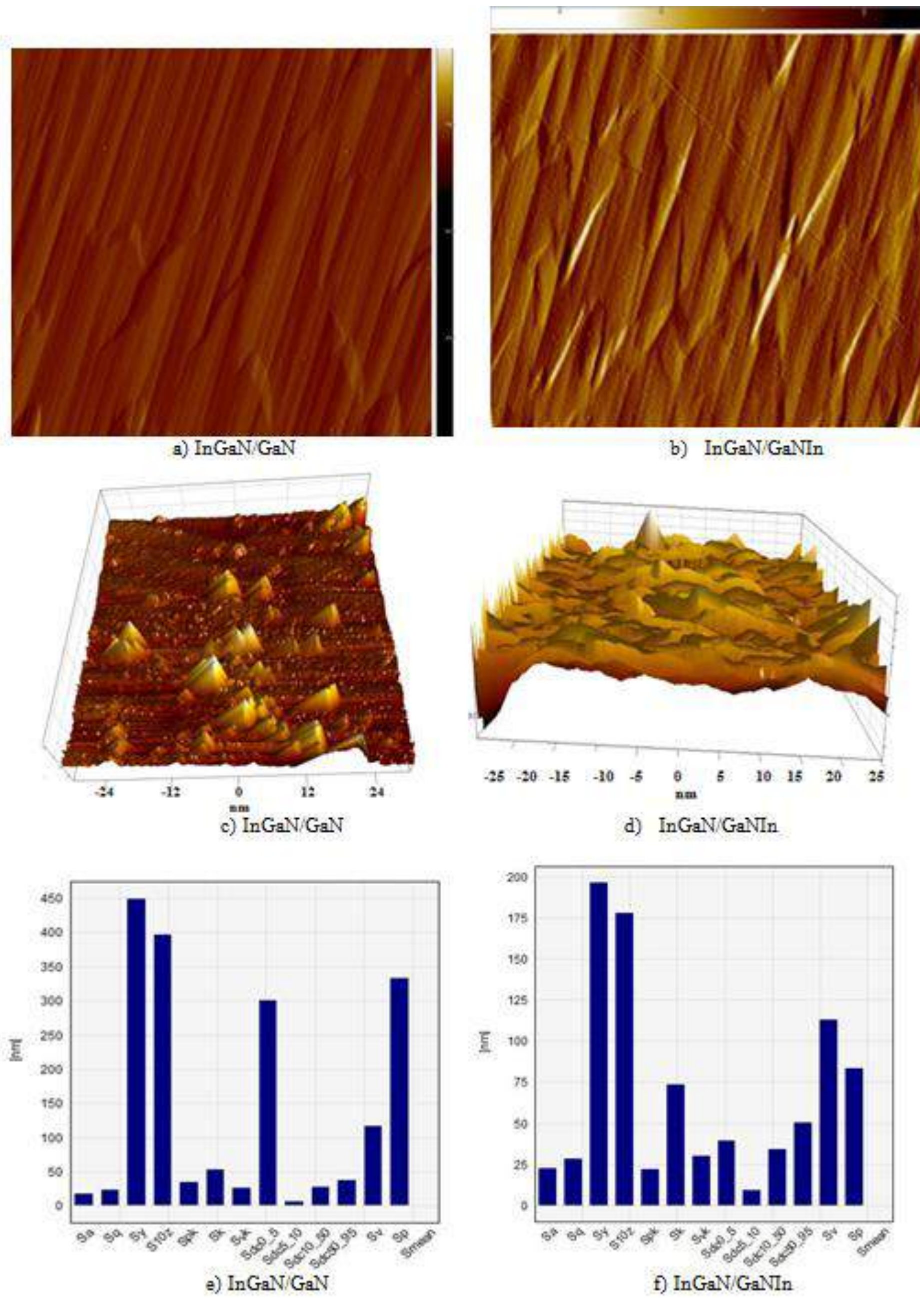


*Fig.3.* Morphology and roughness of semipolar InGaN/GaN(In) MQW heterostructures on 50 x50μm$^2$ surface area. a), b) AFM 2D amplitude forward , c), d) AFM 3D images, e), f ) AFM characterizations parameters (Sa- Roughness Average, Sq- Root mean square, Sy-peak-peak, S10z-ten point height, Spk-reduced peak high, Sk-core roughness depth, Svk-reduce valley depth, Sdc0_5, Sdc5_10, Sdc10_50, Sdc50_95-5%, 5-10%, 10-50%, 50-95% height, Sv- max valley depth, Sp-max peak height, Smean-mean height).

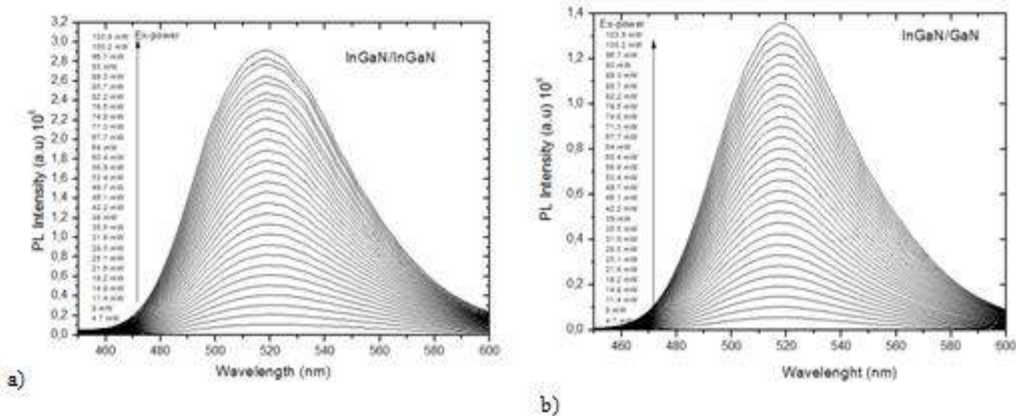


*Fig. 4.* At room temperature excitation power dependence photoluminescence. a) InGaN/GaN and b) InGaN/InGaN QWs heterostructures.

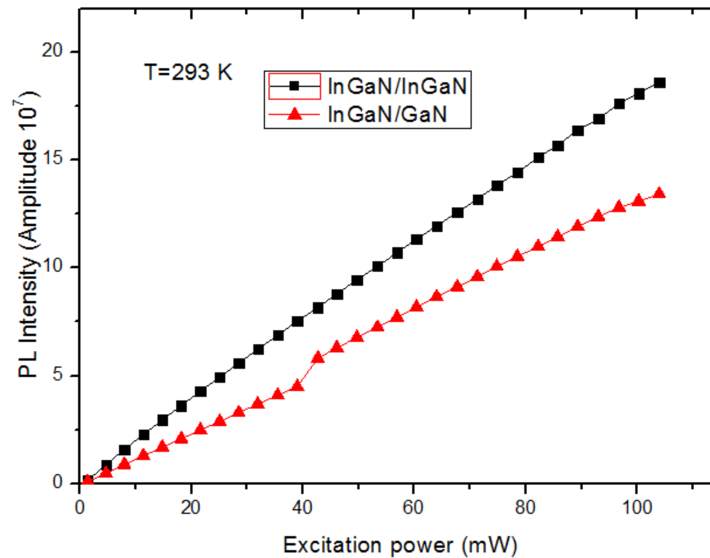


*Fig. 5.* The excitation source power dependence of integrated PL intensity at room temperature of (11-22) InGaN/GaN (red) and InGaN/InGaN (black) QWs heterostructures.

At room temperature excitation source power dependence photoluminescence (PL) properties of InGaN/GaN and InGaN/GaNIn MQW heterojunctions show peak position is not shifted with increasing excitation source power (Fig. 4 a,b), but PL intensity increased linearly with increasing excitation source power (Fig.5), indicating that "Quantum-confined Stark effect" (QCSE) in MQWs grown on semipolar direction is significantly reduced. The origin of the intense emission should be due to the strong confinement of the electron-hole pairs into the MQW structure. The strong confinement should increase e-h wave function overlap and radiative recombination rates. This InGaN barrier-related improvement in QE and efficiency droop could be useful for the realization of longer wavelength "green-gap" range LEDs where poor QE and efficiency droop are more prominent due to high indium (In) in the active region. Results shows that, the emission intensity of MQW structure is increased due to effect of InGaN barrier layer and it could be useful to realize LEDs with the "green-gap" regime wavelength emission with high QE and low droop.

## 4. CONCLUSION

We have demonstrated improvement of surface morphology in semipolar InGaN/(In)GaN MQWs heterostructures which grown by MOVPE. The roughness of the QWs where was 22 and 24 nm with GaN and InGaN barriers respectively. At room temperature PL intensity increased linearly with increasing excitation source power for two samples. We obtained improvement PL intensity of InGaN/InGaN MQWs compare to InGaN/GaN and this indicating that QCSE in MQWs growth on semipolar direction is significantly reduced and the results is useful to realize LEDs with the "green-gap" regime wavelength emission with high QE and low droop.

[1] *J. Piprek*. Phys. Status Solidi A 207, 2217–2225 (2010).
[2] *Y. Yang, L. Zhang, T. Wei, and Y. Zen.*J. Display Technol. 11, 456–460 (2015).
[3] *Y.K. Kuo, J.Y. Chang, M.C. Tsai, and S.H. Yen.* Appl. Phys. Lett. 95, 011116 (2009).
[4] *H. Morkoc, H. Strite, S. Gao, G.B. Lin, M.E. Sverdlov, B. Burns.* A review of large band gap Sic. III-V nitrides, and ZnSe based II-VI semiconductor structures and devices Appl. Phys. Rev. 76, 1363 1994.
[5] *S. Nakamura*. MRS Bull. 34, 101–107 (2009).
[6] *H. Morkoc.* Nitride semiconductors and devices. New York, Springer, 1999.
[7] *H. Amano, N. Sawaki, I. Akasaki and Y. Toyoda.* "Metalorganic vapor phase epitaxial growth of a high quality GaN film using an AlN buffer layer"Appl. Phys. Lett. 48, 353 1986.
[8] *S. Nakamura.* "GaN Growth Using GaN bufferlayer" Jap. J. Appl. Phys. 30, 1991.
[9] *Joachim Piprek.* "Nitride Semiconductor devices book" Germany, Wiley-VCH, 2007.
[10] *H. Sato, A. Tyagi, H. Zhong, N. Fellows, R. B. Chung, M. Saito, K. Fujito, J. S. Speck, S.P. DenBaars and S. Nakamura.* "High power and high efficiency green light emitting diode on free-standing semipolar (1 1 Ī22) bulk GaN substrate," Phys. Status Solidi (RRL), vol. 1, no. 4, pp. 162–164, 2007.

*Received: 22.02.1018*

**ISSN 1028-8546**

**2018, Vol. XXIV, № 1**
**Section: En**

# *CONTENTS*

| | | |
|---|---|---|
| 1. | Photoluminescence of $(Ga_2S_3)_{0.94}$:$(Eu_2O_3)_{0,05}(Tb_2O_3)_{0,01}$ crystal<br>**O.B. Tagiyev, Kh.B. Ganbarova, F.A. Kazimova, T.Sh. Ibragimova, K.O. Tagiyev, S.O. Guseynova** | 3 |
| 2. | The production of the Higgs boson on electron-positron linear colliders<br>**F.T. Khalil-zada** | 8 |
| 3. | Plasma methods for nanostructuring the polymer matrix of piezoelectric nanocomposites<br>**F.N. Tatardar, M. A. Kurbanov, N. A. Safarov, Sh. Sh. Amirov, O. A. Aliyev** | 18 |
| 4. | The silver selenide single crystal growth and devices on its base<br>**G.S. Hadjieva, F.A. Kazimova, T.SH. Ibrahimova, K.O. Tagiev, E.G. Asadov** | 24 |
| 5. | Dielectric properties of polymer composites based on high-density polyethylene and gallium arsenide<br>**N.N. Gadzhieva, A.M. Magerramov, G.B. Akhmedova** | 27 |
| 6. | The production of the Higgs boson and $t\bar{t}$ -pair in polarized $e^-e^+$ -beams<br>**S.K. Abdullaev, M.Sh. Gojayev, N.A. Nasibova, G.A. Soltanova** | 32 |
| 7. | The formation of nano-defect structures in process of double cross slip<br>**A.Sh. Kakhramanov, N.M. Abdullayev, K.Sh. Kakhramanov** | 40 |
| 8. | Temperature dependence of photoluminescence of $ZnGa_2S_4$<br>**T.G. Kerimova, I.A. Mamedova, I.G. Nasibov, S.G. Asadullaeva, Z. Kadiroglu** | 45 |
| 9. | The production of Higgs boson on polarized colliding linear $e^+e^-$ colliders and supersymmetry<br>**F.T. Khalil-zade** | 48 |
| 10. | Spectra of optical parameters of $Bi_2Te_3$ film in 1÷6 eV interval<br>**N.Z. Jalilov** | 53 |
| 11. | Morphology and photoluminescence study of InGaN/GaN(In) heterojunctions<br>**G.K. Gahramanova, R.B. Jabbarov** | 59 |

www.physics.gov.az